

Transformations and Functions of  
Neural Representations in a  
Subcortical Social Behavior Network

Thesis by  
Bin Yang

In Partial Fulfillment of the Requirements for  
the degree of  
Doctor of Philosophy

The logo for the California Institute of Technology (Caltech), featuring the word "Caltech" in a bold, orange, sans-serif font.

CALIFORNIA INSTITUTE OF TECHNOLOGY  
Pasadena, California

2022  
(Defended May 17, 2022)

© 2022

Bin Yang

ORCID: 0000-0002-3878-1530

I dedicate this thesis to my grandmother for always being there for me.

## ACKNOWLEDGEMENTS

I'd like to thank David Anderson for his support and mentorship.

I'd like to thank my thesis committee members Markus Meister, Viviana Gradinaru and Yuki Oka.

I'd like to thank members of the Anderson Lab.

## ABSTRACT

The brain functions by processing sensory information such as vision, smell, and touch, integrating it with internal states (hunger, fear, aggression) and memory to produce relevant motor outputs (eating, fleeing, or fighting). To understand the brain, neuroscientists study neural representations (patterns of neural activity that correlate with features of the outside world) to and perform perturbations (activate or silence groups of neurons) to determine its function. Past studies on neural representations gave us insights into how sensory regions filter complex inputs to retain relevant information and how coordinated activity in the motor regions produce complex motor actions. However, little is known about how information is processed in the inner brain (between sensory and motor) and how behaviors are controlled. Mating and aggression are innate social behaviors that are essential for animals' survival. During social interactions, such as those preceding mating or fighting, the brain must determine the sex of a conspecific to produce sex-appropriate behaviors that are conducive to its survival. Functional studies demonstrated that they are controlled by deep subcortical circuits in the extended amygdala and hypothalamus. My thesis attempts to understand how the inner brain works by 1) showing that chemosensory cues encoding conspecific's sex are transformed to neural representations of mating and aggression during social interactions by recording from a genetically defined group of neurons in different regions of the extended amygdala and hypothalamus. 2) Demonstrating that the neural activity representing conspecific's sex is necessary for the emergence of behavioral representations in the hypothalamus.

## PUBLISHED CONTENT AND CONTRIBUTIONS

**Yang, B.**, Karigo, T., and Anderson, D.J. (2022). “Transformations and Functions of Neural Representations in a Subcortical Social Behaviour Network”. *Nature* (accepted)

B.Y. co-conceptualized the project, performed experiments, analyzed and prepared the data, and co-wrote the manuscript.

Nair, A., Karigo, T., **Yang, B.**, Linderman, S.W., Anderson, D.J., and Kennedy, A. (2022). “An approximate line attractor in the hypothalamus that encodes an aggressive internal state”. bioRxiv preprint. doi: 10.1101/2022.04.19.488776

B.Y. performed neural recording experiments, prepared the data for analysis.

Karigo, T., Kennedy, A., **Yang, B.**, Liu, M., Tai, D., Wahle I.A., and Anderson., D.J. (2021). “Distinct hypothalamic control of same- and opposite-sex mounting behaviour in mice”. *Nature* 589, 258–263. doi:10.1038/s41586-020-2995-0

B.Y. performed neural recording experiments, prepared the data for analysis.

**Yang, B.**, Treweek, J.B., Kulkarni, R.P., Deverman, B.E., Chen, C., Lubeck, E., Shah, S., Cai, L., Gradinaru, V. (2014). “Single-cell phenotyping within transparent intact tissue through whole-body clearing”. *Cell* 158 (4), 945-958. doi: 10.1016/j.cell.2014.07.017

B.Y. co-conceptualized the project, performed experiments, analyzed and prepared the data, and co-wrote the manuscript.

## TABLE OF CONTENTS

Acknowledgements.....	iv
Abstract .....	v
Published Content and Contributions.....	vi
Table of Contents.....	vii
Chapter I: Introduction .....	1
Chapter II: Preamble.....	15
Chapter II: Transformations and Functions of Neural Representations in a Subcortical Social Behavior Network.....	22
Appendix I: Single-cell phenotyping within transparent intact tissue through whole-body clearing.....	69

*Chapter 1*

## INTRODUCTION

A main goal in modern neuroscience is to understand the neural basis for behavior - how sensory information is processed and integrated with internal states and memory to give rise to the decision and execution of behavior. To tackle this question, neuroscientists generally take two different approaches – 1) Studying how information is represented by neural activity and how this representation is transformed among various brain circuits (observations). 2) Artificially activating / silencing the activity of small groups of neurons and study its effects on behavior (perturbations). Observational studies are inherently ethologically relevant but cannot establish causality, while perturbational studies establish causality but may not be ethological relevant. In this chapter, I provide an overview of the neural circuit underlying mating and fighting. In the preamble of Chapter II, I discuss the features of neural representations in several key neural substrates during social interactions. Chapter II of my thesis makes an attempt to combine both observational and perturbational approaches to understand the neural basis for mating and fighting in male mice. This “perturbational observation” approach revealed unexpected functions from a group of inhibitory neurons in transforming the representations of conspecifics’ identity to representations of mating and fighting behaviors in the extended amygdala and the hypothalamus. Finally, in Appendix I, I include the results from an early attempt to improve existing brain clearing methods for visualizing the connectivity and cell types in an entire mouse brain prior to the start of my studies on the social behavior circuit.

From flies, mice to humans, mating and fighting are evolutionarily conserved innate social behaviors necessary for survival. Animals fight to acquire food and territory, and mate with partners to produce offspring. In order to mate or fight, animals must first identify the sex of the conspecifics<sup>1</sup>. Mice rely heavily on olfactory cues to determine the status of conspecifics<sup>2,3</sup>. Two sets of olfactory circuits detect and process either volatile (main olfactory system via the main olfactory epithelium or MOE) or non-volatile (accessory olfactory system via the vomeronasal organ or VNO) chemosensory cues originating from urine / anogenital secretions or tear<sup>3-7</sup>. Electrical recordings of single neurons in the main olfactory bulb (MOB, receives inputs from the MOE) revealed that MOB neurons selectively respond to specific chemical compounds that are present in male or female urine<sup>8</sup>. Single-unit recordings in the accessory olfactory bulb (AOB, receives inputs from the VNO) during social behaviors show that AOB neurons are tuned to the combinations of sex and genetic makeup<sup>9</sup>. Perturbational experiments show that both the main and accessory olfactory systems are necessary for the display of sex-typical mating and aggression<sup>10,11</sup> – Male mice either failed to mate or fight when the main olfactory signaling is disrupted<sup>6,12</sup>, or they mated both male and female mice when the accessory olfactory signaling is disrupted<sup>4</sup>. Both main and accessory olfactory projections converge onto different regions of the extended amygdala that include the medial amygdala (MeA) and the posterior amygdala (PA)<sup>13</sup> (**Figure 1**).

The MeA is one of the many subdivisions of the extended amygdala that have been shown to play a major role in mediating social behaviors including mating and fighting<sup>14,15</sup>. The MeA is divided along the anterior-posterior and dorsal-ventral axes and different

subdivisions are genetically heterogeneous and functionally distinct<sup>14,16,17</sup>. It receives inputs directly from the AOB and indirectly from the MOB via the CoA<sup>13</sup>. Early c-Fos studies indicate that the MeA neurons respond to chemosensory cues and are active during mating and fighting<sup>14,16,18</sup>. A study analyzed AOB and MeA recordings from anesthetized mice provided some evidence of slightly increased selectivity of MeA neurons to male or female urine compared to responses from AOB neurons<sup>19</sup>. Microendoscopic imaging of the MeA CaMKII<sup>+</sup> (a mixture of glutamatergic and GABAergic neurons) population revealed that neurons in MeA selectively respond to either male or female conspecifics during social interactions<sup>20</sup>. Functionally, lesioning the MeA impaired mating behaviors in rats and hamsters while its effects on fighting was mixed or unclear<sup>15,21-24</sup>. Recent perturbational studies demonstrated that optogenetic activation of the GABAergic populations in the postero-dorsal part of the MeA (MeApd) triggered fighting in male mice while activating the glutamatergic population in MeApd promoted self-grooming and suppressed ongoing fighting<sup>25,26</sup>. Chemogenetic silencing of aromatase<sup>+</sup> neurons in MeApd suppressed fighting, but not mating in mice<sup>27</sup>. Results from lesioning studies and recent cell-type specific perturbations suggest the possibility that mating and fighting are mediated by distinct cell types in MeA. It also raises the question to how inhibitory neurons in the MeApd play a positive role to promote fighting in mice.

The function of the posterior amygdala (PA) was relatively unknown until it was recently shown to play a major role in mediating mating and fighting in mice<sup>28-30</sup>. PA was initially identified as a potential source of excitatory input into the ventromedial hypothalamus (VMH) - the key node in mediating fighting in mice<sup>28,31</sup>. Retrograde tracing and functional

mapping experiments show that PA neurons that project to the VMH and the medial preoptic area (MPOA, key node in mediating mating behaviors) are mostly excitatory, express estrogen receptor type-1 (Esr1), and are spatially and transcriptionally distinct<sup>28-30</sup>. Fiber-photometry recording of neurons that project to MPOA and neurons that project to VMHvl show that PA – MPOA neurons become activated during male – female interactions while PA – VMHvl neurons become activated during male – male interactions<sup>28</sup>. However, it remains unclear how information is represented in PA due to the lack of single-unit recordings. It is possible that the neural representations are comparable to that of the MeA as the PA is similarly located in the mating and fighting circuit – two synapses away from the olfactory chemoreceptors and may provide the complementary excitatory input to downstream targets. Functional perturbations show that PA neurons play positive roles in promoting mating and fighting – Activation of PA Esr1<sup>+</sup> neurons that project to VMHvl projections evoke fighting while activation of the PA Esr1<sup>+</sup> neurons that project to MPOA enhance mating<sup>28,30</sup>. Further characterizations of the PA – VMHvl synapses show that long-term potentiation of the excitatory synapse mediate increased aggressiveness after repeated experiences of winning<sup>29</sup>. The GABAergic MeA and the glutamatergic PA further converge onto the principal region of the bed nucleus of stria terminalis (BNSTpr), the medial preoptic area (MPOA), and the ventrolateral part of the ventromedial hypothalamus (VMHvl)<sup>25,28,32</sup> (**Figure 1**).

The BNST is a part of the extended amygdala that sits distally to the major output fibers (stria terminalis) originating from the amygdala proper<sup>14</sup>. It is consisted of multiple subdivisions of highly heterogeneous neuronal populations along both the anterior-posterior and dorsal

ventral axes<sup>33-36</sup>. Situated in between sensory and motor regions, the predominantly GABAergic BNST is thought to function as an inhibitory relay. It forms strong reciprocal connections with the amygdala and projects to diverse brain regions that mediate a variety of functions including but not limited to arousal, stress, anxiety, feeding and reproductive behaviors<sup>14,37</sup>. The anterior portion of the BNST was extensively studied for its role in corticotropin releasing factor (CRF) signaling related stress and anxiety<sup>38</sup>, while the posterior subdivisions of BNST (more specifically, the principal subdivision of the posterior BNST or BNSTpr) was known for its sexual dimorphism (BNSTpr is larger in males of many species), high expression of gonadal hormonal receptors (estrogen and androgen receptors), and its role in reproductive behaviors such as mating and fighting<sup>26</sup>. c-Fos studies show that urine of conspecifics and social interactions including mating and fighting behaviors activate neurons in the BNSTpr<sup>16,39-43</sup>. Lesioning the BNSTpr produces deficits in both mating and fighting in mice<sup>44,45</sup>. A recent study demonstrated functionally the involvement of MeA and BNSTpr connectivity in the enhancement of aggressiveness in mice<sup>46</sup>. Optogenetic activation of the MeA neuropeptide Y (NPY)-expressing neuron axonal terminal in BNSTpr increased the fighting duration in mice<sup>46</sup>. In a separate study, the Shah group performed fiber photometric recordings of the bulk activity responses from the aromatase positive subset of BNSTpr neurons in sexually naïve male mice (AB neurons, specifically expressed in the BNSTpr and not the surrounding subdivisions of BNST) and showed that AB neurons respond to early interactions with male and female conspecifics, during mating, but not after fighting has started<sup>41</sup>. In addition, the response to investigating females was significantly stronger than the response to investigating males, suggesting conspecifics identity could be represented by an intensity code. Functionally, genetically ablating or chemogenetically

silencing the AB neurons disrupted urine preference (an odor discrimination assay that reflect the ability for an animal to differentiate two odors, in this case, between male and female urine), mating and fighting<sup>41</sup>. Optogenetic activation of the AB neurons in sexually naïve males promoted mating to both male and female conspecifics<sup>41</sup>. These results suggests that AB neurons (further confined to a subset of  $Esr1^+/Tac1^+$  BNSTpr neurons in a later study by the same group<sup>47</sup>) distinguish conspecifics' sex by the overall levels of neural activity and function to promote mating in male mice.

BNSTpr project directly to the hypothalamic structures MPOA and VMHvl – key neural substrates that mediate mating and fighting<sup>37,48-50</sup>. The sexually dimorphic MPOA has long been implicated in parental and sexual behaviors in mammals<sup>51,52</sup>. Fiber photometry recordings of the  $Esr1^+$  MPOA neurons during social interactions show that the MPOA is active during male and female-directed sniffing and ultrasonic vocalization positive (USV<sup>+</sup>) mating but becomes suppressed during male-directed fighting<sup>50,53</sup>. Microendoscopic imaging of the  $Esr1^+$  MPOA neurons show distinct subpopulations that are tuned to specific behaviors during social interactions with male or female conspecifics - including sniffing male or female, female-directed mounting, intromission, even male-direct attack<sup>50</sup>. Further analysis showed that mating behaviors are represented in the MPOA using rotational dynamics (patterns of neural activity that follow a rotational trajectory in the state space)<sup>54</sup>. Functional perturbations show that optogenetic activation of the MPOA Galanin<sup>+</sup> (Gal<sup>+</sup>) neurons in male mice suppressed attacks and promoted pup grooming behavior.<sup>55</sup> Activating the MPOA  $Esr1^+$  or the MPOA VGAT<sup>+</sup>/ $Esr1^+$  populations suppressed ongoing fighting and evoked

ultrasonic vocalizations positive (USV<sup>+</sup>) mounting behavior towards both female and male conspecifics and towards inanimate objects<sup>50,53</sup>.

Following the initial discovery that electrical stimulation of the hypothalamus triggered aggression in cats<sup>2,56,57</sup>, a series of studies identified and refined a broad region referred to as the hypothalamic attack area (HAA) in the hypothalamus of many species in which electrical stimulations could trigger aggression<sup>58,59</sup>. The precise neural substrates that control fighting remained unclear until the advent of optogenetics that enabled precise spatial and temporal control of neural activity. Using optogenetics, the Anderson group identified neurons in the VMHvl that when activated, could evoke attacks indiscriminately towards male or female conspecifics or even towards inanimate objects in male mice<sup>48</sup>.

Follow-up studies identified the genetic identity of the VMHvl attack promoting neurons to be *Esr1* expressing and progesterone receptor-expressing (*Pgr*, separate but overlapping with *Esr1*)<sup>39,49</sup>. Chemogenetic and optogenetic silencing of the VMHvl *Esr1*<sup>+</sup> cells suppressed attacks<sup>39,49</sup>. Microendoscopic imaging of the *Esr1*<sup>+</sup> population in VMHvl show that, unlike the MPOA, very few neurons in VMHvl are tuned to specific behaviors.

Separate populations of neurons in VMHvl mostly represent the sex identity of conspecifics and are active at varying intensities during different phases of social interactions, including mating and fighting<sup>50,54,60</sup>. It was unclear how the VMHvl could encode aggression when most cells are tuned to intruder identity. Further analysis revealed that the representation of mating and fighting in VMHvl resembles that of a line attractor (a network mechanism that enables the encoding of continuously varying features, and in this

case, aggression) where mating and fighting are encoded as persistence and intensity of neural activity in the same female or male tuned populations<sup>54</sup>.

The GABAergic MPOA and glutamatergic VMHvl then project to the periaqueductal gray (PAG), a pre-motor region necessary for the execution of mating and fighting<sup>61,62</sup>. Thus, during social interactions, chemosensory information that flow through the neural circuits that mediate mating and fighting are subjected to the following transformations – chemosensory to conspecific identity to behavior decision to behavior execution (**Fig. 1**).

Based on our current understanding that MPOA encode mating behavior, VMHvl encode fighting behavior, and BNSTpr mostly encode conspecific's identity and it's situated one synapse away from MPOA and VMHvl, studying the interactions between BNSTpr, MPOA and VMHvl for the control of mating and fighting become an interesting entry point into elucidating the fundamental question of how sensory inputs are transformed into representations of behavior.

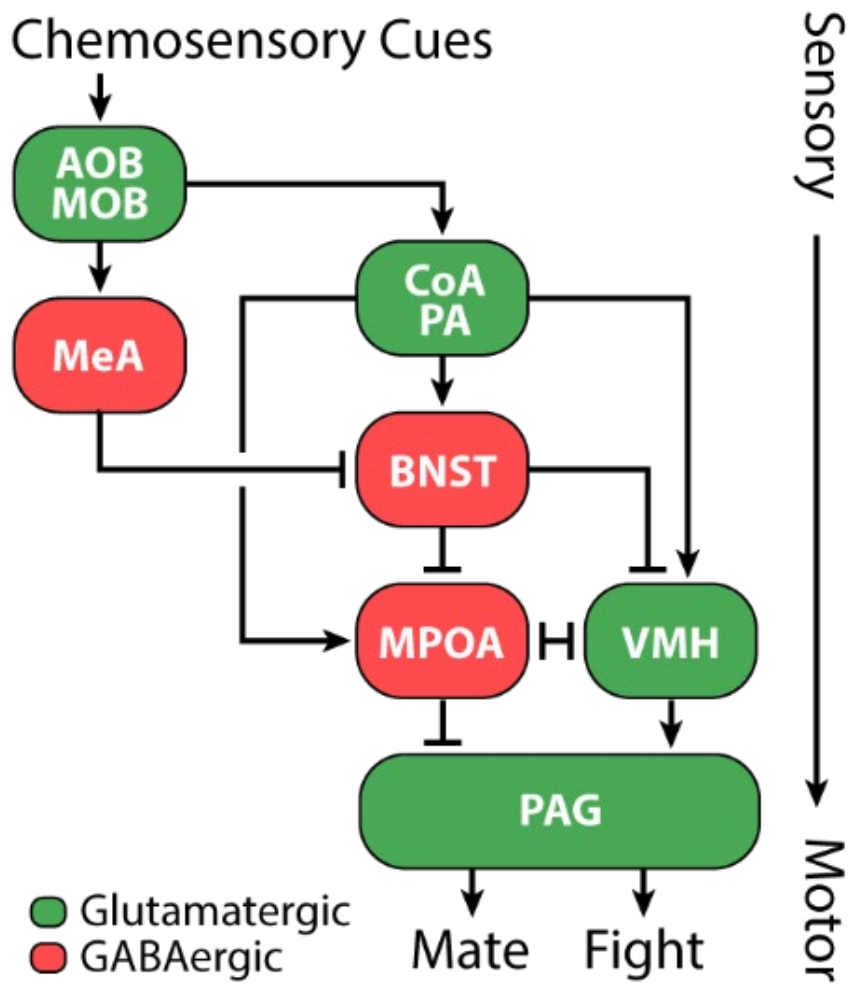


Figure 1. Neural Circuit underlying Mating and Fighting.

## References

1. Lorenz, K. *On aggression*. (Taylor & Francis e-Library, 2005).
2. Anderson, D. J. Circuit modules linking internal states and social behaviour in flies and mice. *Nat. Rev. Neurosci.* **17**, 692–704 (2016).
3. Molecular detection of pheromone signals in mammals: from genes to behaviour | Nature Reviews Neuroscience. <https://www.nature.com/articles/nrn1140>.
4. Stowers, L., Holy, T. E., Meister, M., Dulac, C. & Koentges, G. Loss of Sex Discrimination and Male-Male Aggression in Mice Deficient for TRP2. *Science* **295**, 1493–1500 (2002).
5. Chamero, P. *et al.* Identification of protein pheromones that promote aggressive behaviour. *Nature* **450**, 899–902 (2007).
6. Deficits in sexual and aggressive behaviors in *Cnga2* mutant mice | Nature Neuroscience. <https://www.nature.com/articles/nn1589>.
7. Hattori, T. *et al.* Self-Exposure to the Male Pheromone ESP1 Enhances Male Aggressiveness in Mice. *Curr. Biol.* **26**, 1229–1234 (2016).
8. Lin, D. Y., Zhang, S.-Z., Block, E. & Katz, L. C. Encoding social signals in the mouse main olfactory bulb. *Nature* **434**, 470–477 (2005).
9. Luo, M. Encoding Pheromonal Signals in the Accessory Olfactory Bulb of Behaving Mice. *Science* **299**, 1196–1201 (2003).
10. Kimchi, T., Xu, J. & Dulac, C. A functional circuit underlying male sexual behaviour in the female mouse brain. *Nature* **448**, 1009–1014 (2007).
11. Leypold, B. G. *et al.* Altered sexual and social behaviors in *trp2* mutant mice. *Proc. Natl. Acad. Sci.* **99**, 6376–6381 (2002).
12. Wang, Z. *et al.* Pheromone Detection in Male Mice Depends on Signaling through the Type 3 Adenylyl Cyclase in the Main Olfactory Epithelium. *J. Neurosci.* **26**, 7375–7379 (2006).
13. Keshavarzi, S., Power, J. M., Albers, E. H. H., Sullivan, R. K. S. & Sah, P. Dendritic Organization of Olfactory Inputs to Medial Amygdala Neurons. *J. Neurosci.* **35**, 13020–13028 (2015).

14. Newman, S. W. The Medial Extended Amygdala in Male Reproductive Behavior A Node in the Mammalian Social Behavior Network. *Ann. N. Y. Acad. Sci.* **877**, 242–257 (1999).
15. Lehman, M. N., Winans, S. S. & Powers, J. B. Medial Nucleus of the Amygdala Mediates Chemosensory Control of Male Hamster Sexual Behavior. *Science* **210**, 557–560 (1980).
16. Choi, G. B. *et al.* Lhx6 Delineates a Pathway Mediating Innate Reproductive Behaviors from the Amygdala to the Hypothalamus. *Neuron* **46**, 647–660 (2005).
17. Bian, X., Yanagawa, Y., Chen, W. R. & Luo, M. Cortical-Like Functional Organization of the Pheromone-Processing Circuits in the Medial Amygdala. *J. Neurophysiol.* **99**, 77–86 (2008).
18. Dulac, C. & Torello, A. T. Molecular detection of pheromone signals in mammals: from genes to behaviour. *Nat. Rev. Neurosci.* **4**, 551–562 (2003).
19. Bergan, J. F., Ben-Shaul, Y. & Dulac, C. Sex-specific processing of social cues in the medial amygdala. *eLife* **3**, e02743 (2014).
20. Li, Y. *et al.* Neuronal Representation of Social Information in the Medial Amygdala of Awake Behaving Mice. *Cell* **171**, 1176–1190.e17 (2017).
21. Kondo, Y. Lesions of the medial amygdala produce severe impairment of copulatory behavior in sexually inexperienced male rats. *Physiol. Behav.* **51**, 939–943 (1992).
22. Kondo, Y. & Arai, Y. Functional association between the medial amygdala and the medial preoptic area in regulation of mating behavior in the male rat. *Physiol. Behav.* **57**, 69–73 (1995).
23. Busch, D. E. & Barfield, R. J. A failure of amygdaloid lesions to alter agonistic behavior in the laboratory rat. *Physiol. Behav.* **12**, 887–892 (1974).
24. Vochtelloo, J. D. & Koolhaas, J. M. Medial amygdala lesions in male rats reduce aggressive behavior: interference with experience. *Physiol. Behav.* **41**, 99–102 (1987).
25. Hong, W., Kim, D.-W. & Anderson, D. J. Antagonistic Control of Social versus Repetitive Self-Grooming Behaviors by Separable Amygdala Neuronal Subsets. *Cell* **158**, 1348–1361 (2014).
26. Chen, P. & Hong, W. Neural Circuit Mechanisms of Social Behavior. *Neuron* **98**, 16–30 (2018).

27. Unger, E. K. *et al.* Medial Amygdalar Aromatase Neurons Regulate Aggression in Both Sexes. *Cell Rep.* **10**, 453–462 (2015).
28. Yamaguchi, T. *et al.* Posterior amygdala regulates sexual and aggressive behaviors in male mice. *Nat. Neurosci.* **23**, 1111–1124 (2020).
29. Stagkourakis, S., Spigolon, G., Liu, G. & Anderson, D. J. Experience-dependent plasticity in an innate social behavior is mediated by hypothalamic LTP. *Proc. Natl. Acad. Sci.* **117**, 25789–25799 (2020).
30. Zha, X. *et al.* VMHvl-Projecting Vglut1+ Neurons in the Posterior Amygdala Gate Territorial Aggression. *Cell Rep.* **31**, 107517 (2020).
31. Lo, L. *et al.* Connectional architecture of a mouse hypothalamic circuit node controlling social behavior. *Proc. Natl. Acad. Sci.* **116**, 7503–7512 (2019).
32. Canteras, N. S., Simerly, R. B. & Swanson, L. W. Organization of projections from the ventromedial nucleus of the hypothalamus: A Phaseolus vulgaris-Leucoagglutinin study in the rat. *J. Comp. Neurol.* **348**, 41–79 (1994).
33. Gungor, N. Z. & Pare, D. Functional Heterogeneity in the Bed Nucleus of the Stria Terminalis. *J. Neurosci.* **36**, 8038–8049 (2016).
34. Dong, H.-W. & Swanson, L. W. Projections from bed nuclei of the stria terminalis, anteromedial area: Cerebral hemisphere integration of neuroendocrine, autonomic, and behavioral aspects of energy balance. *J. Comp. Neurol.* **494**, 142–178 (2006).
35. Wood, R. I. & Swann, J. M. The bed nucleus of the stria terminalis in the Syrian hamster: Subnuclei and connections of the posterior division. *Neuroscience* **135**, 155–179 (2005).
36. Rodríguez-Sierra, O. E., Turesson, H. K. & Pare, D. Contrasting distribution of physiological cell types in different regions of the bed nucleus of the stria terminalis. *J. Neurophysiol.* **110**, 2037–2049 (2013).
37. Dong, H.-W. & Swanson, L. W. Projections from bed nuclei of the stria terminalis, posterior division: Implications for cerebral hemisphere regulation of defensive and reproductive behaviors. *J. Comp. Neurol.* **471**, 396–433 (2004).
38. Davis, M., Walker, D. L., Miles, L. & Grillon, C. Phasic vs Sustained Fear in Rats and Humans: Role of the Extended Amygdala in Fear vs Anxiety. *Neuropsychopharmacology* **35**, 105–135 (2010).

39. Yang, C. F. *et al.* Sexually Dimorphic Neurons in the Ventromedial Hypothalamus Govern Mating in Both Sexes and Aggression in Males. *Cell* **153**, 896–909 (2013).
40. Yang, C. F. & Shah, N. M. Representing Sex in the Brain, One Module at a Time. *Neuron* **82**, 261–278 (2014).
41. Bayless, D. W. *et al.* Limbic Neurons Shape Sex Recognition and Social Behavior in Sexually Naive Males. *Cell* **176**, 1190-1205.e20 (2019).
42. Bayless, D. W. & Shah, N. M. Genetic dissection of neural circuits underlying sexually dimorphic social behaviours. *Philos. Trans. R. Soc. B Biol. Sci.* **371**, 20150109 (2016).
43. Pfaus, J. G. & Heeb, M. M. Implications of Immediate-Early Gene Induction in the Brain Following Sexual Stimulation of Female and Male Rodents. *Brain Res. Bull.* **44**, 397–407 (1997).
44. Valcourt, R. J. & Sachs, B. D. Penile reflexes and copulatory behavior in male rats following lesions in the bed nucleus of the stria terminalis. *Brain Res. Bull.* **4**, 131–133 (1979).
45. Claro, F., Segovia, S., Guilamón, A. & Del Abril, A. Lesions in the medial posterior region of the BST impair sexual behavior in sexually experienced and inexperienced male rats. *Brain Res. Bull.* **36**, 1–10 (1995).
46. Padilla, S. L. *et al.* Agouti-related peptide neural circuits mediate adaptive behaviors in the starved state. *Nat. Neurosci.* **19**, 734–741 (2016).
47. Knoedler, J. R. *et al.* A functional cellular framework for sex and estrous cycle-dependent gene expression and behavior. *Cell* **185**, 654-671.e22 (2022).
48. Lin, D. *et al.* Functional identification of an aggression locus in the mouse hypothalamus. *Nature* **470**, 221–226 (2011).
49. Lee, H. *et al.* Scalable control of mounting and attack by *Esr1*<sup>+</sup> neurons in the ventromedial hypothalamus. *Nature* **509**, 627–632 (2014).
50. Karigo, T. *et al.* Distinct hypothalamic control of same- and opposite-sex mounting behaviour in mice. *Nature* (2020) doi:10.1038/s41586-020-2995-0.
51. Wei, D., Talwar, V. & Lin, D. Neural circuits of social behaviors: innate yet flexible. *Neuron* S0896627321001124 (2021) doi:10.1016/j.neuron.2021.02.012.
52. Hull, E. M. & Dominguez, J. M. Sexual behavior in male rodents. *Horm. Behav.* **52**, 45–55 (2007).

53. Wei, Y.-C. *et al.* Medial preoptic area in mice is capable of mediating sexually dimorphic behaviors regardless of gender. *Nat. Commun.* **9**, 279 (2018).
54. Nair, A. *et al.* *An approximate line attractor in the hypothalamus that encodes an aggressive internal state.* <http://biorxiv.org/lookup/doi/10.1101/2022.04.19.488776> (2022) doi:10.1101/2022.04.19.488776.
55. Wu, Z., Autry, A. E., Bergan, J. F., Watabe-Uchida, M. & Dulac, C. G. Galanin neurons in the medial preoptic area govern parental behaviour. *Nature* **509**, 325–330 (2014).
56. Siegel, A., Roeling, T. A. P., Gregg, T. R. & Kruk, M. R. Neuropharmacology of brain-stimulation-evoked aggression. *Neurosci. Biobehav. Rev.* **23**, 359–389 (1999).
57. Anderson, D. J. Optogenetics, Sex, and Violence in the Brain: Implications for Psychiatry. *Biol. Psychiatry* **71**, 1081–1089 (2012).
58. Lammers, J. H. C. M., Kruk, M. R., Meelis, W. & van der Poel, A. M. Hypothalamic substrates for brain stimulation-induced attack, teeth-chattering and social grooming in the rat. *Brain Res.* **449**, 311–327 (1988).
59. Kruk, M. R. *et al.* Discriminant analysis of the localization of aggression-inducing electrode placements in the hypothalamus of male rats. *Brain Res.* **260**, 61–79 (1983).
60. Remedios, R. *et al.* Social behaviour shapes hypothalamic neural ensemble representations of conspecific sex. *Nature* **550**, 388–392 (2017).
61. Falkner, A. L. *et al.* Hierarchical Representations of Aggression in a Hypothalamic-Midbrain Circuit. *Neuron* **106**, 637-648.e6 (2020).
62. Flexible scaling and persistence of social vocal communication | Nature. <https://www.nature.com/articles/s41586-021-03403>.

## *Chapter 2*

### PREAMBLE

In Chapter I, I summarized our current understanding of the neural circuits underlying mating and fighting behaviors. Briefly, chemical compounds originating from conspecific's urine, anogenital secretions or tear are processed by the olfactory system (AOB and MOB) and transformed into neural representations of conspecific's identity at the level of MeA, and PA. The information encoding conspecific's identity is subsequently transformed into neural representations of mating and fighting from MeA/PA to BNSTpr, and from BNSTpr to MPOA and VMHvl.

To understand what role, do various nuclei of the extended amygdala and the hypothalamus play in mediating the sensory to behavior transformation, I recorded single-unit activity from *Esr1*<sup>+</sup> populations in the MeA, BNSTpr, MPOA and VMHvl using microendoscopes during social interactions. A comparison of the responses in these regions during the investigation phase and consummatory phase of social interactions with male and female conspecifics revealed several interesting features of the system. 1) Neurons in all four regions selectively respond to either male or female conspecifics. 2) MeA neurons responded strongly during the investigation phase and are largely silenced during consummatory behaviors while neurons in BNSTpr, MPOA and VMH responded to both investigation and consummatory behaviors. 3) From MeA to BNSTpr to MPOA, neuronal responses are increasingly selective towards intruder identity and consummatory behaviors. 4) In MeA, BNSTpr and MPOA, the encoding of sex is female biased - there are approximately twice as many of neurons that

responded to female conspecifics compared to neurons that responded to male conspecifics. In VMH, this bias is reversed – there are approximately twice as many neurons that responded to males compared to neurons that responded toward interactions with females.

5) Representations of mating and fighting emerges at the level of BNST<sub>pr</sub> – MPOA / BNST-VMH<sub>v1</sub>. This suggests that BNST<sub>pr</sub> is involved in the transformation of conspecific identity to consummatory behaviors.

The organization and representations of the neural circuits that mediate mating and fighting raises several important questions that motivate the study described in the following section – 1) What's the function of biased sex representations? 2) How do behavior representations emerge from conspecifics identity? 3) What role does BNST<sub>pr</sub> play in the emergence of behavior representations in MPOA and VMH<sub>v1</sub>?

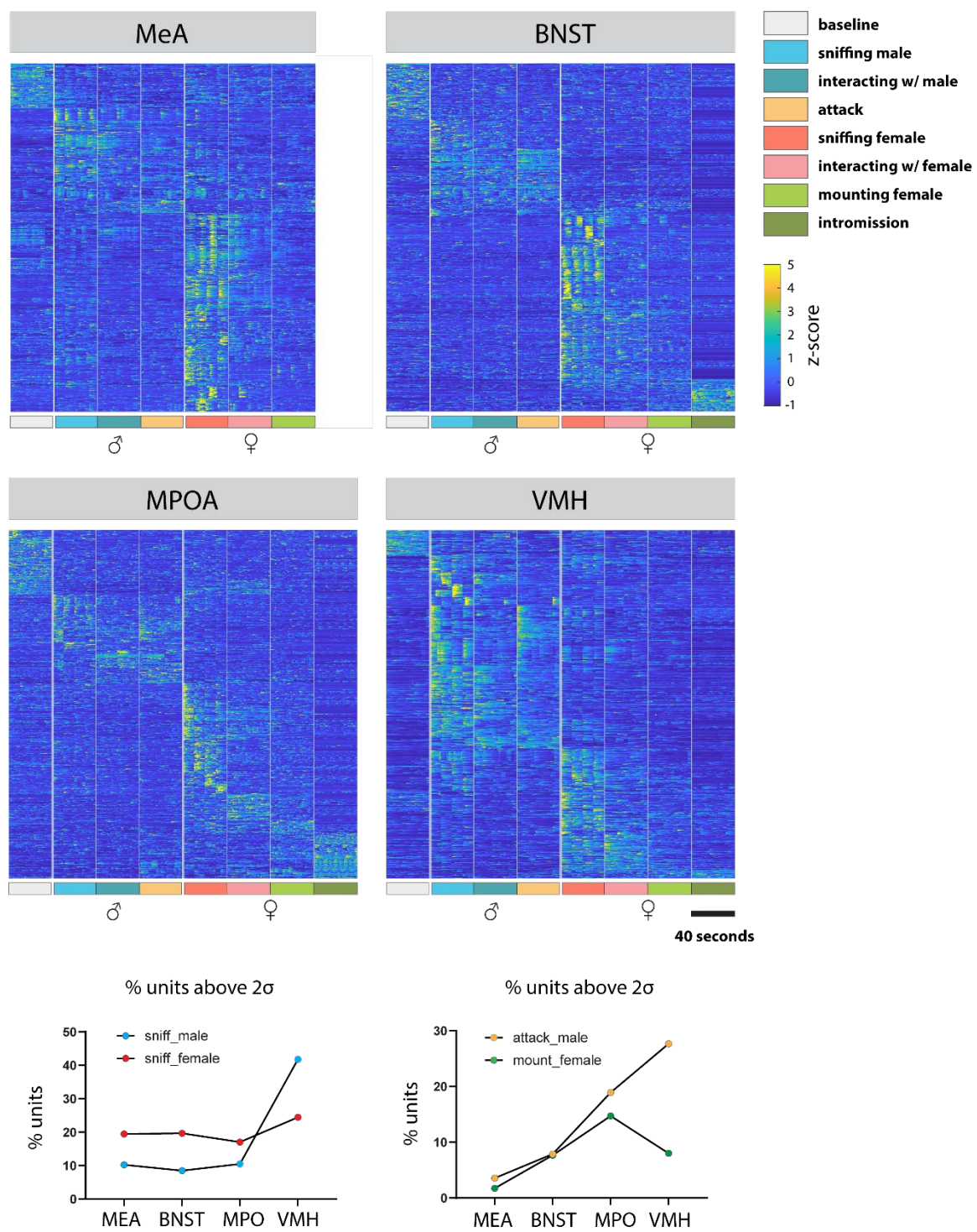


**Figure 1. Activity Raster from  $Esr1^+$  Neurons in MeA, BNST, MPOA and VMH during Social Interactions with Male or Female Conspecifics**

## Chapter 2

### TRANSFORMATIONS AND FUNCTIONS OF NEURAL REPRESENTATIONS IN A SOCIAL BEHAVIOR NETWORK

Yang, B., Karigo, T., and Anderson, D.J. (2022). “Transformations and Functions of Neural Representations in a Social Behavior Network”. *Nature* (accepted)

Mating and aggression are innate social behaviors that are controlled by subcortical circuits in the extended amygdala and hypothalamus<sup>1-4</sup>. The bed nucleus of the stria terminalis, principal subdivision (BNSTpr) is a node that receives input encoding sex-specific olfactory cues from the medial amygdala postero-dorsal (MeApd<sup>5,6</sup>), and which in turn projects to the medial preoptic area (MPOA) and the ventromedial hypothalamus, ventrolateral subdivision (VMHvl), hypothalamic nuclei that control mating<sup>7-9</sup> and aggression<sup>9-14</sup>, respectively<sup>15</sup>. How BNSTpr transforms sex-specific cue representations to control consummatory social behaviors is not yet clear. Previous studies have shown that aromatase<sup>+</sup> BNSTpr (AB) neurons are required for mounting and attack, as well as for female cue preference, implying a function in conspecific sex identification<sup>16</sup>. Here we have performed calcium imaging<sup>17,18</sup> of BNSTpr<sup>Esr1</sup> neurons during male social behaviors, and investigated the effect of silencing these neurons on the coding of sex identity and behavior in the hypothalamus. We find distinct populations of female- vs. male-tuned neurons in BNSTpr, with the former outnumbering the latter by ~2:1, similar to MeApd and MPOA but opposite to VMHvl, where male-tuned neurons predominate<sup>6,9,19</sup>. Chemogenetic silencing of BNSTpr<sup>Esr1</sup> neurons with simultaneous calcium imaging of MPOA<sup>Esr1</sup> or VMHvl<sup>Esr1</sup> neurons revealed, surprisingly, neither a loss of sex-specific representations in the hypothalamus nor a deficiency in female vs. male cue recognition as assessed by ultrasonic vocalizations

(USVs). Instead, sex-specific tuning in VMHvl was inverted from male- to female-dominated, while a switch from sniff- to mount-selective neurons in MPOA failed to occur. These data indicate that BNSTpr<sup>Esr1</sup> neurons control the transition from the appetitive to consummatory phases of male social behaviors via a role in shaping sex- and behavior-specific neural representations in the hypothalamus, independently of any essential role in conspecific sex identification.

We first examined the behavioral effects of silencing BNSTpr<sup>Esr1</sup> neurons in socially experienced males. Chemogenetic silencing<sup>20</sup> significantly reduced mounting and increased sniffing toward females, and reduced attack toward males, consistent with prior observations in inexperienced males<sup>16</sup> (**Extended Data Fig. 1a-m**). Next, we optogenetically silenced<sup>21,22</sup> BNSTpr<sup>Esr1</sup> neurons during either the appetitive or consummatory phases of social interactions with males or females (**Fig. 1**). Silencing BNSTpr<sup>Esr1</sup> cells during approaching or sniffing of males strongly inhibited the transition to, and duration of, attack, but did not significantly alter sniffing itself (**Fig. 1e-g and Extended Data Fig. 1n-q**). Silencing BNSTpr<sup>Esr1</sup> neurons during approaching or sniffing of females significantly reduced the transition to (~2 fold) and duration of (~2.5 fold) mounting (**Fig. 1j-l and Extended Data Fig. 1t**), while extending the total time spent sniffing (**Extended Data Fig. 1r, s**). Interestingly, while optogenetic silencing during attack interrupted this behavior (**Fig. 1h, i**), silencing during mounting had no effect (**Fig. 1m, n**). Optogenetic silencing of BNSTpr<sup>Esr1</sup> terminals<sup>23-25</sup> in MPOA or VMHvl revealed that the sniff-to-mount transition toward females is primarily dependent upon activity in the BNSTpr→MPOA projection (**Extended Data Fig. 2l**), while activity in the BNSTpr→VMHvl projection is necessary for attack (**Extended Data Fig. 2i**). These data confirm that BNSTpr<sup>Esr1</sup> activity is required to gate the transition

from appetitive to consummatory male social behaviors towards both sexes<sup>16,26</sup>, and show that this gating occurs via its projections to MPOA and VMHvl, respectively. They additionally demonstrate a requirement for BNSTpr<sup>Esr1</sup> activity during ongoing attack (but not ongoing mounting)<sup>27</sup>.

A previous study concluded that BNSTpr<sup>AB</sup> neurons are required for intruder sex recognition, based on male vs. female cue-preference tests<sup>16</sup>. Males emit USVs in response to female but not male urine<sup>9,28</sup>. We performed bilateral optogenetic silencing of BNSTpr<sup>Esr1</sup> neurons using GtACR2 and tested both cue preference and USVs. Consistent with earlier data<sup>16</sup>, we observed a reduced preference for female over male cues (**Extended Data Fig. 1r, w**). Surprisingly, however, there was no loss of USVs towards female urine or intact females (**Extended Data Fig. 1s, x**). Thus, while silencing BNSTpr<sup>Esr1</sup> neurons reduced the males' preference for female cues, it did not eliminate their ability to respond specifically to those cues.

Previous bulk calcium measurements of BNSTpr<sup>AB</sup> neurons suggested that intruder sex is encoded by overall activity, such that strong activity indicates a female, while weaker activity indicates a male<sup>16</sup>. To reveal how sex and social behaviors are represented in BNSTpr at the single cell level, we imaged BNSTpr<sup>Esr1</sup> neurons (a subset partially overlapping with, but larger than, AB neurons<sup>29</sup>) expressing jRCaMP7f<sup>30</sup> using a microendoscope (Inscopix, Inc.; **Fig. 2a**). By utilizing a prism-coupled gradient refractive index (GRIN) lens, we were able to image the dorso-ventral extent of this elongated nucleus in behaving mice, yielding almost three-fold more units per session compared to conventional cylindrical GRIN lenses (**Fig. 2b, c; Extended Data Fig. 3a-h**).

We first performed trials in which male, female, or toy mice suspended by their tails were presented to male residents in their home cage (5 trials each, 10s per trial), permitting sniffing but not mounting or attack<sup>19</sup>. We observed distinct BNSTpr<sup>Esr1</sup> populations responding to either male or female “dangled” intruders, but not to toy mice (**Fig. 2c, f and Extended Data Fig. 4a**). The average down-sampled bulk calcium peak response (5 x 10 s trials) to female intruders was ~2 times that of male intruders (**Fig. 2d**), explaining prior bulk calcium imaging results<sup>16</sup>. Analysis of single unit calcium responses (extracted using CNMF-E<sup>31,32</sup>, see Methods) to intruders revealed that 27% of the units were female preferring (determined by choice probability<sup>19</sup> (CP); see Methods) vs. 15% that were male preferring (**Fig. 2g, h and Extended Data Fig. 4e**). Qualitatively similar results were obtained by imaging of BNSTpr<sup>AB</sup> neurons<sup>16</sup>, a functionally equivalent subset of BNSTpr<sup>Esr1</sup> neurons<sup>33</sup> (**Extended Data Fig. 4j-l**). A temporal linear decoder<sup>9</sup> (Support Vector Machine, SVM) trained on BNSTpr<sup>Esr1</sup> data could identify the sex of a dangled intruder, in held-out test data, within 1 sec of intruder presentation ( $p < 0.0001$ ) compared to shuffled control data (**Fig. 2i**), suggesting that olfactory cues are sufficient to generate distinct cellular representations of intruder sex in BNSTpr. Male and female-preferring cells were not topographically segregated but appeared intermingled (**Fig. 2e**).

We asked next whether BNSTpr<sup>Esr1</sup> population activity also represents distinct social behaviors, by imaging under conditions where the resident male freely interacted with male or female intruders (4,585 units from 15 mice). We constructed raster plots of population activity during a 10s interval from each of 8 different conditions (baseline, sniff male/female, interact with male/female, attack, mount, and intromission; see Methods) (**Fig. 2j**). Overall, ~33% of imaged units were active ( $>2\sigma$ ) during female encounters, while ~25% were

activated during male encounters. Of these, ~45% were activated during appetitive and/or consummatory behaviors toward the intruder (**Fig. 2k, orange circle and Extended Data Fig. 4b, c, d**). Approximately 77% of the female-preferring (511 out of 660) and 70% of the male-preferring (259 out of 377) units that exhibited a sex preference during dangling trials retained this preference during subsequent unrestrained social interactions (**Fig. 2l**).

We computed the tuning of BNSTpr<sup>Esr1</sup> neurons for intruder sex or specific behaviors using choice probability<sup>19</sup>, a binary comparison. Among all units that were active during appetitive and/or consummatory behaviors, a larger percentage were male- or female-tuned (20% male, 33% female), than were consummatory behavior-tuned (7% attack, 9% mount) (**Fig. 2m and Extended Data Fig. 4f**). Principle Component (PC) analysis indicated that the largest source of variance in neural activity was explained by intruder sex (**Fig. 2n, PC1**). Linear regression (Methods) revealed that intruder sex accounted for over 30% of the observed variance, while only 9% and 8% of the variance was explained by behavior towards females and males, respectively (**Fig. 2o and Extended Data Fig. 3i**). Together, these results suggest that a major source of variance in BNSTpr<sup>Esr1</sup> population activity is the sex of the intruder (or an internal motive state highly correlated with intruder sex), and that sex is represented by population coding, as in MPOA and VMHvl<sup>9,19</sup>.

We next directly compared representations of intruder sex in MeApd, BNSTpr, VMHvl, and MPOA Esr1<sup>+</sup> neurons, imaged under identical conditions (**Fig. 3a-f; Extended Data Fig. 3i**). Like BNSTpr, both the MPOA and VMHvl Esr1<sup>+</sup> populations contained distinct subsets of male- and female-preferring cells<sup>9,19</sup>. However, whereas among MPOA<sup>Esr1</sup> and MeApd<sup>Esr1</sup> neurons female-preferring outnumbered male-preferring units, by about 2:1

(as in BNSTpr<sup>Esr1</sup>), among VMHvl<sup>Esr1</sup> neurons the ratio was reversed (1:2; **Fig. 3o, p**, gray bars; **Extended Data Figs. 3i and 5p-s**), consistent with earlier results<sup>6,9,19</sup>.

Since BNSTpr projects directly to MPOA and VMHvl<sup>34</sup> and encodes conspecific sex identity<sup>16</sup>, we hypothesized that inhibiting BNSTpr<sup>Esr1</sup> neurons should eliminate sex-specific representations in MPOA and VMHvl. To test this, we combined chemogenetic silencing of BNSTpr<sup>Esr1</sup> neurons using hM4Di<sup>20</sup>, with microendoscopic imaging of VMHvl<sup>Esr1</sup> or MPOA<sup>Esr1</sup> neurons expressing jGCaMP7f<sup>30</sup> (**Fig. 3b,c and Extended Data Fig. 5a-o**), a method we call “ChemoScope”. Imaging during presentation of dangled intruders was performed both in control (“pre-CNO”, i.e. saline-injected) and experimental (CNO-injected) conditions in the same animals, to permit within-subject comparisons at the single-cell level.

Surprisingly, silencing BNSTpr<sup>Esr1</sup> neurons during presentation of dangled male or female intruders did not eliminate sex-specific representations in VMH and MPOA (**Fig. 3e vs. h; 3f vs. i**). A small, but statistically significant, decrease in the separation of male vs. female representations was observed in VMHvl, as indicated by the Pearson’s correlation coefficient and Mahalanobis distance ratio<sup>19</sup> (**Fig. 3j, k**, VMHvl, opposite sex, gray vs. maroon bars). However, the performance of linear decoders of intruder sex, trained on data from MPOA<sup>Esr1</sup> or VMHvl<sup>Esr1</sup> neurons, was only slightly decreased in MPOA by silencing BNSTpr<sup>Esr1</sup> neurons, and was still well above chance (computed using shuffled data). Sex decoding in VMHvl was unaffected (**Fig. 3l-m**). There was a slight increase in the difference between average z-scored responses to females vs. males in MPOA, and a larger increase in VMHvl (**Fig. 3n**), likely reflecting a decrease in the mean response to male intruders in both

nuclei, and an increase in the mean response to female intruders in VMHvl (**Extended Data Fig. 6q-s**).

In contrast to these relatively subtle effects, silencing BNSTpr<sup>Esr1</sup> neurons unexpectedly inverted the 2:1 ratio of male- to female-tuned units in VMHvl, to the female-dominant ratio seen in MPOA (~2:1; **Fig. 3p**; VMH, gray vs. maroon bars). This reversal of sex bias in VMHvl reflected both a decrease in male-preferring units, and an increase in female-preferring units (**Fig. 3o**). In MPOA, by contrast, the ratio of female- to male-preferring units was slightly increased by BNSTpr silencing (**Fig. 3p, q** and **Extended Data Fig. 6s, t**). Together, these data indicate that the activity of BNSTpr<sup>Esr1</sup> neurons is not required for the neural coding of intruder sex identity by MPOA<sup>Esr1</sup> and VMHvl<sup>Esr1</sup> neurons. Rather, it is required to invert, in VMHvl, the female bias in population representations of intruder sex seen in BNSTpr, MPOA and MeApd<sup>6</sup>, to a male bias.

The inversion of sex tuning bias in VMHvl caused by silencing BNSTpr<sup>Esr1</sup> neurons could be explained by two mechanisms: conversion, in which a subset of initially male-tuned VMHvl<sup>Esr1</sup> neurons switched to female-tuning; or selection, in which new female-tuned units appeared and replaced silenced male-tuned units. To distinguish these possibilities, we registered the spatial maps imaged during pre-CNO (saline-injected) and CNO sessions within the same animals, and tracked single unit responses<sup>19</sup> (over 60% of all recorded MPOA<sup>Esr1</sup> units and over 55% of all recorded VMHvl<sup>Esr1</sup> units) during male and female dangling trials, before and after CNO treatment (**Fig. 4 a, i**). Consistent with the data from all (i.e., non-tracked) units (**Fig. 3p**), we observed an approximate inversion of the ratio of male- to female-preferring VMHvl<sup>Esr1</sup> neurons, from 2m:1f before, to 1m:1.7f after, BNSTpr

silencing (**Fig. 4b, c**). In contrast, the ratio of female- to male-preferring MPOA<sup>Esr1</sup> tracked units was slightly increased in CNO, from 1.5f:1m to 2f:1m (**Fig. 4j, k**; cf. **Fig. 3p**).

Single-unit tracking revealed the source of the additional female-preferring Esr1<sup>+</sup> units in VMHvl following BNSTpr silencing (**Fig. 4h**). Almost a quarter of the female-preferring units (24%) in CNO-treated animals derived from pre-CNO male-preferring units that switched sex-preference (**Fig. 4h**, blue; **Extended Data Fig. 7q, s, VMH**, red bar). Twenty percent of the female-preferring units after CNO derived from pre-CNO “co-active” (i.e., responsive to both sexes) units that lost male preference (**Fig. 4h**, yellow; **Extended Data Fig. 7l-n**), or from initially non-active units that gained female preference (20%) (**Fig. 4h**, grey; **Extended Data Fig. 7g-i**). Thus, the inversion of the male sex-tuning bias in VMHvl following BNSTpr silencing was due mostly to the conversion of initially male-preferring, or dual-responsive, units to female-preferring units (**Fig. 4g**).

In MPOA, following BNSTpr<sup>Esr1</sup> silencing a substantial proportion of initially male-preferring, co-active or non-active units converted to female-preferring units (**Fig. 4o**). However, this conversion was partially offset by the silencing of some initially female-preferring units (**Fig. 4o, Extended Data Fig. 7c, right; f, k, n**). Consequently, the overall proportion of female-preferring MPOA<sup>Esr1</sup> units did not change greatly after CNO (**Fig. 4j, k, p**). In contrast to VMHvl, therefore, where BNSTpr<sup>Esr1</sup> silencing converted initially non-female-selective to female-selective units, in MPOA the slight increase in female-tuned units (**Fig. 3n, p**) was primarily due to a substitution of new female-tuned units for others that became inactive. There was no significant change in the percentage of tracked male- or female-tuned units in either MPOA or VMHvl, in animals injected with saline on two consecutive days (**Extended Data Fig. 5p-s**).

To investigate how silencing BNSTpr<sup>Esr1</sup> neurons affects hypothalamic activity during mounting and attack, we tracked single-unit responses in MPOA<sup>Esr1</sup> or VMHvl<sup>Esr1</sup> neurons before and after unilateral silencing of BNSTpr in freely behaving animals (**Fig. 5a**). Because BNSTpr→hypothalamic projections are primarily ipsilateral<sup>34</sup>, by performing silencing and imaging on one side of the brain while leaving the other unperturbed, this design allows normal social behavior in CNO, due to redundant contralateral circuits. Thus, any observed changes in neural activity cannot be due to a loss of social behavior, which requires bi-lateral BNSTpr<sup>Esr1</sup> silencing (**Fig. 1b and Extended Data Fig. 1a**).

In MPOA, female-directed sniffing vs. mounting were represented by largely distinct groups of neurons (**Fig. 5b**, pre-CNO). CNO silencing of BNSTpr<sup>Esr1</sup> significantly decreased the activity of mount-selective cells, with a concomitant increase in sniff-active cells during mounting behavior (**Fig. 5c-f**). Thus, during BNSTpr<sup>Esr1</sup> silencing the cellular responses during female-directed sniffing vs. mounting became more similar than in controls (**Fig. 5b**, CNO). A corresponding decrease in the fraction of variance in neural activity explained by female-directed behaviors was observed as well (**Fig. 5g**).

In contrast to MPOA, in VMHvl male-directed sniffing and attack are represented by largely overlapping neuronal populations (**Fig. 5h**)<sup>9,19</sup>. Following BNSTpr<sup>Esr1</sup> silencing, both the average activity of those neurons normally active during attack behavior, as well as well as the percentage of attack-active neurons, were significantly reduced (**Fig 5j-l**). There was also a decrease in the number of male-selective VMHvl<sup>Esr1</sup> neurons (**Fig. 5i**, CNO; see also **Fig. 4b, c**). Together these data show that in MPOA, unilateral BNSTpr<sup>Esr1</sup> silencing extended the activity of normally sniff-selective cells into the mounting phase, and decreased the activity of mount-selective cells during mounting. In VMHvl it reduced the activity of

both mixed-selectivity and attack-selective cells during the attack, but not the sniff, phase. Thus, silencing of BNSTpr<sup>Esr1</sup> neurons in freely behaving males during social interactions caused distinct changes in neural representations of consummatory behavior in VMHvl and MPOA. However the average response to males and females in both nuclei remained unchanged (**Fig. 3g** ♀♂ Avg.).

BNSTpr lies at the interface between the encoding of sex-specific olfactory cues in the medial amygdala and of motive drive states in the hypothalamus that control the consummatory phases of social behaviors. Previous studies suggested that it encodes and is essential for the identification of conspecific sex via an intensity code<sup>16</sup>, with its requirement for consummatory behaviors presumably reflecting the former function. The data presented here suggest a revision of this view.

First, while we confirm that BNSTpr neural activity contains a representation of conspecific sex identity, our cellular resolution calcium imaging reveals that female vs. male identity is not encoded by a higher vs. lower level of activity in this structure, respectively, as indicated by previous bulk calcium measurements<sup>16</sup>, but rather by a cell identity code: distinct subpopulations of BNSTpr<sup>Esr1</sup> neurons are tuned to males vs. females. Because the female-tuned neurons outnumber the male-tuned cells by ~2:1, a higher level of BNSTpr activity is observed in response to females than males when bulk calcium signals are measured by fiber photometry<sup>16</sup>. This ~2:1 female tuning bias is similar to that in MeApd<sup>6</sup> and MPOA<sup>9</sup>, but is inverted in VMHvl<sup>19</sup>. Thus, at each node in the processing pathway from MeApd→BNSTpr→MPOA/VMHvl, intruder sex is represented as a cell identity code (**Extended Data Fig. 3i**).

Second, while BNSTpr<sup>Esr1</sup> neurons represent intruder sex identity, its function is not required to identify conspecific sex<sup>15</sup>. Although we confirmed that BNSTpr<sup>Esr1</sup> neuronal activity is required for males to show a preference for female cues<sup>16</sup>, we find surprisingly that it is not required for them to identify and distinguish females vs males: emission of USVs is only observed in response to female and not male cues, as in control males<sup>8,9</sup>. Consistent with this, intruder sex can be decoded equally well from MPOA<sup>Esr1</sup> or VMHvl<sup>Esr1</sup> neural activity in the presence or absence of BNSTpr<sup>Esr1</sup> activity. While the ability to identify and distinguish females vs. males is clearly necessary for a male to display a preference for females, it does not follow that all deficits in female *preference* necessarily reflect deficient sex identification. Our results call into question the widespread use of male vs female preference assays as a surrogate measure of conspecific sex identification.

Interestingly, female-biased conspecific sex-tuned neural representations have been observed in the prefrontal cortex as well, where they play a role in sex preference behavior<sup>35</sup>. The causal relationship between conspecific sex tuning in cortical vs. subcortical regions remains to be determined. Our results also raise the question of whether the weak male-biased sex-tuning observed in MeApd<sup>6</sup> in female mice extends to the structures we have investigated here. Previous bulk calcium imaging studies suggest that BNSTpr AB neurons do not encode intruder sex in females<sup>15</sup>, but single-cell analysis was not performed.

Third, while it may be intuitive to think that MeApd, BNSTpr and the hypothalamus each play distinct functional roles in the transformation of sex-specific social cues into behavior, such as social cue representation, sex identification and action selection, respectively, our data on the transformations in neural representations that occur as information flows through this circuit do not support such a hierarchical view. Instead, we

find that intruder sex identity is represented in each of these regions in a distributed manner. In MPOA, the variance explained by behavior is higher than that in BNSTpr (and in MeApd) (**Fig. 5g, m** and **Extended Data Fig. 3i**). In contrast, the variance explained by behavior in VMHvl is higher than that in BNSTpr, largely because VMHvl has very few neurons tuned to specific phases of social behavior<sup>19</sup>. Rather, the main transformation that occurs from BNSTpr to VMHvl is an inversion of the ratio of sex-tuned neurons, from female-dominant in the former to male-dominant in the latter (**Fig. 5m**).

Surprisingly, when BNSTpr<sup>Esr1</sup> neurons were silenced chemogenetically, the male sex-tuning bias in VMHvl flipped to a female-tuning bias. Apparently, female tuning-dominant Esr1<sup>+</sup> GABAergic neurons in BNSTpr are required to suppress female-specific tuning among VMHvl<sup>Esr1</sup> glutamatergic neurons. Consistent with this, retrograde imaging indicated that female-biased tuning is present among BNSTpr<sup>Esr1</sup> neurons that project to VMHvl (as well as to MPOA; **Extended Data Fig. 9**). The mechanism whereby the female-biased sex representation in BNSTpr is transformed into a male-biased representation in VMHvl remains to be established, and may involve differential male- or female-biased inputs from other regions, such as the posterior amygdala<sup>36–38</sup>. In contrast, silencing BNSTpr did not significantly alter the female-dominant sex bias in MPOA (if anything it was slightly increased); rather it reduced the variance explained by behavior (**Fig. 5g**). Together, these data indicate a requirement for BNSTpr<sup>Esr1</sup> neuronal activity in shaping the representations of social behavior and conspecific sex in MPOA and VMHvl, respectively (**Fig. 5m**).

Finally, our results indicate that the inhibition of mounting and attack behavior that occurs upon BNSTpr<sup>Esr1</sup> silencing is not secondary to a deficiency in sex identification<sup>16</sup>. Rather, the failure to transition from appetitive to consummatory social behavior following silencing

reflects changes in the pattern of sex- and behavior-specific tuning among VMHvl<sup>Esr1</sup> and MPOA<sup>Esr1</sup> neurons, with no loss of sex identity coding. In what follows we suggest relatively simple explanations for how these circuit-level “mutant phenotypes” may lead to the observed behavioral phenotypes. However, this causality is not directly demonstrated, and more complex explanations are certainly possible.

In MPOA, many  $Esr1^+$  neurons are tuned for specific behaviors, including sniffing or mounting (**Fig. 2j**). Accordingly, as males transition from sniffing to mounting, sniff-selective neurons become less active while mount-selective neurons become more active. When BNSTpr<sup>Esr1</sup> neurons are silenced, this change in MPOA neural representations of social behavior is muted: sniff-selective neurons continue to be active as the animal transitions to mounting, while mount-selective neurons exhibit reduced activity (**Fig. 5a-e**). Since ~95% of BNSTpr neurons are GABAergic<sup>16,26,39,40</sup>, these observations suggest that in normal animals during sniffing, sniff-selective neurons (or another MPOA subpopulation) may inhibit mount-selective neurons. In order to transition to mounting, input from BNSTpr<sup>Esr1</sup> GABAergic neurons may be required to inhibit the sniff-selective population, thereby dis-inhibiting the mount-selective cells (**Fig. 5n**). In the absence of BNSTpr<sup>Esr1</sup> activity, mount-selective cells are insufficiently active and so this transition is blocked; instead the male continues to sniff the female (**Extended Data Fig. 1b, lower**).

In VMHvl, sniff- and attack-active cells are largely overlapping (**Fig. 5i**) but are sex-specific<sup>9,19</sup>, with male-tuned neurons outnumbering female-tuned cells by ~2:1. During attack, primarily male-tuned neurons are active<sup>9,19</sup>. Optogenetic experiments<sup>9,11,13</sup> and computational modeling<sup>41</sup> suggest that the activity of VMHvl<sup>Esr1</sup> neurons must reach a certain threshold in order for males to transition from sniff to attack. In the absence of BNSTpr<sup>Esr1</sup>

activity female-tuned neurons become dominant in VMHvl, so the number and activity of male-selective neurons are reduced (**Fig. 4c, Extended Data Fig. 8a**). This reduction may prevent activity in the male-tuned population from reaching the threshold necessary to transition to attack (**Fig. 5j-l, n**), although increased inhibition from neighboring GABAergic neurons may contribute as well. Together these data suggest that activity in BNSTpr<sup>Esr1</sup> neurons controls sex- and behavior-tuning in MPOA and VMHvl in a manner essential for the transition from sniffing to mounting or attack, respectively.

Functional perturbations and observational studies often yield different views of brain function<sup>42</sup>. Our results demonstrate how calcium imaging can be combined with manipulations of neural activity in freely moving animals to identify and link circuit-level to behavioral phenotypes. This combined approach allows an integration of observational and perturbational data to reveal both the transformations in neural representations that occur as information flows through a circuit, and the potential function of such transformations in the control of behavior. Future studies should reveal the detailed cellular and synaptic mechanisms that underlie these essential transformations.

**Acknowledgements**

We thank A. Kennedy and A. Nair for advice on miniscope data analysis, M. Hui and C. Kim for assisting with animal surgery and behavior experiments, M. Zelikowsky for advice on statistical analysis, W. Hong for pilot experiments performed in BNSTpr, X. Da, J. Chang and X. Wang for histology, Y. Huang for genotyping, Caltech OLAR staff for animal care, J. Costanza for mouse colony management, M. Schnitzer, A. Vinograd and B. Weissbourd for constructive comments on the manuscript, C. Chiu for laboratory management and G. Mancuso for administrative assistance, members of the Anderson laboratory for helpful comments on this project. This paper was supported by NIH grants MH070053, MH112593, NS123916 and by the Simons Collaboration on the Global Brain. D.J.A. is an investigator of the Howard Hughes Medical Institute.

**Author contributions**

B.Y. performed experiments, analyzed data and prepared figures. T.K performed retrograde tracing experiments. B.Y. and D.J.A. designed the study and wrote the paper.

**Competing interests**

The authors declare no competing interests.

## References

1. Yang, C. F. & Shah, N. M. Representing Sex in the Brain, One Module at a Time. *Neuron* **82**, 261–278 (2014).
2. Anderson, D. J. Circuit modules linking internal states and social behaviour in flies and mice. *Nat. Rev. Neurosci.* **17**, 692–704 (2016).
3. Hashikawa, K., Hashikawa, Y., Falkner, A. & Lin, D. The neural circuits of mating and fighting in male mice. *Curr. Opin. Neurobiol.* **38**, 27–37 (2016).
4. Chen, P. & Hong, W. Neural Circuit Mechanisms of Social Behavior. *Neuron* **98**, 16–30 (2018).
5. Bergan, J. F., Ben-Shaul, Y. & Dulac, C. Sex-specific processing of social cues in the medial amygdala. *eLife* **3**, e02743 (2014).
6. Li, Y. *et al.* Neuronal Representation of Social Information in the Medial Amygdala of Awake Behaving Mice. *Cell* **171**, 1176-1190.e17 (2017).
7. Simerly, R. B. Wired for Reproduction: Organization and Development of Sexually Dimorphic Circuits in the Mammalian Forebrain. *Annu. Rev. Neurosci.* **25**, 507–536 (2002).
8. Wei, Y.-C. *et al.* Medial preoptic area in mice is capable of mediating sexually dimorphic behaviors regardless of gender. *Nat. Commun.* **9**, 279 (2018).
9. Karigo, T. *et al.* Distinct hypothalamic control of same- and opposite-sex mounting behaviour in mice. *Nature* (2020) doi:10.1038/s41586-020-2995-0.
10. Ogawa, S. *et al.* Abolition of male sexual behaviors in mice lacking estrogen receptors  $\alpha$  and  $\beta$  ( $\alpha\beta$ ERKO). *Proc. Natl. Acad. Sci.* **97**, 14737 (2000).

11. Lin, D. *et al.* Functional identification of an aggression locus in the mouse hypothalamus. *Nature* **470**, 221–226 (2011).
12. Yang, T. *et al.* Social Control of Hypothalamus-Mediated Male Aggression. *Neuron* **95**, 955-970.e4 (2017).
13. Lee, H. *et al.* Scalable control of mounting and attack by Esr1+ neurons in the ventromedial hypothalamus. *Nature* **509**, 627–632 (2014).
14. Yang, C. F. *et al.* Sexually Dimorphic Neurons in the Ventromedial Hypothalamus Govern Mating in Both Sexes and Aggression in Males. *Cell* **153**, 896–909 (2013).
15. Wei, D., Talwar, V. & Lin, D. Neural circuits of social behaviors: innate yet flexible. *Neuron* S0896627321001124 (2021) doi:10.1016/j.neuron.2021.02.012.
16. Bayless, D. W. *et al.* Limbic Neurons Shape Sex Recognition and Social Behavior in Sexually Naive Males. *Cell* **176**, 1190-1205.e20 (2019).
17. Ghosh, K. K. *et al.* Miniaturized integration of a fluorescence microscope. *Nat. Methods* **8**, 871–878 (2011).
18. Ziv, Y. *et al.* Long-term dynamics of CA1 hippocampal place codes. *Nat. Neurosci.* **16**, 264–266 (2013).
19. Remedios, R. *et al.* Social behaviour shapes hypothalamic neural ensemble representations of conspecific sex. *Nature* **550**, 388–392 (2017).
20. Armbruster, B. N., Li, X., Pausch, M. H., Herlitze, S. & Roth, B. L. Evolving the lock to fit the key to create a family of G protein-coupled receptors potently activated by an inert ligand. *Proc. Natl. Acad. Sci.* **104**, 5163–5168 (2007).

21. Govorunova, E. G., Sineshchekov, O. A., Janz, R., Liu, X. & Spudich, J. L. Natural light-gated anion channels: A family of microbial rhodopsins for advanced optogenetics. *Science* **349**, 647–650 (2015).
22. Mahn, M. *et al.* High-efficiency optogenetic silencing with soma-targeted anion-conducting channelrhodopsins. *Nat. Commun.* **9**, 4125 (2018).
23. Gradinaru, V. *et al.* Molecular and Cellular Approaches for Diversifying and Extending Optogenetics. *Cell* **141**, 154–165 (2010).
24. Mahn, M., Prigge, M., Ron, S., Levy, R. & Yizhar, O. Biophysical constraints of optogenetic inhibition at presynaptic terminals. *Nat. Neurosci.* **19**, 554–556 (2016).
25. Zhang, C. *et al.* Optimized photo-stimulation of halorhodopsin for long-term neuronal inhibition. *BMC Biol.* **17**, 95 (2019).
26. Knoedler, J. R. *et al.* A functional cellular framework for sex and estrous cycle-dependent gene expression and behavior. *Cell* S009286742101494X (2022) doi:10.1016/j.cell.2021.12.031.
27. Padilla, S. L. *et al.* Agouti-related peptide neural circuits mediate adaptive behaviors in the starved state. *Nat. Neurosci.* **19**, 734–741 (2016).
28. Nyby, J., Wysocki, C. J., Whitney, G. & Dizinno, G. Pheromonal regulation of male mouse ultrasonic courtship (*Mus musculus*). *Anim. Behav.* **25**, 333–341 (1977).
29. Stanić, D. *et al.* Characterization of Aromatase Expression in the Adult Male and Female Mouse Brain. I. Coexistence with Oestrogen Receptors  $\alpha$  and  $\beta$ , and Androgen Receptors. *PLoS ONE* **9**, e90451 (2014).
30. Dana, H. *et al.* High-performance calcium sensors for imaging activity in neuronal populations and microcompartments. *Nat. Methods* **16**, 649–657 (2019).

31. Pnevmatikakis, E. A. *et al.* Simultaneous Denoising, Deconvolution, and Demixing of Calcium Imaging Data. *Neuron* **89**, 285–299 (2016).
32. Zhou, P. *et al.* Efficient and accurate extraction of in vivo calcium signals from microendoscopic video data. *eLife* **7**, e28728 (2018).
33. Knoedler, J. R. *et al.* A functional cellular framework for sex and estrous cycle-dependent gene expression and behavior. *Cell* **185**, 654-671.e22 (2022).
34. Dong, H.-W. & Swanson, L. W. Projections from bed nuclei of the stria terminalis, posterior division: Implications for cerebral hemisphere regulation of defensive and reproductive behaviors. *J. Comp. Neurol.* **471**, 396–433 (2004).
35. Kingsbury, L. *et al.* Cortical Representations of Conspecific Sex Shape Social Behavior. *Neuron* **107**, 941-953.e7 (2020).
36. Stagkourakis, S., Spigolon, G., Liu, G. & Anderson, D. J. Experience-dependent plasticity in an innate social behavior is mediated by hypothalamic LTP. *Proc. Natl. Acad. Sci.* **117**, 25789–25799 (2020).
37. Yamaguchi, T. *et al.* Posterior amygdala regulates sexual and aggressive behaviors in male mice. *Nat. Neurosci.* **23**, 1111–1124 (2020).
38. Zha, X. *et al.* VMHvl-Projecting Vglut1+ Neurons in the Posterior Amygdala Gate Territorial Aggression. *Cell Rep.* **31**, 107517 (2020).
39. Welch, J. D. *et al.* Single-Cell Multi-omic Integration Compares and Contrasts Features of Brain Cell Identity. *Cell* **177**, 1873-1887.e17 (2019).
40. Moffitt, J. R. *et al.* Molecular, spatial, and functional single-cell profiling of the hypothalamic preoptic region. *Science* **362**, eaau5324 (2018).

41. Nair, A. *et al.* An approximate line attractor in the hypothalamus that encodes an aggressive internal state. <http://biorxiv.org/lookup/doi/10.1101/2022.04.19.488776> (2022) doi:10.1101/2022.04.19.488776.
42. Jazayeri, M. & Afraz, A. Navigating the Neural Space in Search of the Neural Code. *Neuron* **93**, 1003–1014 (2017).
43. Daigle, T. L. *et al.* A Suite of Transgenic Driver and Reporter Mouse Lines with Enhanced Brain-Cell-Type Targeting and Functionality. *Cell* **174**, 465–480.e22 (2018).
44. Franklin, K. B. J. & Paxinos, G. *Paxinos and Franklin's The mouse brain in stereotaxic coordinates.* (2013).
45. Segalín, C. *et al.* The Mouse Action Recognition System (MARS) software pipeline for automated analysis of social behaviors in mice. *eLife* **10**, e63720 (2021).
46. Friedrich, J., Zhou, P. & Paninski, L. Fast online deconvolution of calcium imaging data. *PLOS Comput. Biol.* **13**, e1005423 (2017).
47. Shadlen, M., Britten, K., Newsome, W. & Movshon, J. A computational analysis of the relationship between neuronal and behavioral responses to visual motion. *J. Neurosci.* **16**, 1486–1510 (1996).
48. McInnes, L., Healy, J. & Melville, J. UMAP: Uniform Manifold Approximation and Projection for Dimension Reduction. (2020).

Figure 1

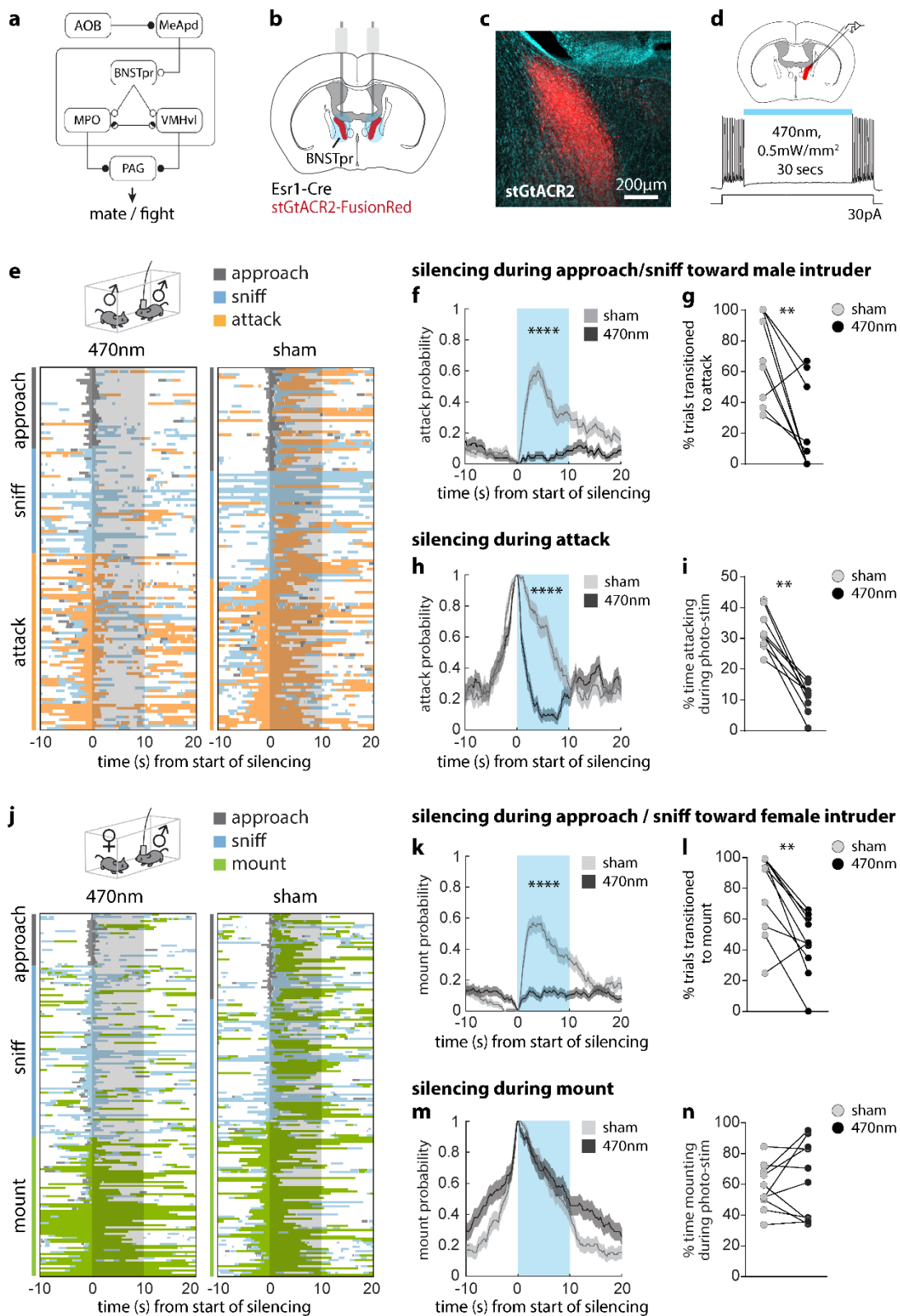


**Figure 1: BNSTpr<sup>Esr1</sup> neurons are necessary for the transition from appetitive to consummatory social behaviors in sexually experienced male mice.**

**a**, Schematic of circuit under study. Open circles, inhibitory connections; closed circles, excitatory connections. **b**, Illustration of bilateral optogenetic silencing in BNSTpr. **c**, Representative image showing stGtACR2 expression in BNSTpr. Similar expression patterns were observed in all animals tested (n = 10). **d**, Whole cell voltage clamp showing light mediated silencing of BNSTpr<sup>Esr1</sup> neurons in an acute slice preparation. **e, j**, Raster plots showing distribution of social behaviors relative to optogenetic silencing. **f, h, k, m**, Mean probability of behavior occurring relative to onset of optogenetic silencing. **g, l**, percent of trials that transitioned to attack (**g**) or mount (**l**). **i, n**, Duration of attack (**i**) or mount (**n**) as a percentage of the 10s optogenetic silencing interval. Statistics: two-sided Wilcoxon signed-rank test (**g, i, l, n**), two-sided Kolmogorov-Smirnov test (**f, h, k, m**). Values are plotted as mean  $\pm$  SEM. \*\*\*\*p < 0.0001; \*\*\*p < 0.001; \*\*p < 0.01; \*p < 0.05. Male-male trials: n=131 stim and 125 sham trials pooled from 10 mice. Male-female trials: n =181 stim and 170 sham trials pooled from 10 mice.

Figure 2

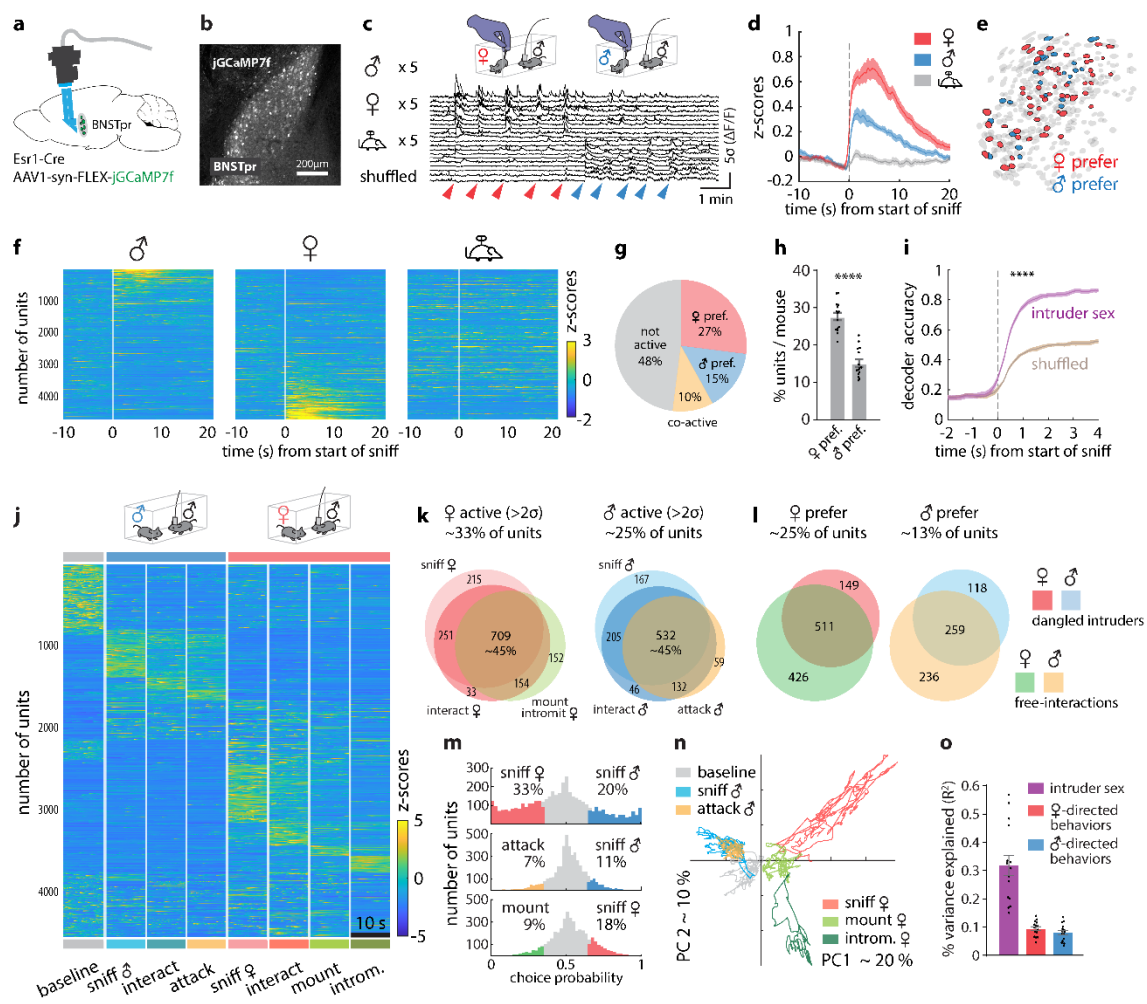


**Figure 2: BNSTpr<sup>Esr1</sup> neurons represent intruder sex via a cell-identity code.**

**a**, Illustration of BNSTpr miniscope imaging using a prism-coupled GRIN lens. **b**, Representative image showing jGCaMP7f expression in BNSTpr. Similar expression patterns were observed in 20 mice. **c**, Imaging experiment paradigm and raw  $\Delta F/F$  of responses from 20 example neurons during dangled presentation of male or female intruders. **d**, Average Z-scores of mean responses during 5 stimulus presentations. **e**, Spatial map of female- and male-preferring units from 1 representative mouse. **f**, Raster plots showing mean responses from all recorded units relative to sniff onset, during repeated dangling presentations of male, female or toy mice. **g**, Mean percentages of male- or female-preferring or co-active units (calculated by choice probability; see Methods). **h**, Mean percentage of male- or female-preferring units per imaged animal. **i**, Performance of time-evolving SVM decoders (Methods) of intruder sex trained on responses to dangled male or female intruders, tested on held-out data. **j**, Raster plot of BNSTpr neuronal activity during male-male or male-female unrestrained social interactions. For comparative purposes, all frames containing each behavior scored (indicated below plot) during a 30 minute social interaction were concatenated and binned into 10s intervals; Averaged z-scored responses of each unit across all bins are shown. **k**, Venn diagram of units that are activated ( $>2\sigma$  over pre-intruder baseline) during different phases of male-male / male-female interactions. Color code as in (j). **l**, Venn diagram of units that are male- or female-preferring (determined by choice probability) during dangled presentations of, or free interactions with, intruders. Color scheme to *right*. **m**, Binary choice probability histograms and percentages of tuned units comparing: sniffing male vs female; attack vs sniff male; and mount vs sniff female. **n**, Population activity vectors in the first two principal components space during male- and female-directed behaviors, from 1 example mouse. **o**, Variance ( $R^2$ ) in population activity that can be explained by intruder sex or by male- or female-directed consummatory behavior. Statistics: two-sided Wilcoxon signed-rank test (**h**). two-sided Kolmogorov-Smirnov test (**i**). Values are plotted as mean  $\pm$  SEM. \*\*\*\* $p < 0.0001$ ; \*\*\* $p < 0.001$ ; \*\* $p < 0.01$ ; \* $p < 0.05$ . n=15 mice.

Figure 3

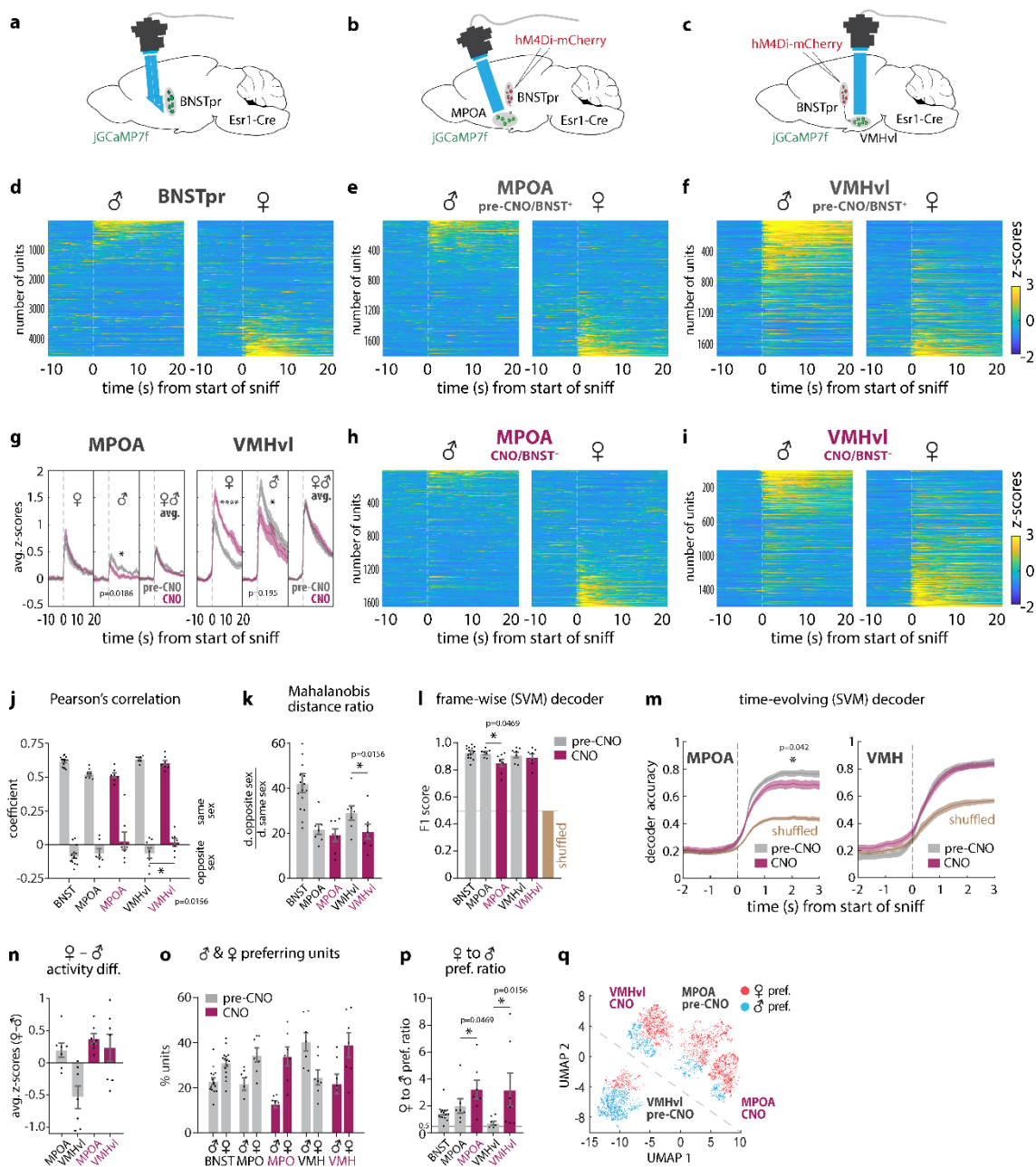
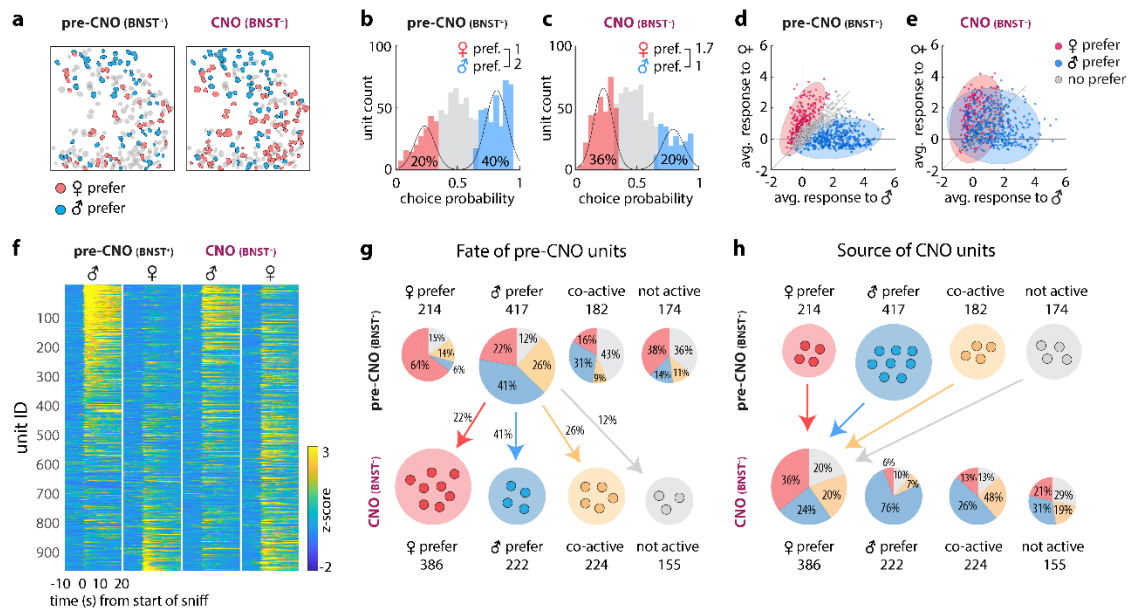


**Figure 3: BNSTpr is required for male-biased intruder sex representations in VMHvl.**

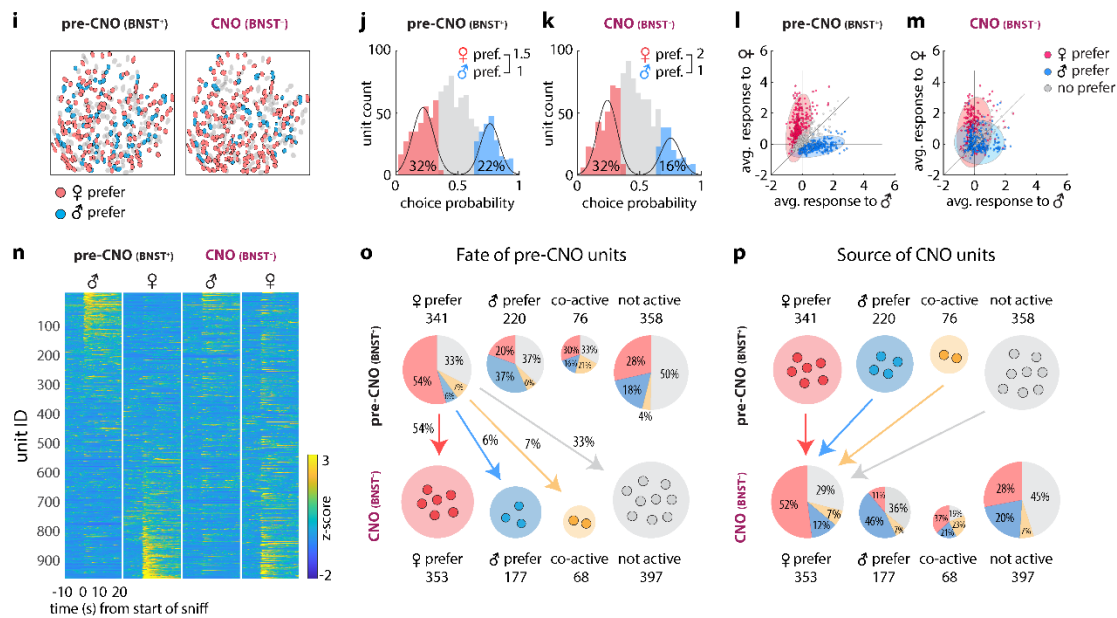
**a**, Illustration of BNSTpr miniscope imaging. **b, c**, Illustration of ChemoScope imaging in MPOA (**b**) and VMHvl (**c**) while silencing BNSTpr. **d, e, f, h, i** Average single-unit responses imaged during 5 repeated dangling presentations of male or female mice in BNSTpr (**d**), pre-CNO MPOA (**e**), and pre-CNO VMHvl (**f**), or CNO-treated (7.5mg/kg CNO i.p.) MPOA (**h**), and VMHvl (**i**), “Pre-CNO” animals received an equivalent volume of saline i.p. CNO controls shown in **ED Fig. 11, m**. **g**, Average bulk (down-sampled) calcium responses to dangled female or male stimuli, or combined male and female responses, before (i.e., saline-injected) vs. after the application of CNO, in MPOA (**left panel**) or VMHvl (**right panel**). **j**, Average Pearson’s correlation coefficient and **k**, average Mahalanobis distance ratio between population responses to dangled mice of the same or opposite sex in BNSTpr, MPOA and VMHvl,  $\pm$ CNO. **l, m** Performance of frame-wise (**l**) or time-evolving (**m**) decoders. **n**, Average difference between responses to female or male stimuli in MPOA and VMHvl. **o**, Average percentage of male- vs female-preferring units. **p**, Ratio of female to male-preferring units. **q**, supervised UMAP embedding of population responses to male and female stimuli across MPOA and VMHvl (see Methods). Statistics: two-sided Kolmogorov-Smirnov test (**g, m**). two-sided Wilcoxon signed-rank test (**j, k, l, p**). Values are plotted as mean  $\pm$  SEM. \*\*\*\* $p < 0.0001$ ; \*\*\* $p < 0.001$ ; \*\* $p < 0.01$ ; \* $p < 0.05$ .  $n=7$  mice per imaged region.

Figure 4

## VMHvl



## MPOA

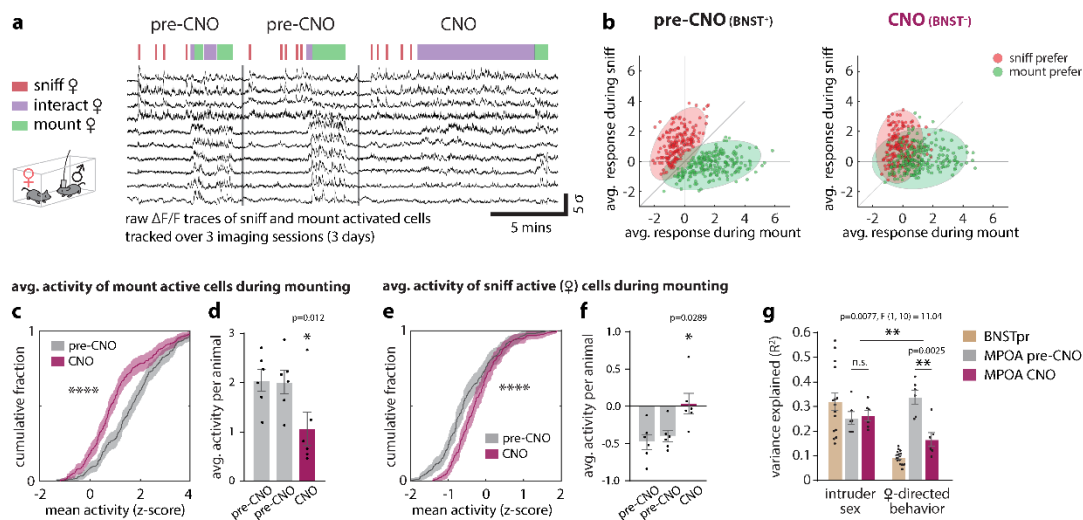


**Figure 4: Differential effect of BNSTpr silencing on sex representations in VMHvl and MPOA revealed by sequential imaging of identified units.**

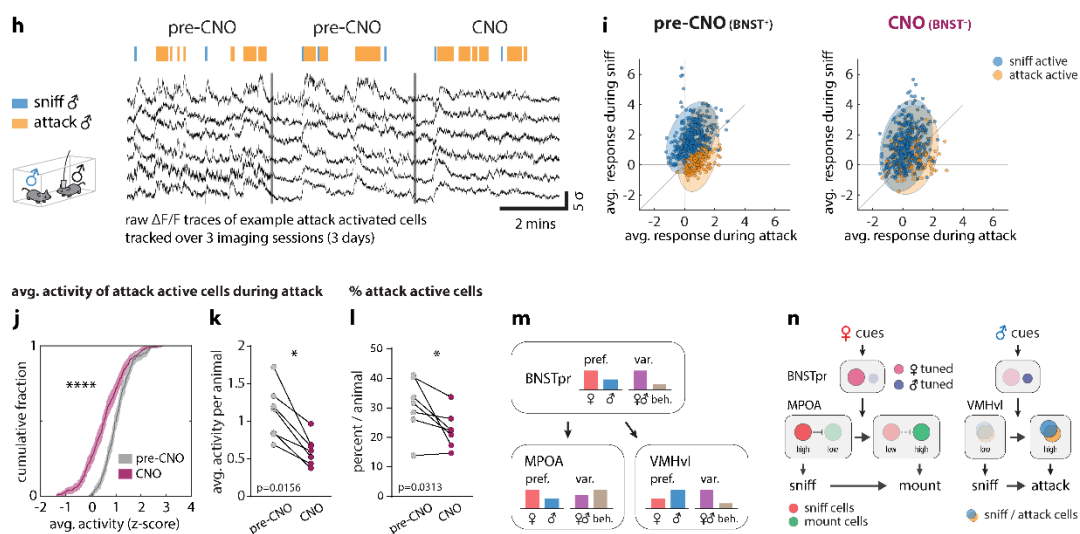
**a, i**, Spatial maps of tracked male and female-preferring units in VMHvl (**a**) and MPOA (**i**) before and after CNO application. **f, n**, Single-unit responses to dangled male or female stimuli in VMHvl (**f**) or MPOA (**n**) before vs. after CNO application. Sorting of units is the same pre- vs. post-CNO. **b, c, j, k**, Histograms of male- vs. female-tuned units determined by choice probability from single-unit responses to dangled intruders. **d, e, l, m**, Scatter plots of single-unit responses to dangled male and female mice before and after CNO application in VMHvl (**d, e**) or MPOA (**l, m**). Each dot (**d, e, l, m**) represents a single neuron and the color of each dot indicate its male / female preference *before* CNO application. Distribution of male- or female-preferring units *before* (**d, l**) and *after* (**e, m**) CNO are shown as colored ellipses. **g, h, o, p**, Pie charts showing fates (**g, o**) and sources (**h, p**) of units in VMHvl (**g, h**) or MPOA (**o, p**) before vs. after CNO treatment, respectively. The percentage of units of each type that retained or switched sex-preference, responded to both sexes (“co-active”) or responded to neither sex (“not active”) is indicated.

Figure 5

## ChemoScope BNSTpr - MPOA

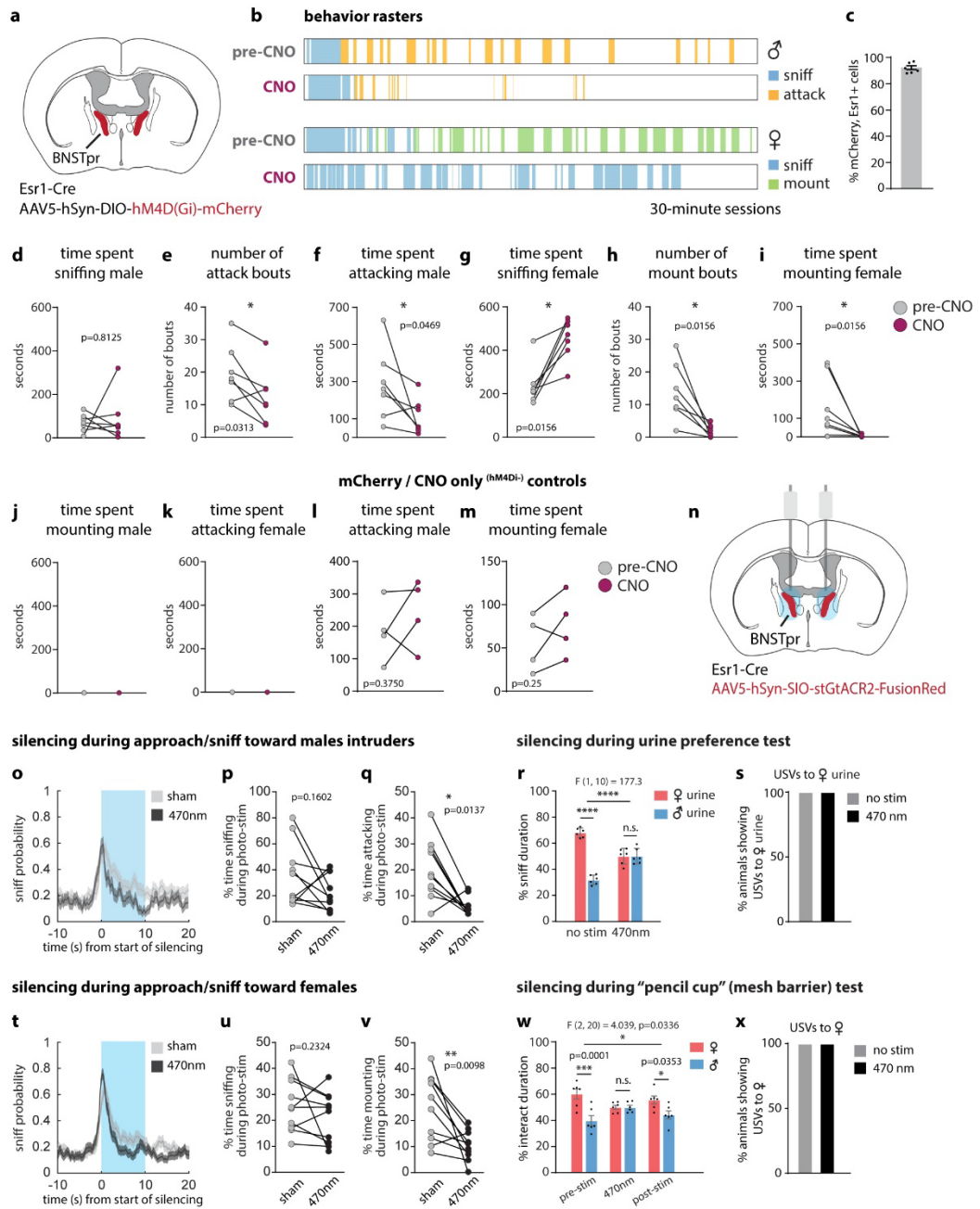


## ChemoScope BNSTpr - VMHvl



**Figure 5: Differential effect of BNSTpr silencing on behavior representations in MPOA and VMHvl revealed by unilateral ChemoScope imaging.**

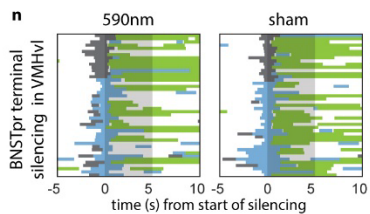
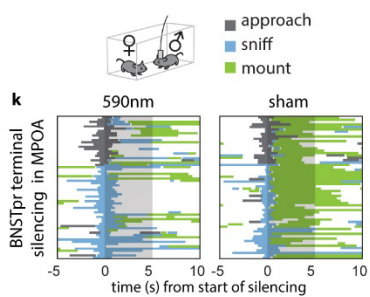
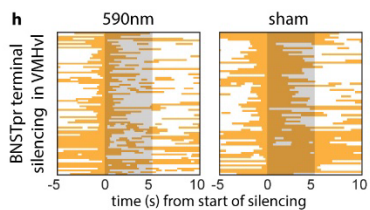
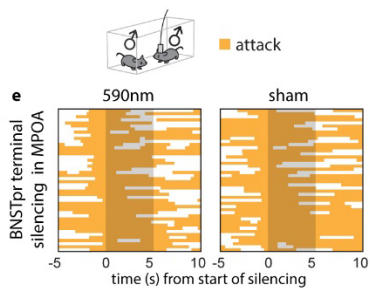
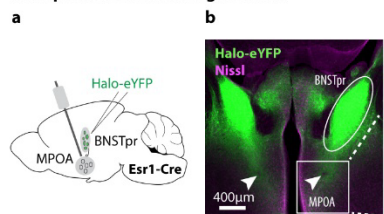
**a, h**, example  $\Delta F/F$  traces of neurons tracked over 3 imaging sessions in MPOA (**a**) and VMHvl (**h**). **b, i**, Scatter plot of single-unit responses to sniff and mount females in MPOA (**b**), or to sniff and attack males in VMHvl (**i**) before and after CNO application. Each dot (**b, i**) represents a single neuron and the color of each dot in both plots indicates its tuning *before* CNO application. Distribution of sniff vs mount MPOA units (**b**) or sniff vs attack VMHvl units (**i**) before and after CNO are shown as colored ellipses. **c-f**, Cumulative fractions (**c, e**) and bar graphs (**d, f**) of MPOA single-unit responses to initially (i.e., in saline-injected animals/pre-CNO) mount active (**c**) or sniff active (**e**) cells during mounting, before vs. after CNO. **g**, Variance ( $R^2$ ) in population activity that can be explained by intruder sex or by female-directed consummatory behavior in BNSTpr or in MPOA, before vs. after CNO. **j, k**, Cumulative fractions (**j**) and scatter plots (**k**) of VMHvl single-unit responses to initially attack-active cells during attack, before vs. after CNO. **l**, percent of attack-active cells per animal before vs. after CNO. **m**, Diagram summarizing observed transformations of sex and behavior representations from BNSTpr to MPOA and VMHvl. “Pref.,” fraction of units that are either female (red bars)- or male (blue bars)-preferring neurons. “Var.,” fraction of variance explained ( $R^2$ ) by intruder sex (purple bars) or consummatory behavior (light brown bars). **n**, Schematic illustrating the role of BNSTpr<sup>Esr1</sup> neurons in promoting the transition from sniffing to mounting or attack, inferred from the circuit-level and behavioral phenotypes of BNSTpr silencing. Pale circles, low activity; saturated circles; high activity. Vertical arrows indicate net functional effects, not circuitry. Horizontal arrows indicate time-dependent transitions. Statistics: two-sided Kolmogorov-Smirnov test (**c, e, j**), two-sided Wilcoxon signed-rank test (**k, l**), Friedman test with Dunn’s correction (**d, f**), two-way ANOVA with Bonferroni correction for variance explained in MPOA pre-CNO and CNO (**g**), variance explained in BNSTpr was plotted for reference and was **not** used in the two-way ANOVA. \*\*\*\* $p < 0.0001$ ; \*\*\* $p < 0.001$ ; \*\* $p < 0.01$ ; \* $p < 0.05$ . Values are plotted as mean  $\pm$  SEM. For ChemoScope BNSTpr-MPOA,  $n=6$  mice (**d, f, g**). For ChemoScope BNSTpr-VMHvl  $n=7$  mice (**k, l**).



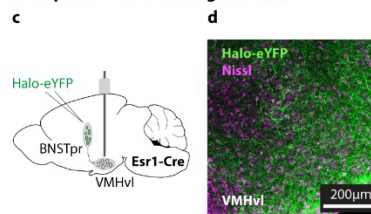
**Extended Data Figure 1: Chemogenetic and optogenetic silencing of BNSTpr<sup>Esr1</sup> neurons disrupts aggression and mating.**

**a**, Illustration of hM4d (Gi)-mediated silencing in bilateral BNSTpr<sup>Esr1</sup> neurons. **b**, Example behavior raster plot from 1 animal across 4 recording sessions. **c**, Percent of BNSTpr<sup>Esr1</sup> neurons that express mCherry. Values are plotted as mean  $\pm$  SEM, n=6 mice. **d-m**, Measurements performed before (pre-CNO: saline injection, gray points) vs. after (CNO injection, maroon points) chemogenetic silencing of BNSTpr, of time spent sniffing male intruders (**d**), number of attack bouts toward male intruders (**e**), time spent attacking male intruders (**f**), time spent sniffing female intruders (**g**), number of mount bouts toward female intruders (**h**), time spent mounting female intruders (**i**), time spent mounting male intruders (**j**), time spent attacking female (**k**), and time spent attacking male (**l**), time spent mounting female (**m**) in mCherry/CNO only controls (**l, m**) per 30-minute session. 100 $\mu$ l containing either saline (pre-CNO) or 7.5mg/kg CNO was given i.p. 60 minutes prior to start of behavior tests. **n**, Illustration of bilateral optogenetic silencing in BNSTpr. **o, t**, Mean probability of sniff behavior occurring relative to onset of optogenetic silencing. **p, u**, Duration of sniffing toward male (**p**) or female (**u**) intruders. **q, v**, Duration of attack (**q**) toward male intruders or mount (**v**) toward female intruders as a percentage of the duration of optogenetic silencing. “Sham” controls were the same animals during a 10s “sham stimulation,” i.e., without light. **r, w**, Percent of time spent interacting with male or female urine (**r**), or male or female conspecifics separated by a meshed barrier (**w**) before and during (**r**) or before, during and after (**w**) optogenetic silencing of BNSTpr. Optogenetic silencing conditions: 470nm @  $\sim$ 1 mW/mm<sup>2</sup> for 10 seconds (**o, p, q, t, u, v**). 470nm @  $\sim$ 1 mW/mm<sup>2</sup> for 10 minutes (**r, s, w, x**) Statistics: For Chemogenetic inhibition, two-sided Wilcoxon signed-rank test (**d-m**). Values are plotted as total time or total bouts per 30-minute session per animal. n = 7 mice (**d-k**), n=4 mice (**l, m**). For Optogenetic inhibition during interactions with male or female conspecifics (**o, p, q, t, u, v**), two-sided Kolmogorov-Smirnov test (**o, t**), two-sided Wilcoxon signed-rank test (**p, q, u, v**). Male-male trials (**o, p, q**), n=131 stim and 125 sham trials pooled from 10 mice. Male-female trials mice (**t, u, v**), n=181 stim and 170 sham trials pooled from 10 mice. For Optogenetic inhibition during urine preference (**r**) and “pencil cup” (mesh barrier) (**w**) tests, two-way ANOVA with Bonferroni correction, n=6 mice. Values are plotted as mean  $\pm$  SEM. \*\*\*\*p < 0.0001; \*\*\*p < 0.001; \*\*p < 0.01; \*p < 0.05.

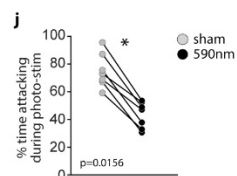
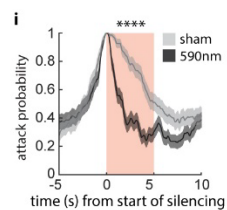
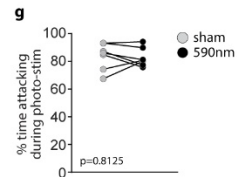
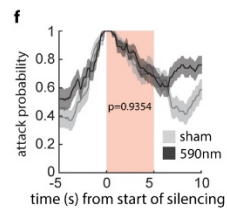
## BNSTpr terminal silencing in MPOA



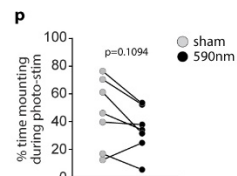
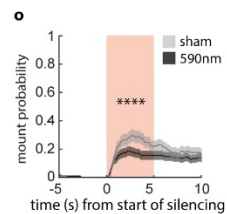
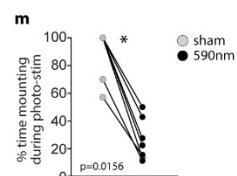
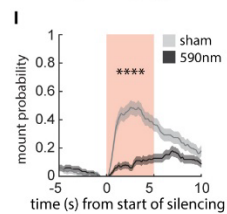
## BNSTpr terminal silencing in VMHvl



## silencing during attack

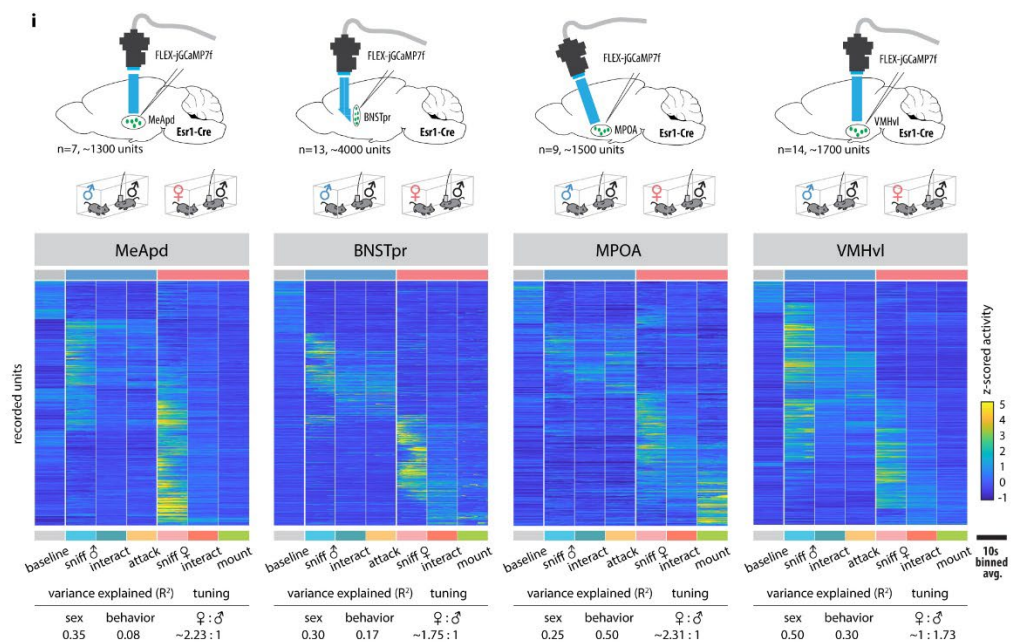
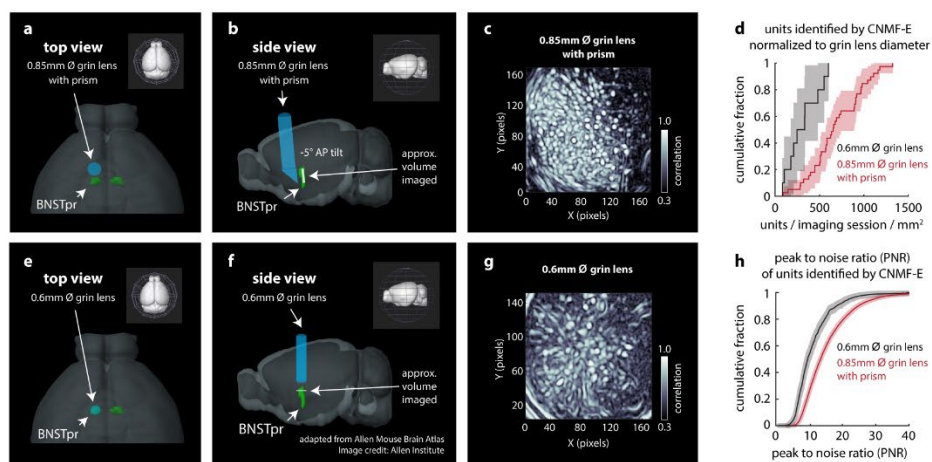


## silencing during approach/sniff toward female intruder



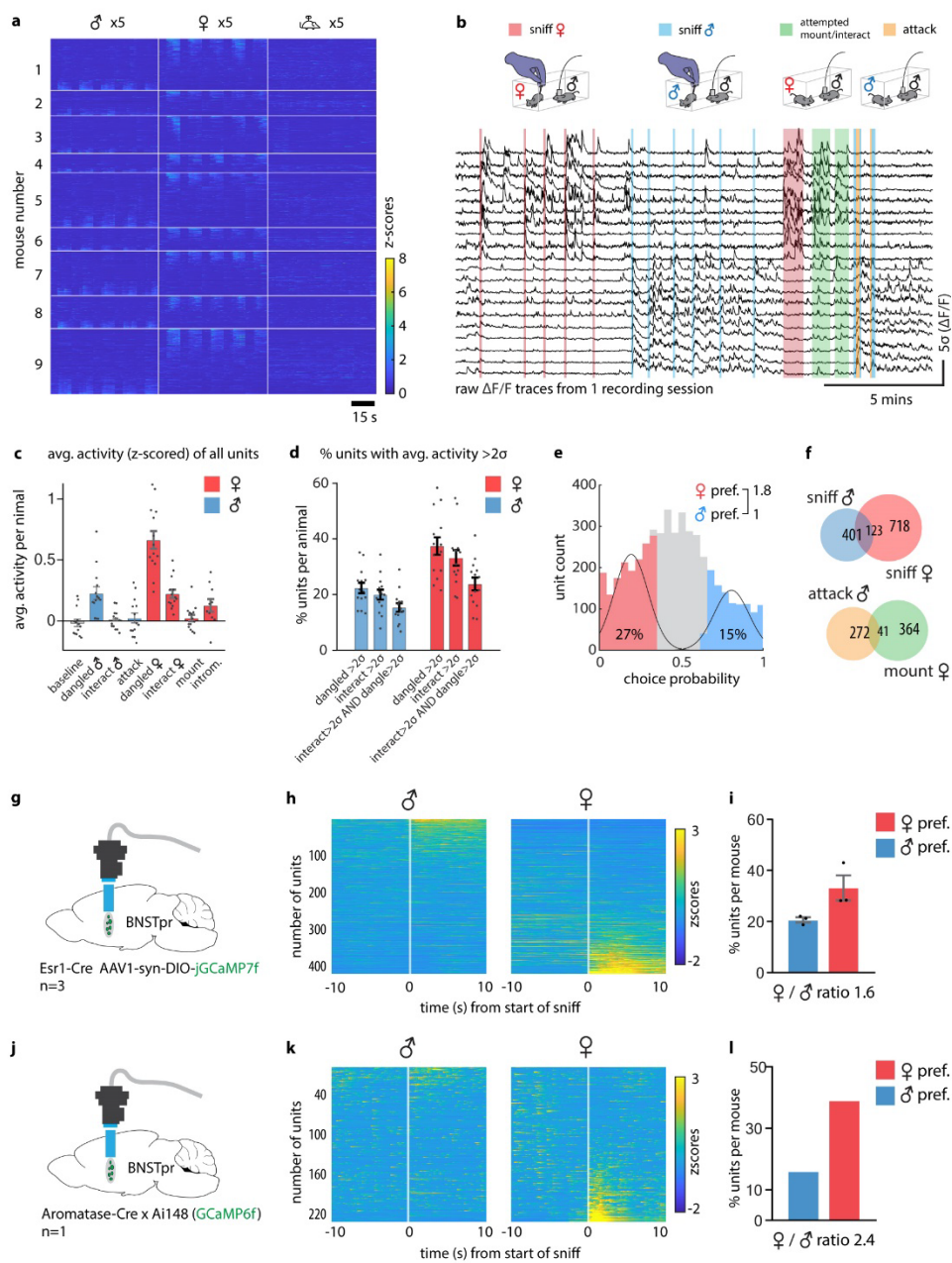
**Extended Data Figure 2: Optogenetic silencing of BNSTpr<sup>Esr1</sup> terminals in MPOA or VMHvl during male-male/ male-female interactions.**

**a, c**, Diagram illustrating BNST terminal silencing in MPOA (**a**) or VMHvl (**c**). **b, d**, Representative images showing Halo-EYFP cell body expression in BNSTpr and axonal expression in MPOA (**b**) and VMHvl (**d**). Similar expression patterns were observed in all 14 animals tested (**b, d**). **e, h, k, n**, Raster plots showing distribution of social behaviors relative to optogenetic silencing of BNSTpr terminal in MPOA (**e, k**) or VMHvl (**h, n**). **f, i, l, o**, Average probability of behavior occurring relative to onset of optogenetic silencing. **g, j, m, p**, Duration of attack (**g, j**) or mount (**m, p**) as a percentage of the 5-second optogenetic silencing. Statistics: two-sided Kolmogorov-Smirnov test (**f, i, l, o**), values are plotted as mean  $\pm$  SEM. Two-sided Wilcoxon signed-rank test (**g, j, m, p**). \*\*\*\* $p < 0.0001$ ; \*\*\* $p < 0.001$ ; \*\* $p < 0.01$ ; \* $p < 0.05$ .  $n=7$  mice for each silenced region.



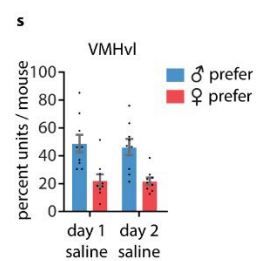
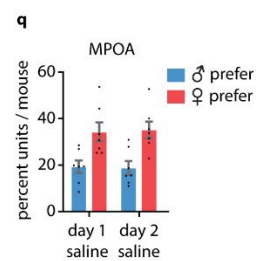
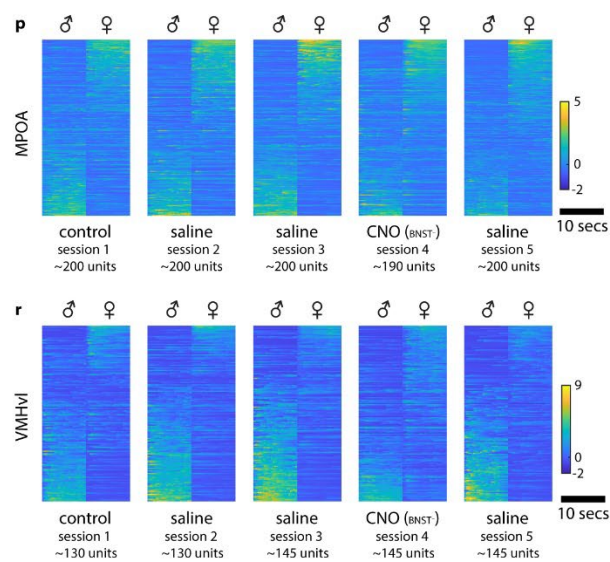
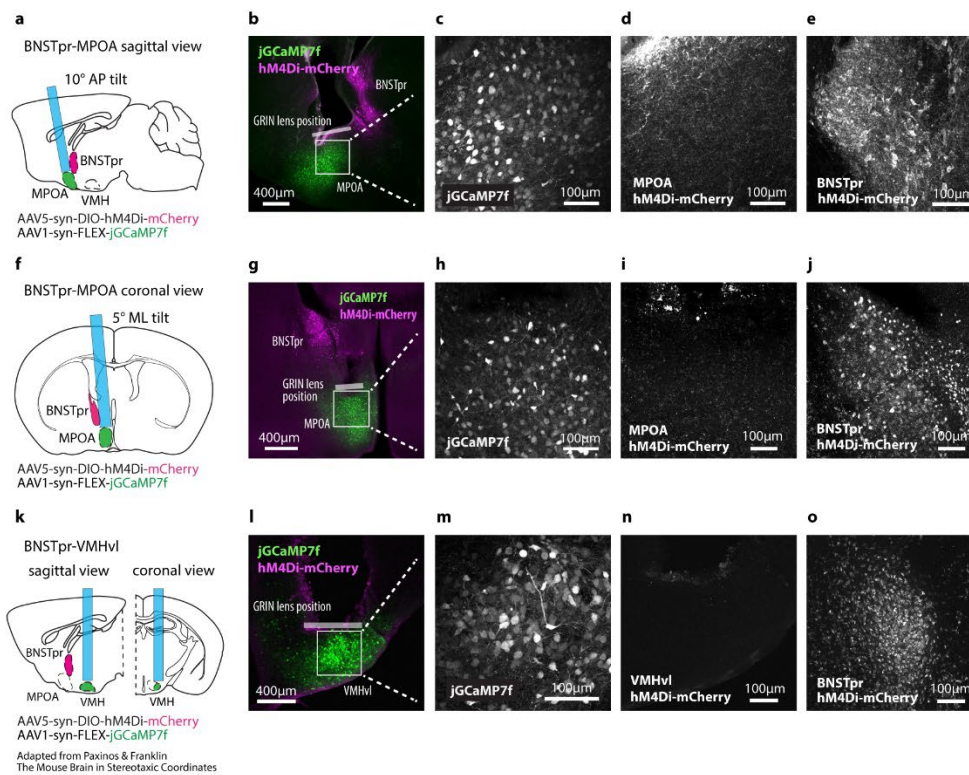
**Extended Data Figure 3: Performance of 0.85 mm Ø prism coupled GRIN lens compared to 0.6 mm Ø GRIN lens for imaging BNSTpr.**

**a, b, d, e**, Illustrations showing GRIN lens placement in BNSTpr from top (**a, d**) and side (**b, e**) views. **a-c**, Illustrations or data from animals implanted with prism lenses. **d-f**, Data from animals implanted with conventional cylindrical GRIN lenses. **c, f**, Mean pixel correlation during 1 example imaging session. **g**, Cumulative fraction of number of units captured per imaging session normalized to the diameter of the GRIN lens. **h**, Cumulative fraction of the peak to noise ratio (PNR) of all units imaged using either a 0.6mm grin lens or a 0.85mm prism-coupled grin lens. **i**, Raster plots of MeApd, BNSTpr, MPOA and VMHvl  $Esr1^+$  neuronal activity during male-male or male-female unrestrained social interactions. For comparative purposes, all frames containing each behavior scored (indicated below plot) during a 30 minute social interaction were concatenated and binned into 10s intervals; Averaged z-scored responses of each unit across all bins are shown. Tables below show the average variance ( $R^2$ ) in population activity that can be explained by intruder sex or by male and female-directed consummatory behavior and the ratio of female-preferring to male-preferring neurons in each imaged region.



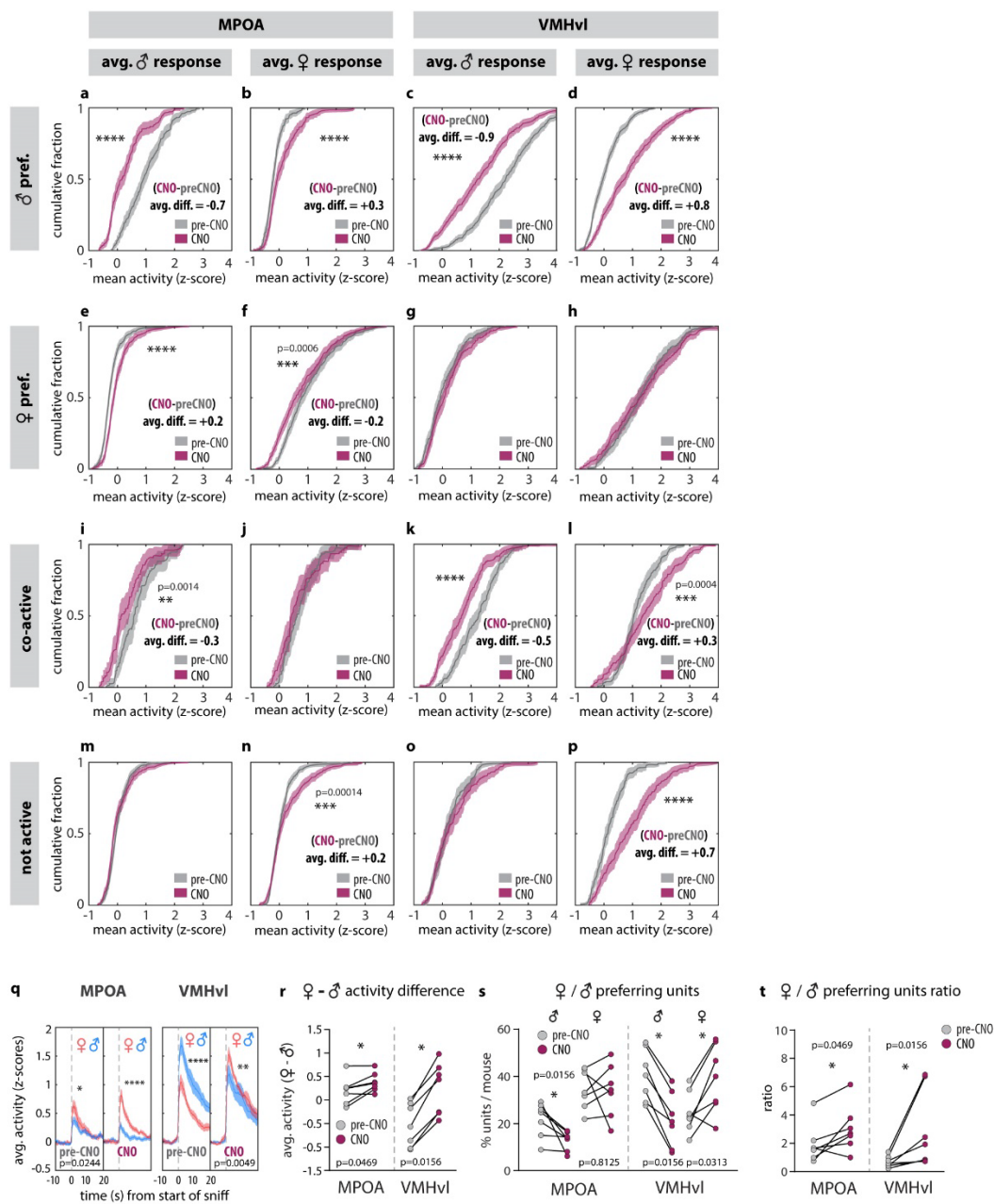
#### Extended Data Figure 4: Miniscope imaging analysis of BNSTpr neurons.

**a**, Example raster plot of population responses to 5 repeated presentations of dangled male, female or toy intruders from a cohort of 9 individual animals (cohort 1, n = 6, cohort 2, n = 9). **b**, continuously recorded raw  $\Delta F/F$  traces of 20 example neurons from 1 recording session. **c**, Average z-scored responses of BNSTpr neurons per animal (n=15 mice) during 8 annotated behaviors/conditions. **d**, Percent of units per animal (n=15 mice) whose average response is  $>2\sigma$  baseline measured prior to intruder introduction. **e**, Histograms of male- / female-preferring units determined by choice probability from single-unit responses to dangled intruders. **f**, Venn diagram of units that are male- or female- sniff preferring (top), or attack- or mount- preferring (bottom) (determined by choice probability) during free interactions with, or sniffing of dangled, male or female intruders. **g-l**, Comparison of BNSTpr<sup>Esr1</sup> (**g, h, i**) and BNSTpr<sup>AB</sup> (**j, k, l**) population responses to dangled presentation of male or female intruders. **g, j**, Illustration of BNSTpr<sup>Esr1</sup> (**g**) and BNSTpr<sup>AB</sup> (**j**) miniscope imaging using a conventional 0.6mm GRIN lens. **h, k**, Average z-scores of single-unit responses relative to the start of sniff during 5 repeated dangling presentations of male or female intruders. **i, l**, percent of male vs female preferring units in BNSTpr. n=15 mice.



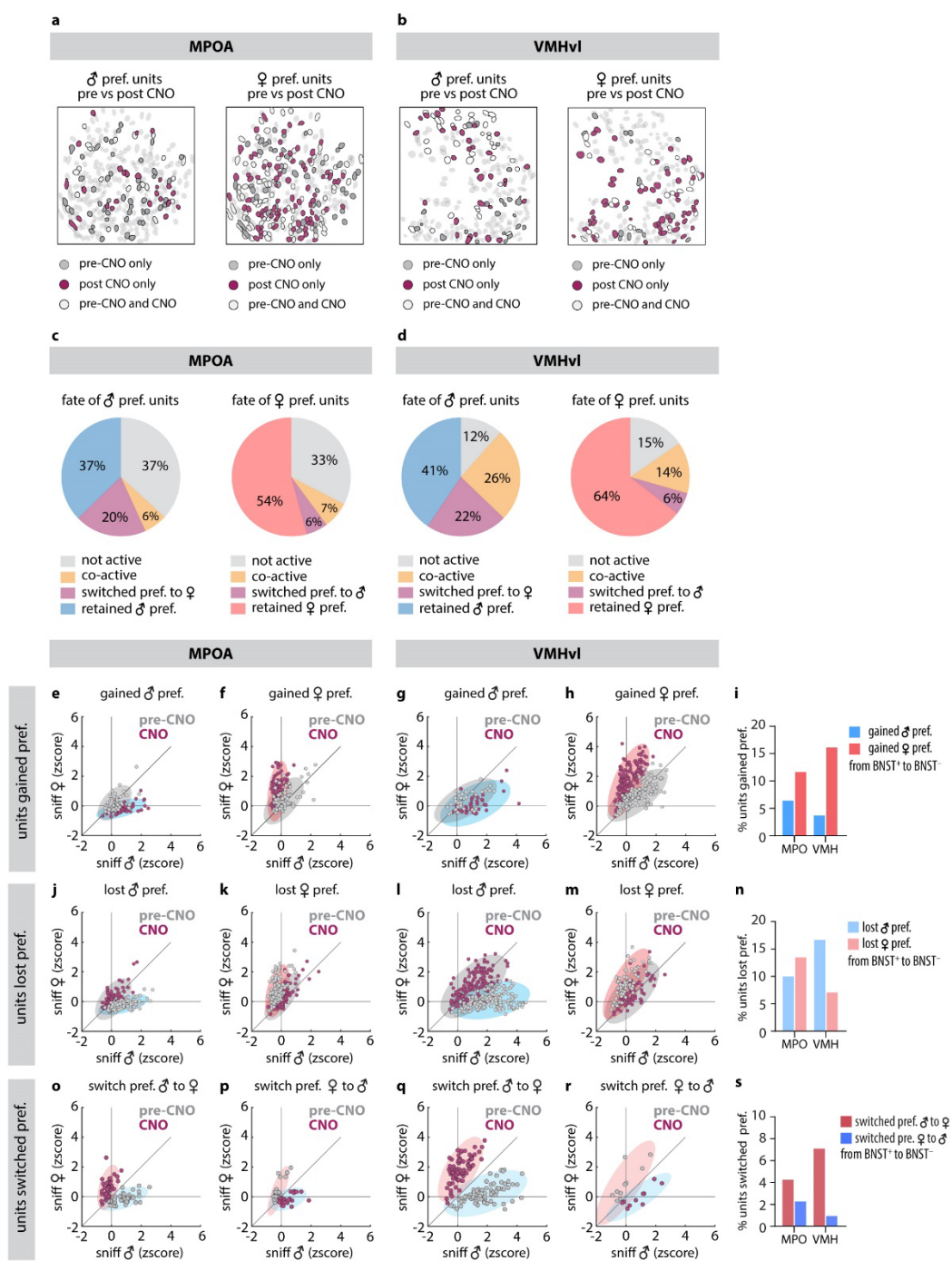
**Extended Data Figure 5: ChemoScope imaging of MPOA and VMHvl across multiple days.**

**a, f, k**, Diagram showing the position of 0.6mm GRIN lens in relation to MPOA, BNSTpr and VMHvl. **b-e**, Sagittal histology sections showing the expression of jGCaMP7f in MPOA (**b, c**), hM4Di-mCherry in BNSTpr (**b, e**), and lack of cell body expression of hM4Di-mCherry in MPOA (**d**). **g-j**, Coronal histology sections showing the expression of jGCaMP7f in MPOA (**g, h**), hM4Di-mCherry in BNSTpr (**g, j**), and lack of cell body expression of hM4Di-mCherry in MPOA (**i**). **l-o**, Coronal histology sections showing the expression of jGCaMP7f VMHvl (**l, m**), hM4Di-mCherry in BNSTpr (**o**), and lack of cell body expression of hM4Di-mCherry in VMHvl (**n**). Similar expression patterns were observed in 14 mice tested (7 mice for each imaged region). **p, r**, example raster plots of average single-unit responses to 5 trials of dangled male or female intruders in MPOA (**p**) and VMHvl (**r**) across multiple imaging sessions (sessions are 2-3 days apart). Units are sorted based on their eigenvalues in the first principal component of the population activity vector. **q, s**, percent of units that are male or female preferring across 2 days of imaging in MPOA (**q**) and VMHvl (**s**), in saline-injected animals. n=7 mice from each imaged region.



**Extended Data Figure 6: ChemoScope imaging of MPOA and VMHvl.**

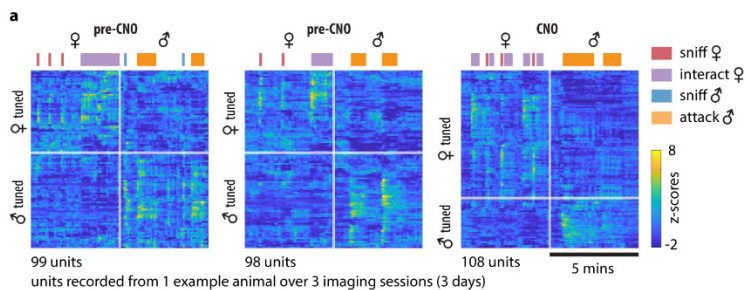
Cumulative fractions showing average single unit responses to dangled male and female intruders from initially (i.e., in saline-injected animals) male preferring (**a-d**), female preferring (**e-h**), co-active (**i-l**) and not active (**m-p**) units in MPOA (**a,b,e,f,i,j,m,n**) and VMHvl (**c,d,g,h,k,l,o,p**). **q**, average responses to dangled male or female intruders in MPOA (left panel) and VMHvl (right panel). **r-t**, mean response difference between dangled female and male intruders (**r**), percentage of male vs female preferring units (**s**) and the ratio of female- to male-preferring units (**t**) before and after the application of CNO, in MPOA or VMHvl. Statistics: Kolmogorov-Smirnov test (**a-q**). Values are plotted as mean  $\pm$  SEM. Mann-Whitney test (**r-t**). \*\*\*\* $p < 0.0001$ ; \*\* $p < 0.01$ ; \* $p < 0.05$ .  $n=7$  mice from each imaged region.



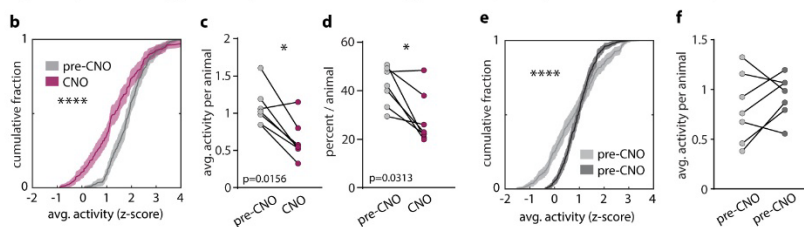
**Extended Data Figure 7: Tracking changes to MPOA and VMHvl single-unit responses before and after silencing BNSTpr.**

**a, b**, spatial maps showing distribution of male- or female preferring units before (gray) and after (maroon) chemogenetic silencing of BNSTpr in MPOA(**a**) or VMHvl (**b**). **c, d**, response profiles of initially (i.e., in saline-injected animals/pre-CNO) male- or female preferring units after BNSTpr silencing, in MPOA (**c**) and VMHvl (**d**). (**e-s**) 2d scatter plots and bar plots showing average single-unit responses to dangled male and female intruders from tracked units in MPOA and VMHvl, sorted as indicated.

### BNSTpr - VMHvl ChemoScope

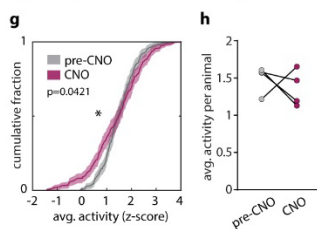


avg. activity of sniff active (♂) cells during attack % sniff active (♂) cells pre-CNO controls (BNST<sup>NM4Dfl/+</sup>/CNO)



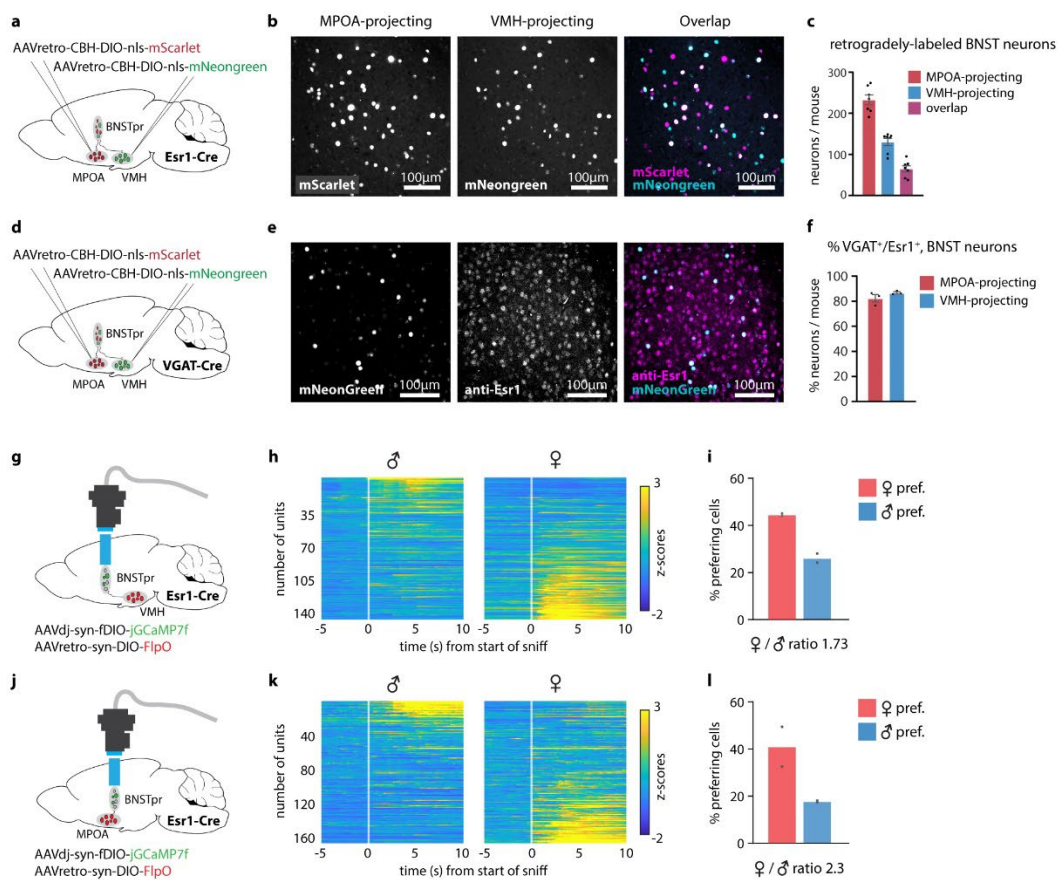
mCherry / CNO only controls (BNST<sup>NM4Dfl/+</sup>/mCherry+)

avg. activity of attack active cells during attack



**Extended Data Figure 8: Effect of BNSTpr silencing on VMHvl behavior representations and female / male preference.**

**a**, Raster plot of all recorded units from 1 example animal over 3 imaging sessions. Units are sorted separately for each recorded session based on their responses during male and female interactions. **b, c, e-h**, Cumulative fractions (**b, e, g**) and bar graphs (**c, f, h**) of VMHvl single-unit responses to initially (i.e., in saline-injected animals/pre-CNO) sniff active (**b, c**) or attack active (**e-h**) cells during attack before CNO (i.e., saline-injected/pre-CNO) (**e, f**), or before and after CNO (**b, c, g, h**). **g, h**, mCherry/CNO only controls. **d**, percent sniff active cells in VMHvl before (i.e., saline-injected/pre-CNO) and after CNO. Statistics: two-sided Kolmogorov-Smirnov test (**b, e, g**), values are plotted as mean  $\pm$  SEM, two-sided Wilcoxon signed-rank test (**c, d, f, h**). \*\*\*\* $p < 0.0001$ ; \*\*\* $p < 0.001$ ; \*\* $p < 0.01$ ; \* $p < 0.05$ .  $n=7$  mice.



**Extended Data Figure 9: Retrograde tracing and imaging of BNSTpr projection neurons.**

**a, d**, Diagram showing retrograde tracing of BNSTpr projection neurons. **b, e**, Example images showing MPOA or VMHvl projecting neurons expressing mScarlet or mNeongreen. **c**, Average number of back-labeled BNSTpr neurons per animal.  $n = 7$  animals. **f**, percent of VGAT+ projection neurons that are Esr1+. **g, j**, Diagram showing miniscope imaging of VMHvl- or MPOA-projecting BNSTpr neurons. **h, k**, Average z-scores of single-unit responses relative to the start of sniff during 5 repeated dangling presentations of male or female intruders. **i, l**, percent of male- or female-preferring units.

## METHODS

### Mice

All experimental procedures involving the use of live mice or their tissues were carried out in accordance with NIH guidelines and approved by the Institute Animal Care and Use Committee (IACUC) and the Institute Biosafety Committee (IBC) at the California Institute of Technology

(Caltech). All C57BL/6N mice used in this study, including wild-type and transgenic mice, were bred at Caltech. BALB/c male and female mice were used as intruder mice and bred at Caltech or purchased from Charles River Laboratories (CRL). Experimental mice were used at the age of 2–3 months. Intruder mice were used at the age of 2–6 months and were maintained with three to five cage mates to reduce their aggression. *Esr1*<sup>Cre/+</sup> knock-in mice (Jackson Laboratory stock no. 017911) were backcrossed into the C57BL/6N background (>N10) and bred at Caltech. Heterozygous *Esr1*<sup>Cre/+</sup>, or double heterozygous *Aromatase*<sup>Cre/+</sup> (ref. 17); *Ail48/+*<sup>43</sup> mice were used for cell-specific targeting experiments and were genotyped by PCR analysis using genomic DNA from tail or ear tissue. All mice were housed in ventilated micro-isolator cages in a temperature-controlled environment (median temperature 23 °C, humidity 60%), under a reversed 11-h dark–13-h light cycle, with ad libitum access to food and water. Mouse cages were changed weekly.

### Virus

The following AAVs along with the supplier, injection titres in viral genome copies/ml (vg/ml) and injection volumes in nanoliters (nl) were used in this study.

AAV1-hSyn1-SIO-stGtACR2-FusionRed (Addgene 105677,  $\sim 2 \times 10^{12}$  vg/ml, 200nl), AAV5-hSyn-DIO-hM4D(Gi)-mCherry (Addgene 44362,  $\sim 2 \times 10^{12}$  vg/ml, 200nl per injection), AAV5-Ef1a-DIO-eNpHR3.0-eYFP (Halo-eYFP, **E.D. Fig. 2**) (Addgene 26966,  $\sim 4 \times 10^{12}$  vg/ml, 200nl per injection), AAV1-syn-FLEX-jGCaMP7f-WPRE (Addgene 104492,  $\sim 2 \times 10^{12}$  vg/ml, 200nl per injection), AAVdj-syn-FLEX-FlpO (Janelia Vector Core,  $\sim 1 \times 10^{13}$  vg/ml, 200nl per injection), AAVretro-syn-fDIO-jGCaMP7f (Janelia Vector Core,  $\sim 2 \times 10^{12}$  vg/ml, 200nl per injection), AAVretro-CBH-DIO-nls-mScarlet (Janelia Vector

Core,  $\sim 1 \times 10^{13}$  vg/ml, 200nl per injection), AAVretro-CBH-DIO-nls-mNeonGreen (Janelia Vector Core,  $\sim 1 \times 10^{13}$  vg/ml, 200nl per injection).

### **Stereotaxic Coordinates for virus injection and GRIN lens implantation**

Stereotaxic injection coordinates were based on the Paxinos and Franklin atlas<sup>44</sup>.

Virus injection: BNSTpr, AP: -0.15, ML:  $\pm 0.65$ , DV: -3.75, VMHvl, AP: -1.5, ML:  $\pm 0.75$ , DV: -5.75, MPOA, AP: 1.0, ML:  $\pm 0.3$ , DV: -4.75, MeApd, AP: -1.65, ML:  $\pm 2.1$ , DV: -4.9).

Gradient Refractive Index (GRIN) lens implantation:

BNSTpr: AP: -0.1, ML: -0.7, DV: -4.5 ( $\emptyset 0.85 \times 7$ mm GRIN lens with prism, **Extended Data Fig. 3**).

BNSTpr: AP: -0.2, ML: -0.7, DV: -3.65 ( $\emptyset 0.6 \times 7.3$ mm GRIN lens).

MeApd: AP: -1.65, ML: -2.0, DV: -4.75 ( $\emptyset 0.6 \times 7.3$ mm GRIN lens).

VMHvl: AP: -1.6, ML: -0.75, DV: -5.6 ( $\emptyset 0.6 \times 7.3$ mm GRIN lens).

MPOA: AP: +1.0, ML: -1.0, DV: -5.0 ( $\emptyset 0.6 \times 7.3$ mm GRIN lens). Implanted at a  $10^\circ$  tilt in AP axis and a  $5^\circ$  tilt in ML axis to avoid damaging BNSTpr and its projections to MPOA (**Extended Data Fig. 5a-j**).

### **Surgeries**

Surgeries were performed on socially and sexually experienced adult male *Esr1<sup>Cre/+</sup>* mice, aged 2-3 months. Virus injection and implantation were performed as described previously<sup>9,19</sup>. Briefly, animals were anaesthetized with isoflurane (5% for induction and 1.5% for maintenance) and placed on a stereotaxic frame (David Kopf Instruments). Virus was injected into the target area using a pulled glass capillary (World Precision Instruments) and a pressure injector (Micro4 controller, World Precision Instruments), at a flow rate of 50 nl/minute. The glass capillary was left in place for 5 minutes following injections before withdrawing. For microendoscope experiments, virus injection and lens implantation were performed two weeks apart. Lenses were slowly lowered into the brain and fixed to the skull with dental cement (Metabond, Parkell). 2 weeks after lens implantation, mice were head-fixed on a running wheel and a miniaturized microendoscope (nVista, Inscopix) was lowered over the implanted lens until GCaMP-expressing fluorescent neurons were in focus. Once GCaMP-expressing neurons were detected, a permanent baseplate was attached to the skull

with dental cement. Mice were habituated with weight-matched dummy microendoscopes (Inscopix) for at least 1 week before behavior testing.

### **Housing conditions for social and sexual experience**

All male C57BL/6N mice used in this study were socially and sexually experienced. Mice aged 8-12 weeks were initially co-housed with a female BALB/c for 1 week and were screened for sex-appropriate social behaviors. Mice that show both mounting toward females and attack toward males during a 30-minute resident intruder assay were selected for surgery and subsequent behavior experiments. From this point forward, these male mice were always cohoused with non-pregnant female BALB/c mice.

### **Chemogenetic inhibition**

Behavioral tests were performed on two consecutive days. The number of mice receiving saline or Clozapine-N-oxide (CNO) (Enzo Life Sciences) was counterbalanced across the two days. CNO was dissolved in saline. CNO (7.5mg/kg) or saline (control) was intraperitoneally injected 60 minutes prior to behavioral tests.

### **Optogenetic inhibition**

Animals were connected to a 470nm or a 590nm laser (Changchun New Industries Optoelectronics Tech Co., Ltd.) via optical patch cords ( $\varnothing 200 \mu\text{m}$ , N.A., 0.22, Doric lenses and Thorlabs) and a rotary joint (Doric lenses). The experimenter monitored mouse behavior via a computer monitor in a room adjacent to the behavioral arena. Laser was triggered manually when animals were engaged in the behaviors of interest. Sham stimulation (laser OFF) was interleaved with the light stimulation (laser ON) as an internal control. For optogenetic inhibition of BNSTpr using *gtACR2*, 10 seconds of 470nm continuous photo stimulation at  $1\text{mW}/\text{mm}^2$  at the tissue level was used during social interactions. 10 minutes of 470nm continuous photo stimulation at  $1\text{mW}/\text{mm}^2$  at the tissue level was used for urine preference and “pencil-cup” (meshed barrier) tests. For optogenetic inhibition of BNSTpr – MPOA and BNSTpr – VMHvl terminals using Halorhodopsin, 5 seconds of 590nm continuous photo stimulation at  $3\text{mW}/\text{mm}^2$  at the tissue level was used.

### **Behavior annotations**

Behavior videos were manually annotated using a custom MATLAB-based behavior annotation interface<sup>11,45</sup>. A “baseline” period of 5 minutes where the animal was alone in his home cage was recorded at the start of every recording session. A total of 7 behaviors during the resident intruder assays were annotated: sniff (face, body, genital-directed sniffing) toward male or female intruders, attack, mount, intromission, “interact” (periods where the animals were close to each other but sniff, attack, mount/intromission were absent) with male or female intruders. For “dangled” presentations of male or female intruders, the dangled bout starts at the onset of nostril/whiskers movement when the ano-genital region of the dangled intruder is held next to the resident.

### **Microendoscopic imaging**

On the day of imaging, mice were habituated for at least 10 minutes after installation of the miniscope in their home cage prior to the start of the behavior tests. Imaging data was acquired at 30 Hz with 2x spatial down-sampling, LED power (0.1-0.5) and gain (1x-7x) were adjusted depending on the brightness of GCaMP expression determined by the image histogram as per the user manual. A TTL pulse from the Sync port of the data acquisition box (DAQ, Inscopix) was used to synchronously trigger StreamPix7 (Norpix) for video recording. Imaging sessions typically lasted 1 hour (20-25 minutes of interactions per sex.)

### **ChemoScope imaging**

To minimize population activity changes associated with stress from i.p. injections, social experience or fatigue from resident intruder assays in saline or CNO trials, a series of habituation imaging sessions were performed every 2-3 days (3-4 sessions total) prior to the saline vs CNO trials used for analysis (**Extended Data Fig. 5p-s**). Mice were injected with 100 $\mu$ l of saline (or 100 $\mu$ l of 7.5mg/kg CNO for CNO trials) and returned to their home cage for 60 minutes prior to imaging.

### **Microendoscopic data extraction**

#### Preprocessing

Miniscope data were acquired using the Inscopix Data Acquisition Software as 2x down-sampled .isxd files. Preprocessing and motion correction was performed using the Inscopix Data Processing Software. Briefly, raw imaging data was cropped, 2x down-sampled, median filtered and motion corrected. A spatial band-pass filter was then applied to remove out of focus background. The filtered imaging data was temporal down-sampled to 10Hz and exported as a .tiff image stack.

#### Calcium data extraction

After preprocessing, calcium traces were extracted and deconvolved using the CNMF-E large data pipeline<sup>32</sup> with the following parameters: patch\_dims = [42, 42], gSig = 3, gSiz = 13, ring\_radius = 19, min\_corr = 0.8, min\_pnr = 8, deconvolution: foopsi with the ar1 model<sup>46</sup>. The spatial and temporal components of every extracted unit were carefully inspected manually (SNR, PNR, size, motion artifacts, decay kinetics, etc.) and outliers (obvious deviations from the normal distribution) were discarded. The extracted traces were then Z-scored prior to analysis.

#### **Choice probability**

Choice probability (CP) is a metric that estimates how well either of two different behaviors can be predicted/distinguished, based on the activity of any given neuron during these two behaviors<sup>47</sup>. CP of single neurons were computed using previously described methods<sup>9,19</sup>. To compute the CP of a single neuron for any behavior pair, 1-second binned neuronal responses occurring during each of the two behaviors were used to generate a “receiver operating characteristic” (ROC) curve. CP is defined as the area under the curve (AUC) bounded between 0 to 1. A CP of 0.5 indicates the activity of the neuron cannot distinguish between the two alternative behaviors. We defined a neuron as being capable of distinguishing between two behaviors (e.g. interacting with male vs. female) if the CP of that neuron was  $> 0.65$  or  $< 0.35$ , and was  $> 2\sigma$  or  $< -2\sigma$  of the CP computed using shuffled data (repeated 100 times). For instance, if the CP of a particular neuron for females was 0.8, and the shuffled CP was  $0.5 \pm 0.1$  (SD), that neuron would be considered as “female-preferring”. If another neuron had a CP of 0.1 and a shuffled CP of  $0.5 \pm 0.15$  (SD), that neuron would be considered as a “male-preferring” neuron.

### **Decoding intruder sex**

We constructed “frame-wise” (using 1-second binned behavior and calcium activity “frames”, **Fig. 3l**) or “time-evolving” (as a function of time at 10Hz, **Fig. 2i and Fig. 3m**) linear SVM decoders (as described previously<sup>9</sup>) to distinguish intruder sex using 50 randomly selected neurons from each animal in BNST (n=15 animals), VMHvl (n=7) and MPOA (n=7). Accuracy was evaluated using a stratified 5-fold cross-validator. Decoding was repeated 100 times and the decoder performance was reported as the mean accuracy per imaged animal. For significance testing, the mean accuracy of the decoder trained on shuffled data (repeated 500 times per imaged animal) was computed to compare against the decoder accuracy trained on actual data.

### **Determining explained variance in BNSTpr population activity**

We calculated the variance of the population activity explained by intruder sex and behaviors (**Fig. 2o**) using linear regression as described previously<sup>9</sup>. To evaluate the encoding of intruder sex and behaviors by BNSTpr<sup>Esr1</sup> neurons, we regressed the activity of single neurons against the sex of the intruder (a pair of binary vectors) and against 7 annotated behaviors (7 binary vectors). The fraction of variance explained is calculated as the ratio of the cross-validated  $R^2$  (coefficient of determination) of the fit against the sex of the intruder and the cross-validated  $R^2$  of the fit against 7 different behaviors. To determine the fraction of variance explained by behaviors, we regressed the residual activity (from the fit against intruder sex) against male- or female- directed behaviors and reported the fraction of the residual variance explained, as cross-validated  $R^2$  of the fit.

### **Pearson’s correlation**

Pearson’s correlation (**Fig. 3j**) was reported as the mean pair-wise Pearson’s correlation coefficient per imaged animal computed by using the average population responses (all trials during 1 recording session) to dangled male intruders and the 1-second binned population responses to dangled male intruders (same-sex) or dangled female intruders (opposite-sex).

### **Mahalanobis distance ratio**

Mahalanobis distance ratio (**Fig. 3k**) was expressed as the ratio between the Mahalanobis distance (described previously<sup>19</sup>) of the population vector responding to dangled female intruders (opposite sex) and the Mahalanobis distance of the population vector responding to dangled male intruders (same sex).

### **Supervised UMAP embedding of single-unit responses to male and female stimuli**

The first 50 PCs of 1-second-binned single-unit responses to male and female stimuli from MPOA and VMHvl along with categorical labels indicating the origin of each unit (MPOA pre-CNO, MPOA CNO, VMHvl pre-CNO, VMHvl CNO) were used to initialize the embedding (**Fig. 3q**). The Python implementation of UMAP<sup>48</sup> (umap-learn) were used along with the following parameters:  $n\_neighbors = 15$ ,  $min\_dist = 0.4$ ,  $metric = euclidean$ .

### **Statistical analysis**

Data were processed and analyzed using Python, MATLAB, and GraphPad (GraphPad PRISM 9). All data were analyzed using two-tailed non-parametric tests except urine preference and pencil-cup (meshed barrier) tests (**Extended Data Fig. 1r, w**), and the fraction of variance explained by intruder sex or female-directed behavior (**Fig. 5g**) where two-way ANOVA with Bonferroni correction was used. Wilcoxon signed-rank test (paired, non-parametric Mann-Whitney U test) was used for binary paired samples. Friedman test with Dunn's correction was used for non-binary paired samples (**Fig. 5d, f**). Kolmogorov-Smirnov test was used for non-paired samples. Not significant (N.S.),  $P > 0.05$ ; \* $P < 0.05$ ; \*\* $P < 0.01$ ; \*\*\* $P < 0.001$ ; \*\*\*\* $P < 0.0001$ .

### **Code availability**

The custom MATLAB and Python codes used to analyze the data in this study are available upon request.

### **Data availability**

The data on which this study is based are available upon reasonable request.

*Appendix I*SINGLE-CELL PHENOTYPING WITHIN TRANSPARENT INTACT TISSUE  
THROUGH WHOLE-BODY CLEARING

Yang, B., Treweek, J.B., Kulkarni, R.P., Deverman, B.E., Chen, C., Lubeck, E., Shah, S., Cai, L., Gradinaru, V. (2014). "Single-cell phenotyping within transparent intact tissue through whole-body clearing". *Cell* 158 (4), 945-958. doi: 10.1016/j.cell.2014.07.017

**Abstract**

Understanding the structure-function relationships at cellular, circuit, and organ-wide scale requires 3D anatomical and phenotypical maps, currently unavailable for many organs across species. At the root of this knowledge gap is the absence of a method that enables whole-organ imaging. Herein we present techniques for tissue clearing in which whole organs and bodies are rendered macromolecule-permeable and optically-transparent, thereby exposing their cellular structure with intact connectivity. We describe PACT, a protocol for passive tissue clearing and immunostaining of intact organs; RIMS, a refractive index matching media for imaging thick tissue; and PARS, a method for whole-body clearing and immunolabeling. We show that in rodents PACT, RIMS, and PARS are compatible with endogenous-fluorescence, immunohistochemistry, RNA single-molecule FISH, long-term storage, and microscopy with cellular and subcellular resolution. These methods are applicable for high-resolution, high-content mapping and phenotyping of normal and pathological elements within intact organs and bodies.

## Introduction

Facile and physiologically informative optical access to intact tissues has long been a goal of biologists. As early as the 1800s, work by scientists such as Werner Spalteholz revealed the utility of rendering tissue optically transparent for anatomical and biomedical studies (Spalteholz, 1914). Although the Spalteholz technique and its variants incur damage to tissue integrity and morphology, they are still in use a century later (Steinke and Wolff, 2001), highlighting barriers to the adoption of more recent tissue-clearing methods and modern microscopy techniques. While separate tissue clearing protocols have strengths in an application-specific context, none is able to fully surmount the most common challenges: confirmed generalizability across organs other than the brain or embryo, difficulties in execution, and incompatibility with endogenous fluorescence and/or post-hoc immunohistochemistry (**Table S1**). Thus motivation to improve tissue clearing protocols is sustained around three main objectives: 1) efficient clearing of both central and peripheral organs; 2) preservation of cellular and subcellular structures of multiple organ types; and 3) compatibility with endogenous fluorescent protein expression and post-hoc detection of DNA, RNA, and proteins.

The payoffs of such a method are optical access throughout large volumes of tissues, enabling the study of cell-to-cell spatial relationships and long-range neural connectivity in the context of preserved tissue morphology (Chung and Deisseroth, 2013; Chung et al., 2013; Kim et al., 2013; Zhang et al., 2014). In conjunction with fluorescent tracers, tissue clearing facilitates the identification of interacting cellular structures, including diverging or

converging nerves and vasculature at their target sites throughout the body. Fine-scale subcellular analysis of cleared specimens using standard protein and nucleic acid probes should also be achievable in the context of cleared tissues.

We have developed a methodology for whole-organism clearing, building upon previous techniques such as CLARITY, SCALE, SeeDB, ClearT, 3DISCO, CUBIC, dibenzyl ether (DBE), and BABB (Murray's Clear) (Becker et al., 2012; Chung et al., 2013; Dodt et al., 2007; Erturk et al., 2012; Hama et al., 2011; Ke et al., 2013b; Kuwajima et al., 2013a; Susaki et al., 2014b). Each of these has made a clear contribution: hydrogel embedding to stabilize tissue structures (Chung et al., 2013), fluorescent protein-compatible clearing reagents (Susaki et al., 2014b), and imaging approaches for large or challenging tissue samples (Becker et al., 2013; Tseng et al., 2009). Although a comprehensive discussion of their respective strengths and weaknesses is beyond the scope of this text, a few critical points merit mention. First, in the original proof-of-principle for each of these techniques, the detailed methods and optimized protocols were only presented for clearing brain tissue, and occasionally for the spinal cord (Erturk et al., 2012; Zhang et al., 2014) or whole embryo (Dodt et al., 2007; Hama et al., 2011). 3DISCO represents, to date, the most complete elucidation of a clearing method in peripheral tissues. However, as is the case with many prior clearing protocols (**Table S1**), 3DISCO's clearing reagents (tetrahydrofuran and DBE) substantially quench fluorescent signals in tissue samples (Erturk et al., 2012). CLARITY (Chung et al., 2013) and CUBIC (Susaki et al., 2014b) bypass the fluorescence quenching problem, but CLARITY in its original form used electrophoretic tissue clearing (ETC) to extract lipids from large samples, which can be challenging to implement and can cause

variability in final tissue quality, including epitope and fine processes damage and tissue browning due to heating (forum.claritytechniques.org). This led to variations of CLARITY using passive lipid extraction (Zhang et al., 2014, with protocol described in detail in Tomer et al., 2014), along with thermal acceleration of clearing and improved imaging. CUBIC also achieves tissue transparency by passively clearing phospholipids and is compatible with hydrogel embedding. The main weakness of passive clearing methods is their slow speed, which makes them unsuited for clearing large tissue volumes or whole organisms.

We here propose a methodology to facilitate fast, whole-brain and whole-body clearing using the circulatory system or the cerebrospinal fluid route to directly deliver clarifying agents. A first step was to optimize the hydrogel embedding, clearing, and imaging reagents, which resulted in **PACT**, for **P**Assive **C**LARITY **T**echnique, for quicker passive lipid extraction of 1-3mm thick tissues. To image PACT-cleared tissue we have developed a **R**efractive **I**ndex **M**atching **S**olution (**RIMS**) - a custom economic recipe, with outcome similar to FocusClear™ (Chung et al., 2013; Moy et al., 2013; Tseng et al., 2009). The PACT reagents were then delivered either intracranially or via the vasculature to achieve whole brain and body clearing and labeling. We term the latter **PARS**, for **P**erfusion-assisted **A**gent **R**elease *in Situ*. All steps for PARS, including preservation, clearing, and labeling, are performed *in situ* prior to tissue extraction. We demonstrate below that PARS, together with RIMS, transform opaque, intact, whole-organisms into optically transparent, fluorescently labeled samples for visualization with conventional confocal microscopy and phenotypic analysis at the cellular, subcellular, and even single-molecule transcripts level.

## Results

### *Optimized Method for Passive Clearing and Immunostaining of Whole Organs in the Rodent*

Similar to the CLARITY method (Chung et al., 2013; Tomer et al., 2014), we render thick tissue optically transparent for imaging in three main steps. First, tissue is cross-linked and hybridized to hydrogel monomers to stabilize biomacromolecules. Second, tissue lipids are extracted from the tissue-hydrogel matrix with ionic detergents. Third, cleared tissue is embedded in RIMS for imaging, or for long-term storage. Although whole-body clearing was our primary goal, we recognized that the processing of small or particularly fragile specimens and organs would best be accomplished by a mild, passive clearing protocol. We developed PACT for rendering rodent whole organs, their 1-3 mm thick sections, including brain, spinal cord, kidney, heart, lung, and intestine, or human tissue biopsies transparent. The clearing speed depends in part on the rate of lipid solvation by detergent micelles, and the rate of diffusion of detergent micelles in tissue (Hoffman, 2002). However, unless an applied force accelerates their diffusion through tissue, such as the electric field in CLARITY's ETC (Chung et al., 2013; Tomer et al., 2014), lipid extraction by large micelles is slow. We tested different detergents at various concentrations for their ability to passively clear 3 mm coronal mouse brain blocks over a 3-day incubation. Sodium dodecyl sulfate (SDS) at all concentrations was superior for lipid solvation and removal from brain tissue relative to other detergents, and moreover, only the 8% SDS concentration achieved uniform clearing throughout the entire 3 mm block (**Figure S1A**).

We hypothesized that a decrease in the cross-link density of the tissue-hydrogel would facilitate both lipid extraction and macromolecule penetration into thick, highly myelinated

or fibrous tissue during subsequent immunohistochemistry. To test this, 1mm brain sections were infused with varying combinations and concentrations of formaldehyde, acrylamide, and bis-acrylamide, degassed, and polymerized at 37 °C. The efficiency of tissue clearing (**Figure 1A**) and the depth of antibody penetration (**Figure 1B**) increased significantly when lower concentrations of formaldehyde and acrylamide were used, and when bis-acrylamide, an acrylamide cross-linking agent used in CLARITY (Tomer et al., 2014), was excluded from the cocktail of hydrogel monomers. Upon observing a qualitative increase in tissue transparency in the tissue-hydrogels prepared with lower acrylamide concentrations (**Figure 1A**), we assayed the different PACT tissue preparations for protein loss, tissue integrity, and changes in weight and volume during clearing to ensure that a minimal crosslinking scheme was sufficient to preserve tissue morphology and molecular information. The amount of protein that leached out of tissue into SDS clearing buffer was statistically indistinguishable between 4% PFA-fixed, uncleared tissue samples (A0P4) that were incubated in PBS as a control, and those cleared tissue-hydrogel matrices prepared with 4% acrylamide (A4P0) or with 4% acrylamide plus 4% PFA (A4P4) (**Figure 1C**). Notably, the amount of protein recorded in the 8% SDS clearing bath solutions for all hydrogel-embedded samples was less than the protein loss ( $0.57 \pm 0.11$  mg per mg gross weight) for the samples preserved only with 4% PFA and incubated in PBS-0.1% TritonX-100, a mild detergent-containing buffer. This implies that hydrogel monomers effectively crosslink and stabilize tissue protein, which is further supported by our finding that unpolymerized, PFA-fixed tissue incubated in 8% SDS showed poor protein retention ( $0.63 \pm 0.02$  mg protein loss per mg gross weight) (**Figure 1C**).

To corroborate these results on the preservation of molecular content in PACT tissue, the relative levels of native eYFP fluorescence were visualized and quantified in PACT brain samples from Thy1-eYFP transgenic mice. While a decrease in mean fluorescence intensity was observed under both hydrogel formulations (A4P0, A2P0), PACT samples showed comparable total intensity relative to uncleared tissue (**Figure 1D**) once the fluorescent measurements were normalized for tissue expansion (**Figure S1C**). Indeed, tissue-hydrogel matrices that were prepared using acrylamide alone (A4P0) exhibited tissue weight and volume changes of ~174% and ~223%, respectively (**Figure 1E**) over A4P4 counterparts. But, upon the transfer of tissue samples from clearing solution to mounting media, PACT samples shrank back to their original size within a few hours (**Figure S3D**). This tissue expansion-contraction has been documented in previous brain clearing protocols (Chung et al., 2013; Hama et al., 2011; Susaki et al., 2014b), wherein it was concluded that these size changes, though suboptimal, did not appear to negatively influence gross tissue morphology or cellular architecture. To visualize the effect of PFA on cross-link density in the tissue-hydrogel matrix, which is hypothesized to limit tissue expansion, PACT-cleared brain slices were imaged via scanning electron microscopy (SEM) (**Figure S1B**). We noted that A2P0 matrices had the largest pore sizes, followed by A4P0, while A4P4 had the smallest visualized pore sizes; pore size directly affects diffusion rate with faster macromolecular diffusion times in tissue-hydrogel matrices with larger pores. Tissue deformity (i.e. expansion and contraction) during PACT processing and mounting did not appear to affect the overall cellular organization or protein content of samples relative to conventional histological processing (**Figure 1F-1L**). Thus, we selected A4P0 for PACT given its balance

between clearing speed, protein retention, and intermediate pore size tissue, which is conducive to macromolecule tissue penetration during histology.

*PACT Reagents are Compatible with Histology and Endogenous Fluorochromes*

To ensure that the signal intensity from genetically encoded fluorescent proteins was preserved throughout PACT processing, 1 mm-thick Thy1-eYFP tissue sections were A4P0-hybridized, PACT-cleared, and imaged using confocal microscopy. Despite PACT clearing, and importantly, the slow image acquisition time for thick samples the genetically expressed eYFP was readily detected throughout the samples (**Figures 1F, 1H**). Furthermore, the tissue-hydrogel matrix still permitted uniform Nissl staining of thick, cleared sections (**Figure 1F**, compared to uncleared 80  $\mu\text{m}$  sections in **Figure 1G**). The overall tissue architecture remained constant between cleared and uncleared sections, as revealed by Nissl staining (red), which assuages concern that successive swelling and then shrinking of tissue caused permanent tissue deformity.

Not only were native proteins including those maintaining the structural integrity of tissue samples, retained by the tissue-hydrogel matrix during clearing (**Figures 1C, 1F, 1H**), but also the cleared tissue blocks were sufficiently macromolecule-permeable to permit labeling of peptidic and nucleic acid epitopes using a variety of common histological markers (e.g. antibodies, small-molecules, mRNA probes). For example, aside from Nissl, 1 mm PACT sections from the mouse brain and spinal cord were immunolabeled with antibodies against anti-tyrosine hydroxylase (TH) (**Figure 1I**); glial fibrillary acidic protein (GFAP), murine immunoglobulin G (IgG), and ionized calcium binding adaptor molecule 1 (Iba1) (**Figure**

**1J**). These targeted moieties represent antigens occupying a wide variety of cellular locations: membrane-localized and cytosolic, neuronal and non-neuronal antigens. PACT clearing decreased light scattering in tissue samples such that all labels were easily resolved across the entire 1 mm section during single-photon fluorescence imaging.

To confirm that PACT methodologies were effective on peripheral tissues as well, the kidney, heart, lung, and intestine of Thy1-eYFP mice were excised, cleared, and labeled with anti-integrin antibodies, acridine orange (AO), and/or SYTO24 (**Figure 1K**). As observed in the central organ samples (**Figure 1F, 1H-J**), small-molecule dyes and antibodies alike rapidly diffused through 1-3 mm thick A4P0-crosslinked and PACT-cleared sections of peripheral organs. While the time for complete immunolabeling of thick sections depends on several factors, including the tissue type, hydrogel pore size (**Figure S1B**), and the extent of lipid removal (**Figures 1A, S1A**), we achieved uniform antibody penetration throughout PACT samples with a 7-12 day incubation. However, for studies that only require labeling with small molecule fluorescent dyes one may obtain rapid staining of 1-3 mm PACT brain sections with a single overnight to 3-day incubation, respectively. Some peripheral tissues were stained even faster, wherein AO labeling of individual nuclei in unsectioned mouse intestinal tissue (~ 400um thick) was attained in under one hour (**Figure 1K**). We then determined if PACT can be applied to pathological samples. Human skin cancer biopsies (**Figure S2A**) were cleared and stained with pan-cytokeratin to visualize tumor cells (**Figure 1L, Figure S2B-C**). In sum, the entire PACT-cleared tissue block was accessible down to the subcellular level to molecular interrogation using standard immunohistochemical methods and conventional fluorescence microscopy.

To determine if PACT is compatible with established procedures to visualize single mRNA transcripts, we subjected PACT-processed tissue to single-molecule fluorescent *in situ* hybridization, smFISH (Femino et al., 1998; Raj et al., 2008). The methodology of smFISH is capable of detecting single RNA molecules with high specificity in fixed cells and its high sensitivity allows for measurements of RNA abundance and subcellular localization. However, smFISH in tissue sections remains challenging due to low signal to noise ratio caused by tissue autofluorescence. Herein,  $\beta$ -actin transcripts in 100  $\mu\text{m}$ -thick cleared mouse brain sections were labeled using 24 Alexa 594-labelled 20mer oligonucleotide probes towards  $\beta$ -actin mRNA. Tissue samples were slide-mounted in media containing 4',6-diamidino-2-phenylindole (DAPI) and imaged via single-photon microscopy.  $\beta$ -actin transcripts were indeed retained in the cytoplasm of neurons throughout PACT and smFISH processing, and single points of fluorescence could be distinguished despite the high copy number of  $\beta$ -actin in cells and the considerable thickness of imaged brain section (Buxbaum et al., 2014; Raj et al., 2008) (**Figure 2A**). PACT tissue exhibited significantly increased contrast of diffraction-limited spots throughout the tissue relative to uncleared tissue (**Figure 2C**). We found that smFISH intensity showed very little difference between PACT cleared and uncleared tissue, while background intensity was significantly reduced (**Figure 2 A-B, 2D and 2E, S2D**). These findings, taken together with the increase in smFISH signal to noise ratio seen in PACT cleared tissues, suggests that background autofluorescence in thick samples is the main factor obscuring smFISH signal in uncleared tissue.

*Recipe for Refractive Index Matching Solution for Imaging and Long-Term Storage of Cleared Tissue*

Effective imaging relies on sample immersion in a mounting media that reduces the refractive index (RI) variations within heterogeneous tissue and that alleviates the RI mismatch between tissue, mounting media and lens immersion media interfaces. In response to the prohibitive cost and limited availability of FocusClear, we formulated an affordable substitute: RIMS, for **R**efractive **I**ndex **M**atching **S**olution, with an RI appropriate for tissue imaging (RI = 1.46), biological safety, and biocompatibility for tissue preservation (see supplemental experimental procedures). To test RIMS, PACT-processed samples were mounted in 80% glycerol, FocusClear, or RIMS, and then imaged under identical conditions (**Figure S3A**). RIMS provided good optical clarity for fluorescence microscopy (**Figure S3C**) and caused minimal quenching of the eYFP signal over a 3-month period (**Figure S3E**). Since its performance appeared to be on par with or exceeds FocusClear (**Figure S3A**) and provided a >10-fold reduction in mounting costs, RIMS was employed for all subsequent PACT and PARS experiments. The exact RIMS formulation can be optimized in a case-specific manner to the RI of tissue samples (**Figure S3B**).

#### *Whole-Body Clearing using the Vasculature in Adult Rodents*

The PACT protocol uses a 4% acrylamide monomer solution to generate the final tissue hydrogel and results in a good combination of protein preservation, speed and ease of clearing, and optical clarity. However passive diffusion is slow, prohibitive for large volume or whole organism clearing. We also noted that the acrylamide hydrogels markedly swelled during the detergent clearing phase (**Figure 1A, S1C**). These two drawbacks, common to most clearing protocols, prompted us to develop an alternate methodology to speed up clearing and also to minimize tissue expansion during clearing. We decided to utilize the

existing vasculature networks, as is done regularly in cardiac perfusion-fixation (Gage et al., 2012; Jonkers et al., 1984), to introduce agents directly to tissue by performing the entire fixation and clearing procedure *in situ*. We term this method **Perfusion-Assisted Agent Release *in Situ*** (or **PARS**). PARS utilizes the intact vasculature of the animal to infuse the hydrogel monomer and clearing solutions directly, which then diffuse throughout the tissues of interest.

To investigate both whether major blood vessels and whole-organism microvasculature was accessed by the perfusate (Leong and Ling, 1990; Li et al., 2012), AlexaFluor 647-conjugated antibodies against mouse immunoglobulin (**Figure S4B**, right) or Atto 647-conjugated nanobodies against GFAP (**Figure S4B**, left) were perfusion-recirculated through cardiac catheters for 24 hours. The mouse brain vasculature was extensively labeled, illustrating the accessibility of blood vessels to perfusate (**Figure S4B**). Perfusate was also observed to diffuse into surrounding tissue, as shown by the extravasculature GFAP labeling (**Figure S4B**, **Supplementary Video 1**).

To recirculate PACT reagents into brain CSF or through whole-body vasculature for several days-to-weeks we developed a closed-loop perfusion system. Using this custom PARS chamber (**Figure S4A**), continuous intracranial perfusion of 8% SDS into CSF, via a method we termed PARS-CSF (**Figure 3**), attained whole-brain clearing in 4 days (**Figure 3A-3B**). Inserting the cannula more caudally into the cisterna magna (**Figure 3A**, right) granted clearing of the entire length of the rat spinal cord (**Figure 3B**). Next, AAV9-eGFP injected adult mice were prepared with a subdural cannula inserted directly above the olfactory bulb

(**Figure 3A**, left), and after 4 days of recirculating 8% SDS at 37 °C, both unmyelinated and densely myelinated mouse brain regions near CSF circulation (most parts of the cortex, hypothalamus, regions near the ventricles and spinal cord) were transparentized). GFP-labeling of individual neurons, neuronal processes, and glial cells was clearly visible throughout the brain (**Figure 3C**).

Herein, we surmised that the same perfusion-clearing method of PARS-CSF could be extended to clearing whole-bodies *in situ*. Furthermore, the application of a pressure gradient on tissue during the lipid extraction and antibody diffusion, respectively, might hold the added benefit of accelerating the clearing and immunolabeling steps relative to PACT-based clearing of individual excised whole-organs. Clearing reagents were cycled through the whole-body vasculature (see timeline, **Figure 4A**), with complete clearing of all peripheral organs and of central nervous system accomplished within 1 week and 2 weeks, respectively, for mice and rats alike (**Figure 4B-4D**, S7). The minimal protein content of the PARS perfusate, and the higher protein content of perfusate from AOP4-infused mice (**Figure 4E**) suggested that the whole-organism hydrogel polymerization was both necessary and sufficient to stabilize gross organ structure and macromolecular content. To confirm that PARS was compatible with visualizing localized fluorescent protein expression in sparsely labeled cells in multiple organs, we delivered a GFP transgene by systemic administration adeno-associated virus (AAV). AAV9:CAG-eGFP (**Figure 5D**) or AAV9BD1:CAG-eGFP, a variant of AAV9 that transduces CNS neurons to a similar extent as AAV9, but exhibits reduced astrocyte and hepatocyte transduction (**Figure 5E**) were delivered via the vasculature in adult mice. In both the brain and the liver, native eGFP expression was readily

detectable and the reduced transduction of liver hepatocytes by AAV9BD1 as compared with AAV9 was easily detected (**Figure 5D versus 5E**).

In comparison to PACT, we predicted that tissue volume changes during PARS processing would be reduced since musculoskeletal structures, such as the skull, the vertebral column, and muscle walls, would physically constrain tissue expansion. Indeed, PARS-based clearing of rodent brains was accomplished with limited hydrogel swelling and tissue expansion during clearing (**Figures 4C-4D, S5A**). Although PARS-processed brains do swell slightly following their extraction from the skull and placement in PBS or RIMS (**Figure S5A**), there was no evidence to suggest that gross changes in neuronal morphology occurred as a result of PARS processing and post-PARS expansion (**Figure 5B**). Nevertheless, we attempted to mitigate tissue swelling in RIMS through post-fixing PARS samples in 4% PFA overnight prior to RIMS mounting. To assess the extent to which overall tissue architecture was altered by volume changes, the intercellular distance and the average cell size within different brain regions (cortex, striatum, thalamus) of uncleared, PARS-cleared, and post-fixed PARS-cleared samples was measured (**Figure S5B**). It was predicted that individual regions may be differentially affected by PARS processing or RIMS incubation; for example, any sheer forces originating from perfusion-related intracranial pressure may exert a greater insult on less myelinated tissue or cause ventricle collapse. Post-fixing PARS samples significantly prevented the increased cell-sizes and intercellular distances that were detected throughout PARS samples. There were no significant differences in cell size or intercellular spacing between uncleared and post-fixed samples in all brain regions assayed (**Figure S5B**).

*Whole-Organism PARS Enables Phenotyping and Imaging in an Organ-by-Organ Fashion*

Following whole-body PARS processing and labeling, major organs were excised, thick-sectioned and imaged using confocal microscopy (**Figures 5, 6, S6**). The PARS-cleared whole-brain (**Figures 5A-B**) and spinal cord (**Figure 5C**) of Thy1-eYFP mice were imaged, and we concluded that PARS processing rendered entire organs optically transparent to the extent that visualizing deep-tissue structures with cellular resolution was possible. Through visualizing individual neurons and nephrons throughout the cleared whole-brain (**Figures 5A-B; Supplementary Video 2**) and kidney (**Figure 6B; Supplementary Video 3**) respectively, we may posit that this optical clarity was achieved while leaving fine cellular structures intact, in part due to the success of *in situ* tissue-hydrogel polymerization in stabilizing tissue architecture, preserving protein content and endogenous fluorescence, and maintaining the spatial relationships between subcellular and cellular tissue components (**Figure 5A-B**). For example, we could resolve individual fluorescently-labeled glomeruli of individual nephrons within 1 mm kidney sections, which establishes the ability of PARS to access peripheral organs through intact vasculature (**Figure 6B, S6**). Importantly, this includes the delivery of all immunohistochemical solutions as well, including blocking solutions, primary and fluorescently-labeled secondary antibody cocktails, or fluorescently-labeled small-molecules, and wash buffers. Immunolabeling using PARS was target-specific, uniformly distributed throughout peripheral organs, and exhibited low background, as illustrated by the tubulin and DRAQ5 labeling in PARS-processed mouse kidney sections (**Figure 5B, Supplementary Video 2**) and by the perfusion-based labeling of blood vessels

in the liver, lung, pancreas with lectin, the filamentous actin probe phalloidin, and the nucleic acid stain DAPI (**Figure S6**).

## **Discussion**

Herein we introduce PARS, a method that renders intact whole-organisms transparent for imaging with single-cell resolution while preserving fluorescent and protein-based signals and tissue architecture. Our starting point, the CLARITY method (Chung et al., 2013) provided scientists with a brain-processing platform for elucidating the 3D cellular arrangement and connectome *in toto*. Numerous laboratories have previously reported on new clearing reagents in the decade before CLARITY, however many of these reagents were highly application- or tissue-specific (summarized in **Table S1**). In contrast, CLARITY introduced two broadly applicable techniques pertaining to tissue preservation (hydrogel embedding) and clearing efficiency (electrophoretic tissue clearing, ETC), both of which could be incorporated into the design, or redesign, of other clearing procedures. Traditionally, making tissue transparent was a process that demanded solvent incubations on the order of weeks-to-months, as reported in other clearing protocols (Hama et al., 2011). ETC, however, challenged the prevailing view that the rate of tissue clearing could only be accelerated through assaying large panels of organic solvents for their ability to solubilize tissue rapidly. Oftentimes, candidate solvents tested in these screens achieved rapid tissue clearing, but compromised tissue structure (Hama et al., 2011) or quenched native fluorescence (Becker et al., 2012; Erturk et al., 2012; Susaki et al., 2014b). Although the reagents introduced by CLARITY are gentler by comparison, the needed ETC step for fast

clearing is complex to implement and causes tissue degradation from sample heating. Although these challenges can be bypassed by the use of passive CLARITY (Tomer et al., 2014) the slow rate of clearing make the technique impractical for scaling up or for whole-body mapping.

With the goal of rapidly clearing whole organisms while still using mild detergents and fluorescence non-quenching reagents throughout, we evolved PARS on the basic principles of CLARITY, but aimed to bypass the need for ETC while maintaining faster clearing than through passive diffusion. First we optimized the clearing agents for passive CLARITY by removing bisacrylamide and increasing the detergent concentration to 8% SDS (PACT reagents). The tissue clearing step was redesigned such that the electrophoretic force used by CLARITY to drive fast lipid extraction was replaced with a perfusion-based pressure gradient. Controlled flow of PACT reagents throughout intact tissue vasculature transforms most peripheral organs into optically transparent tissue within 2-3 days, while whole-mouse and whole-rat brains are rendered transparent within 1 - 2 weeks. Additionally, the self-contained nature of clearing *in situ* also reduced tissue expansion during the monomer infusion and lipid removal.

PARS opens up the possibility of whole-organ and whole organism mapping with high phenotypic content. With this in mind, quick, low resolution scanning of large tissue blocks can direct investigators to restricted areas worthy of slow, high phenotypic content analysis, including smFISH; a method that preserves fluorescent markers long-term is particularly valuable in this respect. Both PACT and PARS methodologies are scalable, cost-effective

relative to the original CLARITY process and theoretically transferrable to other model organisms or human tissue. Indeed, while PARS was depicted using cardiac perfusion in rodents, the overall methodology may also be applicable to instances in which sufficiently large vessels are available for creating a perfusion route, such as whole-organ perfusion in larger, higher order mammals, including isolated human tissue. While PARS does achieve increased speed of clearing and reduced swelling without tissue damage (**Table S1**) the method's unique strength lies in its scalability. Our data demonstrate, for example, that PARS can be employed to assess AAV-mediated transduction at the cellular level in multiple organs after systemic delivery. By eliminating the need to section individual tissues, the PARS approach could expedite efforts to screen numerous AAV serotypes and/or gene regulatory elements for optimal expression in the cell types of interest. In addition to improving screening throughput and speed, a PARS-based whole-body method could also counteract the risk of underestimating AAV transduction in target tissues due to undersampling errors. Similarly, PARS holds the potential to refine our understanding of peripheral nerves at their target whole-organs. Accurate maps of complex long-range fiber bundles, such as for the vagus nerve (George et al., 2000), could help inform improvements in existing therapies or spur the development of entirely novel therapeutic strategies, such as for bioelectronics medicines (Famm, 2013). PARS can also facilitate biomedical work in brain-to-body interconnections, in whole-body screening experiments for off- and on-target agents, and in whole-organ mapping for sparse elements such as tumor cells or stem cells. Lastly, the PARS method is compatible with cell-filling endoskeletal structures. By combining PARS with TEMPEST – a precursor to CLARITY (Deisseroth and Gradinaru, 2014) – the *in vivo* expression of long-lasting keratin filaments (that outlive the cells themselves while keeping

a loyal blueprint of the morphology) within populations of interest can facilitate accurate post-mortem quantification and mapping of long-degenerated cells throughout the brain.

The methods we introduce here builds upon our prior work in CLARITY to expand tissue clearing and phenotyping to whole organisms by using the intrinsic circulatory system. Because the vascular network is not homogeneous, leading to non-uniform perfusive flow, organs of interest will clear at different rates. To achieve optimal clearing while retaining high tissue content, further validation for specific applications and technical improvements will be necessary. The blood-brain barrier may present a challenge to efficient perfusion-based transport of particularly large molecules such as antibodies (150 kDa) to the brain relative to the periphery. To improve perfusion efficiency, one solution likely will be to develop (or utilize when already available) smaller antibody scaffolds for immunolabeling; these include the fragment-antigen-binding format of immunoglobulins (Fab ~50 kDa), and nanobodies, single domain antibodies derived from camelid antibodies, whose smaller size (~12-15 kDa) promotes tissue permeability (Harmsen and De Haard, 2007).

Improved imaging platforms will also be needed to take full advantage of all the recent tissue clearing work, ours and others (Becker et al., 2012; Chung et al., 2013; Dodt et al., 2007; Ertürk et al., 2012; Ertürk and Bradke, 2013; Hama et al., 2011; Ke et al., 2013a; Kuwajima et al., 2013b; Susaki et al., 2014a). In order to obtain cellular and subcellular information in thick cleared tissue, it is necessary to utilize long-working distance objectives while still preserving high magnification and numerical aperture. Scanning speed is an additional barrier with cleared tissue blocks taking many days to be fully imaged – resonant scanners

or light-sheet microscopy (Tomer et al., 2014) can accelerate the process while retaining high-resolution data.

Given increasing interest in the link between the brain and peripheral organs (Birmingham et al., 2014), it will be critical to have an unsegmented view of the whole-body, with structural connections between the brain and peripheral organs left intact. Through the development of PARS and enabling technologies (nanobodies, imaging platforms) it is becoming possible not only to facilitate neuroscientists' overarching goal of creating a brain connectome, but also to facilitate elucidation of a brain-to-body-and-back connectome as well as the phenotyping of every other organ system in the body, healthy or diseased.

#### **AUTHOR CONTRIBUTION**

BY, JT, and VG conceived the project. BY, JT, RPK, BD, CKC, EL, SS, LC, and VG planned and executed experiments. BY, JT, VG made the figures and wrote the paper with input from all other authors. VG supervised all aspects of the work.

#### **ACKNOWLEDGEMENTS**

We thank the entire Gradinaru lab for helpful discussions. We also thank Drs. Dianne Newman and David Anderson for helpful discussions and suggestions. We thank Drs. Amir Arbabi and Andrei Faraon for assistance with SEM imaging. We thank Leica Microsystems

for acquiring some of the images presented with a Leica TCS SP8 with Leica HC FLUOTAR L 25x/1.00 IMM CORR objective designed for CLARITY imaging.

BD and VG especially wish to acknowledge the contributions of Paul H. Patterson ( - 2014), whose desire to apply tissue clearing to unresolved questions in neuroscience pushed us to further evolve these methods.

This work was funded by: the NIH / NINDS New Innovator (NIH IDP20D017782-01); NIH 1R01AG047664-01; Startup funds from the President and Provost of California Institute of Technology and the Biology and Biological Engineering Division of California Institute of Technology; the Beckman Institute of Caltech; the Pew Charitable Trust; Kimmel Foundation (to VG). And NIH R01HD075605 (to LC).

VG is also supported by: Human Frontiers in Science Program, the Mallinckrodt Foundation, the Gordon and Betty Moore Foundation, the Michael J. Fox Foundation, Caltech-GIST, NIH 1R01NS085910-01, NIH 1R21MH103824-01.

C-K.C., S.S., E.L., acknowledge support from the Caltech Biology Division Training grant (NIH/NRSA 5T32GM07616). R.P.K. acknowledges support from NIH/NIAMS (5T32AR058921). J.B.T. acknowledges the Colvin Postdoctoral Fellowship and CALTECH Division of BBE.

## Methods

**PACT Clearing:** 4% paraformaldehyde (PFA)-fixed tissue sections were incubated at 4 °C overnight in the hydrogel monomer solution A4P0 (4% acrylamide in PBS) supplemented with 0.25% photoinitiator 2,2'-Azobis[2-(2-imidazolin-2-yl)propane]dihydrochloride (VA-044, Wako Chemicals USA, Inc.). A4P0-infused samples were degassed with nitrogen for 1-5 minutes and then incubated for 2-3 hours at 37 °C to initiate tissue-hydrogel hybridization. After removing excess hydrogel via brief PBS washes, tissue-hydrogel matrices were transferred into 50 mL conical tubes containing 8% SDS in 0.1M PBS (pH 7.5), and depending on tissue size, were incubated for 2-5 days at 37 °C with shaking. For immunostaining, 1-3 mm thick PACT-processed samples were washed in PBS with 4-5 buffer changes over the course of a day and then transferred to buffer containing small-molecule dyes or primary antibodies followed by fluorescently-conjugated secondary antibody (1:200-400, in PBS containing 2% normal donkey serum, 0.1% TritonX-100 and 0.01% sodium azide) for 3-7 days or with small-molecule dyes for 1-3 days. Antibody or small molecule dye solutions need to be replaced every day. Unbound antibody was removed via PBS washes, as before, and then samples were incubated with secondary antibodies (Fab fragment secondary antibodies are preferred, 1:200-400) for 2-5 days then washed for 1 day in PBS or phosphate buffer (PB) prior to incubation in imaging media (RIMS). All staining and mounting steps were conducted at room temperature with gentle shaking.

**RIMS Imaging Media (RI 1.47):** 40 g of Sigma D2158 (Histodenz) in 30ml of 0.02M PB with 0.1% tween-20 and 0.01% sodium azide, pH to 7.5 with NaOH – which results in a final concentration of 88% Histodenz w/v. Samples are incubated in RIMS until transparent (~ 1 day for PACT samples, up to 1 week for PARS cleared brains), followed by mounting in fresh RIMS.

**smFISH:** 100 µm PACT sections were ethanol-permeabilized, labeled with 24 Alexa 594-labeled 20mer oligo probes towards B-actin (overnight incubation at 37 °C), washed and coverslipped with Slowfade Gold + DAPI according to published protocols (Buxbaum et

al., 2014; Lyubimova et al., 2013). Laplacian of Gaussian filtering with a radius of 3 was applied to visualize transcripts in both cleared and uncleared samples.

**PARS Protocol:** Immediately following standard cardiac perfusion with 4% PFA (in PBS, pH 7.4), the fixed rodent was transferred onto a perfusion chamber (**Figure S4A**) which recirculated all subsequent PACT and immunolabeling reagents (as above) continuously (1 ml/min) through rodent vasculature via a peristaltic pump. Perfusion tubing connected the chamber to a feeding needle inserted through the left ventricle into the aorta and loosely sutured in place. The rodent was post-fixed with 4% PFA for 1 hour and then perfusion-washed with PBS for 1 hour. A4P0 monomer was cycled through vasculature overnight, followed by a 2 hour PBS perfusion wash. Before polymerization and without disconnecting perfusion lines, the perfusion chamber was placed into a ziplock bag (**Figure S4A**), and the bag containing the chamber with rodent was degassed for 2 minutes under nitrogen gas. Polymerization was initiated via perfusion-recirculation of 200mL of 0.25% VA-044 initiator in PBS at 37°C for 2-3 hours. The whole-body was cleared through a  $\leq$  2-week perfusion with 8% SDS in PBS, pH 7.5 at 37-42 °C followed by extensive PBS perfusion-washing over 2-3 days. Antibodies and small-molecule dyes (as above in PACT) were then delivered via a 3-day perfusion and 1-day wash.

For the **PARS-CSF** variation of brain or spinal cord clearing (**Figure 3A-B**), transcardially-fixed rodents were decapitated and a subdural cannula was inserted above the region of interest and cemented to the skull. All PARS reagents are delivered in the same order and timeframe as PARS at 1ml/min

**AAV production and systemic delivery:** Single stranded ssAAV-CAG-eGFP vectors packaged into AAV9 or the AAV9 variant capsid, AAV2/9BD1, was generated and purified as described (Lock et al., 2010). The AAV2/9BD1 capsid was modified from AAV2/9 (U. Penn) with, amongst others, an N498Y mutation to reduce liver transduction (Pulicherla et al., 2011).  $1 \times 10^{12}$  vector genomes (vg) of either virus was delivered intravenously into mice and tissue assessed 6 months later by PARS for native eGFP fluorescence.

**Fluorescence Microscopy:** Cleared tissue samples were mounted in RIMS at room temperature using spacers from 0.5 mm – 7 mm depending on sample thickness (iSpacer, SunJin Lab Co.; Silicone Isolator, Electron Microscopy Sciences, PA) and coverslipped. For Figure 3B, the samples were imaged by Leica Microsystems using a Leica TCS SP8 two-photon microscope with the Leica HC FLUOTAR L 25x/1.00 IMM CORR objective (working distance, w.d. 6.0 mm). Other images were taken using a Zeiss LSM 780 single-photon microscope with either the Fluar 5x/0.25 M27 dry objective (w.d. 12.5 mm), Plan-Apochromat 10x/0.45 M27 air objective (w.d. 2.0 mm), LD SC Plan-Apochromat 20x/1.0 Corr M32 85mm scale-immersion objective (w.d. 5.6 mm), or LD LCI Plan-Apochromat 25x/0.8 Imm Corr DIC M27 multi-immersion objective (w.d. 0.57 mm). Image reconstructions were performed using Imaris imaging software (Bitplane). After imaging, samples were stored in RIMS at room temperature.

For more detailed methods see Extended Supplemental Procedures and Table S2 for a detailed list of reagents/buffers.

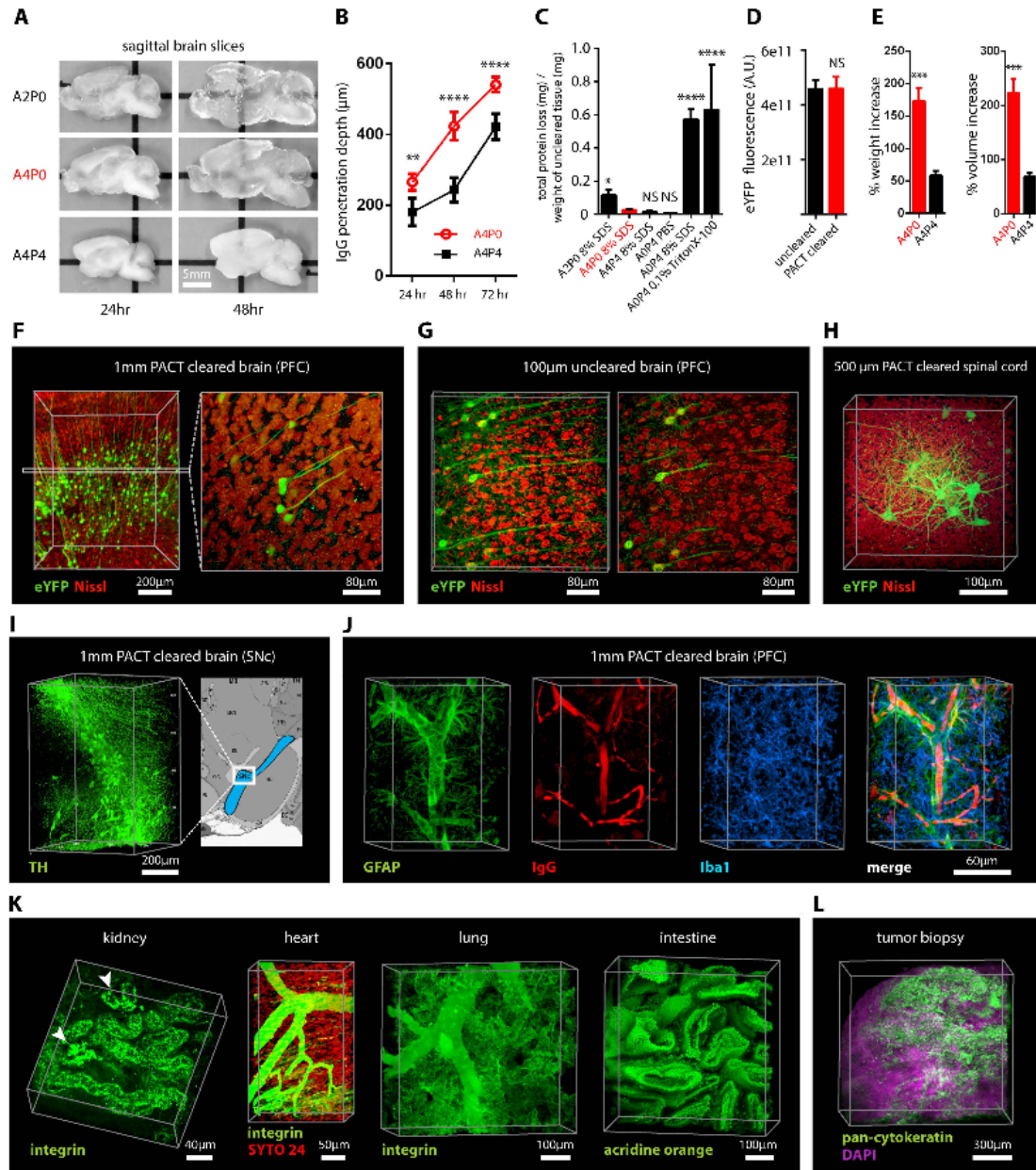
## References

- Becker, K., Jahrling, N., Saghafi, S., and Dodt, H.U. (2013). Ultramicroscopy: light-sheet-based microscopy for imaging centimeter-sized objects with micrometer resolution. *Cold Spring Harbor protocols* 2013, 704-713.
- Becker, K., Jahrling, N., Saghafi, S., Weiler, R., and Dodt, H.U. (2012). Chemical clearing and dehydration of GFP expressing mouse brains. *PLoS One* 7, e33916.
- Buxbaum, A.R., Wu, B., and Singer, R.H. (2014). Single  $\beta$ -Actin mRNA Detection in Neurons Reveals a Mechanism for Regulating Its Translatability. *Science* 343, 419-422.
- Chung, K., and Deisseroth, K. (2013). CLARITY for mapping the nervous system. *Nature methods* 10, 508-513.
- Chung, K., Wallace, J., Kim, S.Y., Kalyanasundaram, S., Andalman, A.S., Davidson, T.J., Mirzabekov, J.J., Zalocusky, K.A., Mattis, J., Denisin, A.K., *et al.* (2013). Structural and molecular interrogation of intact biological systems. *Nature* 497, 332-337.
- Deisseroth, K.A., and Gradinaru, V. (2014). Functional Targeted Brain Endoskeletonization.
- Dodt, H.-U., Leischner, U., Schierloh, A., Jahrling, N., Mauch, C.P., Deininger, K., Deussing, J.M., Eder, M., Zieglgansberger, W., and Becker, K. (2007). Ultramicroscopy: three-dimensional visualization of neuronal networks in the whole mouse brain. *Nature methods* 4, 331-336.
- Ertürk, A., Becker, K., Jahrling, N., Mauch, C.P., Hojer, C.D., Egen, J.G., Hellal, F., Bradke, F., Sheng, M., and Dodt, H.-U. (2012). Three-dimensional imaging of solvent-cleared organs using 3DISCO. *Nature protocols* 7, 1983-1995.
- Ertürk, A., and Bradke, F. (2013). High-resolution imaging of entire organs by 3-dimensional imaging of solvent cleared organs (3DISCO). *Experimental neurology* 242, 57-64.
- Famm, K. (2013). Drug discovery: a jump-start for electroceuticals. *Nature* 496, 300.
- Femino, A.M., Fay, F.S., Fogarty, K., and Singer, R.H. (1998). Visualization of Single RNA Transcripts in Situ. *Science* 280, 585-590.
- Gage, G.J., Kipke, D.R., and Shain, W. (2012). Whole animal perfusion fixation for rodents. *Journal of visualized experiments : JoVE*.
- George, M.S., Sackeim, H.A., Rush, A.J., Marangell, L.B., Nahas, Z., Husain, M.M., Lisanby, S., Burt, T., Goldman, J., and Ballenger, J.C. (2000). Vagus nerve stimulation: a new tool for brain research and therapy. *Biological psychiatry* 47, 287-295.
- Hama, H., Kurokawa, H., Kawano, H., Ando, R., Shimogori, T., Noda, H., Fukami, K., Sakaue-Sawano, A., and Miyawaki, A. (2011). Scale: a chemical approach for fluorescence imaging and reconstruction of transparent mouse brain. *Nature neuroscience* 14, 1481-1488.
- Harmsen, M.M., and De Haard, H.J. (2007). Properties, production, and applications of camelid single-domain antibody fragments. *Applied Microbiology and Biotechnology* 77, 13-22.
- Hoffman, A.S. (2002). Hydrogels for biomedical applications. *Advanced Drug Delivery Reviews* 54, 3-12.

- Jonkers, B., Sterk, J., and Wouterlood, F. (1984). Transcardial perfusion fixation of the CNS by means of a compressed-air-driven device. *Journal of neuroscience methods* *12*, 141-149.
- Ke, M.-T., Fujimoto, S., and Imai, T. (2013a). SeeDB: a simple and morphology-preserving optical clearing agent for neuronal circuit reconstruction. *Nature neuroscience* *16*, 1154-1161.
- Kim, S.Y., Chung, K., and Deisseroth, K. (2013). Light microscopy mapping of connections in the intact brain. *Trends in Cognitive Sciences* *17*, 596-599.
- Kuwajima, T., Sitko, A.A., Bhansali, P., Jurgens, C., Guido, W., and Mason, C. (2013a). Clear(T): a detergent- and solvent-free clearing method for neuronal and non-neuronal tissue. *Development* *140*, 1364-1368.
- Leong, S.K., and Ling, E.A. (1990). Labelling neurons with fluorescent dyes administered via intravenous, subcutaneous or intraperitoneal route. *Journal of neuroscience methods* *32*, 15-23.
- Li, T., Bourgeois, J.P., Celli, S., Glacial, F., Le Sourd, A.M., Mecheri, S., Weksler, B., Romero, I., Couraud, P.O., Rougeon, F., *et al.* (2012). Cell-penetrating anti-GFAP VHH and corresponding fluorescent fusion protein VHH-GFP spontaneously cross the blood-brain barrier and specifically recognize astrocytes: application to brain imaging. *FASEB journal : official publication of the Federation of American Societies for Experimental Biology* *26*, 3969-3979.
- Lock, M., Alvira, M., Vandenberghe, L.H., Samanta, A., Toelen, J., Debyser, Z., and Wilson, J.M. (2010). Rapid, simple, and versatile manufacturing of recombinant adeno-associated viral vectors at scale. *Hum Gene Ther* *21*, 1259-1271.
- Lyubimova, A., Itzkovitz, S., Junker, J.P., Fan, Z.P., Wu, X., and van Oudenaarden, A. (2013). Single-molecule mRNA detection and counting in mammalian tissue. *Nat Protocols* *8*, 1743-1758.
- Moy, A.J., Wiersma, M.P., and Choi, B. (2013). Optical histology: a method to visualize microvasculature in thick tissue sections of mouse brain. *PLoS One* *8*, e53753.
- Plotnikov, S., Juneja, V., Isaacson, A.B., Mohler, W.A., and Campagnola, P.J. (2006). Optical clearing for improved contrast in second harmonic generation imaging of skeletal muscle. *Biophysical journal* *90*, 328-339.
- Pulicherla, N., Shen, S., Yadav, S., Debbink, K., Govindasamy, L., Agbandje-McKenna, M., and Asokan, A. (2011). Engineering liver-detargeted AAV9 vectors for cardiac and musculoskeletal gene transfer. *Molecular therapy : the journal of the American Society of Gene Therapy* *19*, 1070-1078.
- Raj, A., van den Bogaard, P., Rifkin, S.A., van Oudenaarden, A., and Tyagi, S. (2008). Imaging individual mRNA molecules using multiple singly labeled probes. *Nat Meth* *5*, 877-879.
- Spalteholz, W. (1914). *Über das Durchsichtigmachen von menschlichen und tierischen Präparaten* (Leipzig: S. Hierzel).
- Steinke, H., and Wolff, W. (2001). A modified Spalteholz technique with preservation of the histology. *Annals of anatomy = Anatomischer Anzeiger : official organ of the Anatomische Gesellschaft* *183*, 91-95.
- Susaki, E.A., Tainaka, K., Perrin, D., Kishino, F., Tawara, T., Watanabe, T.M., Yokoyama, C., Onoe, H., Eguchi, M., and Yamaguchi, S. (2014a). Whole-Brain Imaging with Single-Cell Resolution Using Chemical Cocktails and Computational Analysis. *Cell*.

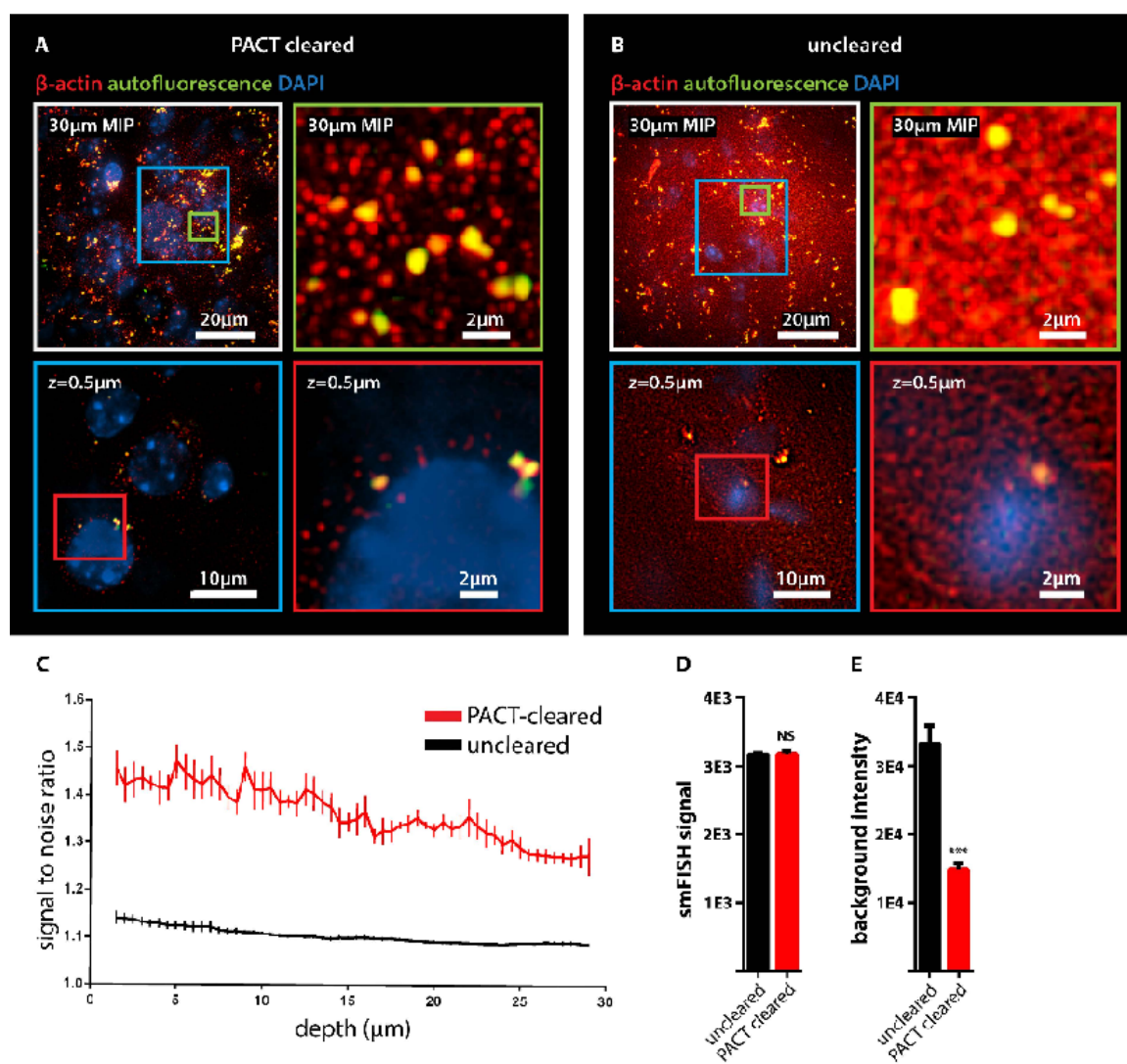
- Susaki, E.A., Tainaka, K., Perrin, D., Kishino, F., Tawara, T., Watanabe, T.M., Yokoyama, C., Onoe, H., Eguchi, M., Yamaguchi, S., *et al.* (2014b). Whole-Brain Imaging with Single-Cell Resolution Using Chemical Cocktails and Computational Analysis. *Cell*.
- Tomer, R., Ye, L., Hsueh, B., and Deisseroth, K. (2014). Advanced CLARITY for rapid and high-resolution imaging of intact tissues. *Nature protocols* *9*, 1682-1697.
- Tseng, S.J., Lee, Y.H., Chen, Z.H., Lin, H.H., Lin, C.Y., and Tang, S.C. (2009). Integration of optical clearing and optical sectioning microscopy for three-dimensional imaging of natural biomaterial scaffolds in thin sections. *Journal of biomedical optics* *14*, 044004.
- Zhang, M.D., Tortoriello, G., Hsueh, B., Tomer, R., Ye, L., Mitsios, N., Borgius, L., Grant, G., Kiehn, O., Watanabe, M., *et al.* (2014). Neuronal calcium-binding proteins 1/2 localize to dorsal root ganglia and excitatory spinal neurons and are regulated by nerve injury. *Proceedings of the National Academy of Sciences of the United States of America* *111*, E1149-1158.

Figure 1.



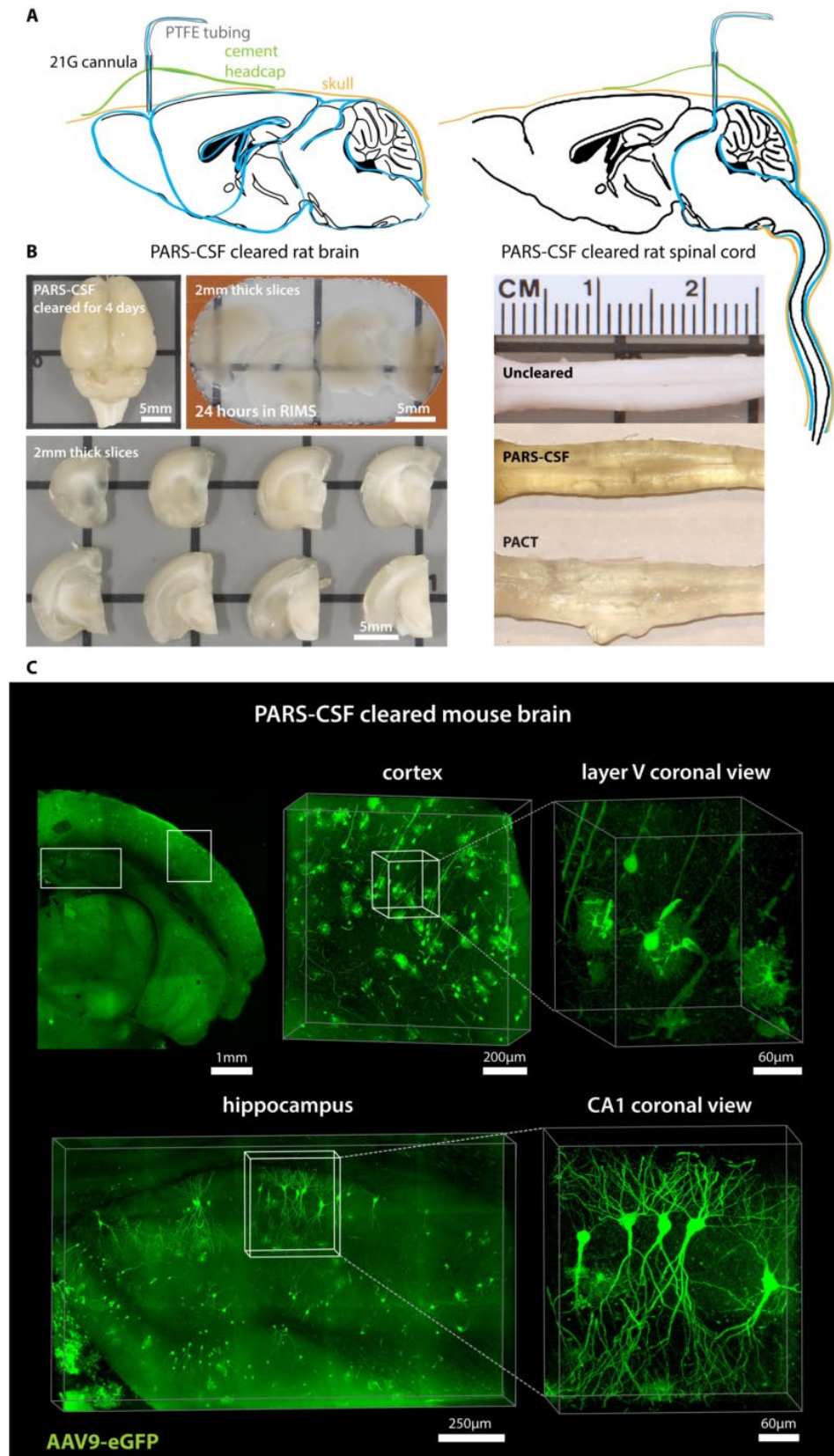
**Figure 1: PACT clearing of A4P0 tissue-hydrogel hybrid achieves optimal transparency and immunohistochemistry compatibility across organs.** (A) Optical transparency comparison of 3 mm adult mouse sagittal blocks of A2P0, A4P0, and A4P4 tissue-hydrogel hybrid cleared for 24 h and 48 h. (B) Compared to A4P4, A4P0 tissue-hydrogel hybrid showed faster antibody penetration (n=6 fields of view per sample). (C) The percentage of protein loss from 1 mm mouse brain slices (n=6 slices for each clearing condition); statistical significance is shown for each condition vs. A4P0 8% SDS (red). (D) The integrated eYFP fluorescence intensity in arbitrary units (A.U.) of uncleared and cleared 1 mm Thy1-eYFP mouse brain slices (n=6 slices). (E) Compared to A4P4, the A4P0 hydrogel-tissue hybrid showed higher tissue expansion and weight gain post clearing. (F-H) Thy1-eYFP mouse sections stained with Nissl: (F) 1 mm cleared brain slice, prefrontal cortex (PFC) area (left: z = 1 mm imaging stack depth); (G) 1 mm uncleared brain slice, PFC (left: z = 100  $\mu$ m imaging stack depth); (H) 1 mm spinal cord slice (z = 500  $\mu$ m). (I) Substantia nigra pars compacta (SNc) of 1 mm mouse brain slice stained with anti-tyrosine hydroxylase (TH) antibody (z = 1 mm). (J) PFC of 1 mm adult mouse brain slices stained with antibodies against GFAP, mouse-IgG, and Iba1 (z = 1 mm). (K) 1 mm section of mouse kidney (z = 150  $\mu$ m; arrowheads show glomeruli), heart (z = 320  $\mu$ m), lung (z = 550  $\mu$ m) and intestine (z = 350  $\mu$ m) stained with anti-integrin antibodies, SYTO24, and acridine orange. (L) PACT-cleared human tissue biopsy from basal cell carcinoma (BCC) was stained with anti-pan-cytokeratin (AE1/AE3) Alexa Fluor 488 primary antibody to label endothelial cells and DAPI (700  $\mu$ m imaging stack depth). All graphs are shown in mean  $\pm$  SEM. Statistical significance: for paired samples: 2-tailed Student's *t* test; for multiple comparisons: one-way ANOVA followed by Bonferroni posthoc (\**p* < 0.05, \*\**p* < 0.01, \*\*\**p* < 0.005, and \*\*\*\**p* < 0.0001). All confocal imaging; for objectives see Supplemental Methods. Also see Figure S1-3 and Tables S1-2.

Figure 2.



**Figure 2: Detection of individual mRNA transcripts in PACT tissue sections by smFISH.** 100 $\mu$ m-thick mouse brain slices were hybridized with twenty-four 20mer oligonucleotide probes towards  $\beta$ -actin mRNA labeled with Alexafluor 594. **(A)** PACT-cleared smFISH brain slices. Upper panel shows 30  $\mu$ m maximum intensity projection. An abundant number of diffraction limited spots corresponding to single beta-actin mRNAs (red) were readily detected up to 30  $\mu$ m in depth under 589nm illumination. Note bright amorphous granules (yellow) are background lipofuscin vesicles that show up in both 589nm(red) and 532nm autofluorescence (green) channels, whereas smFISH signals are in the red channel only. **(B)** Compared to PACT cleared slices, smFISH in uncleared brain slices showed significantly decreased contrast. (Lower panels in **A** and **B** show single slices of 0.5  $\mu$ m at 12  $\mu$ m depth; the images were processed from raw data using the same contrast scale and Laplacian of Gaussian filtering; for raw data see **Figure S2D**) **(C)** Signal to noise ratio as a function of depth shows PACT-clearing tissue increases the signal to noise ratio of smFISH throughout the thickness of the sample as compared to uncleared tissue. **(D)** smFISH intensities show no appreciable differences between uncleared and PACT-cleared tissue.  $p = 0.8722$ ; 2-tailed Student's  $t$  test. **(E)** Comparison of background intensity between uncleared and PACT-cleared tissue illustrates the significant reduction of background fluorescence in PACT-cleared tissue.  $p = 0.0006$ ; 2-tailed Student's  $t$  test. All graphs are shown in mean  $\pm$  SEM. For microscopy see Supplemental Methods.

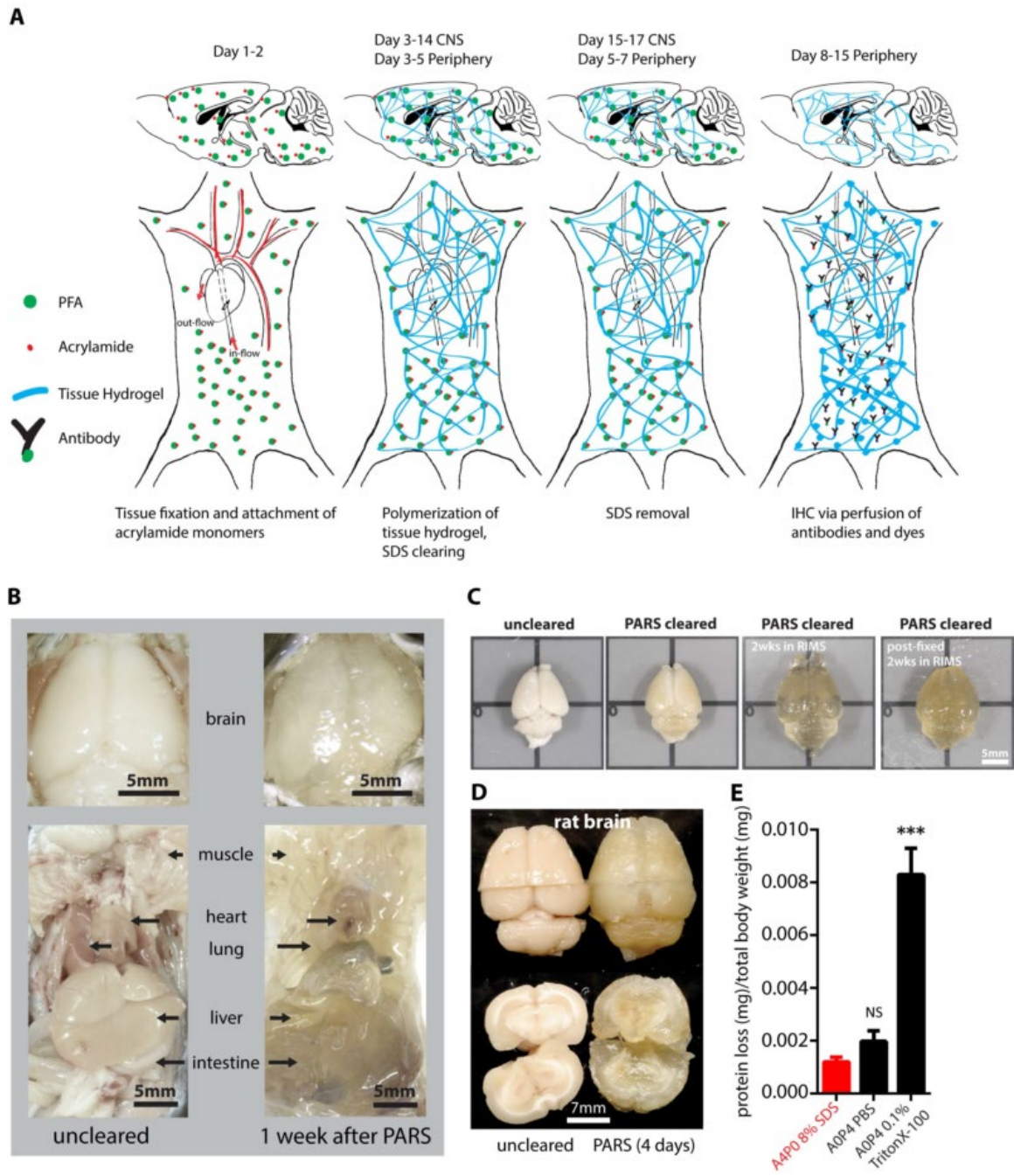
Figure 3



**Figure 3: PARS-CSF: a protocol for rapid whole-brain or spinal cord clearing and labeling via the cerebrospinal fluid route (CSF) using perfusion-assisted agent release *in situ* (PARS).**

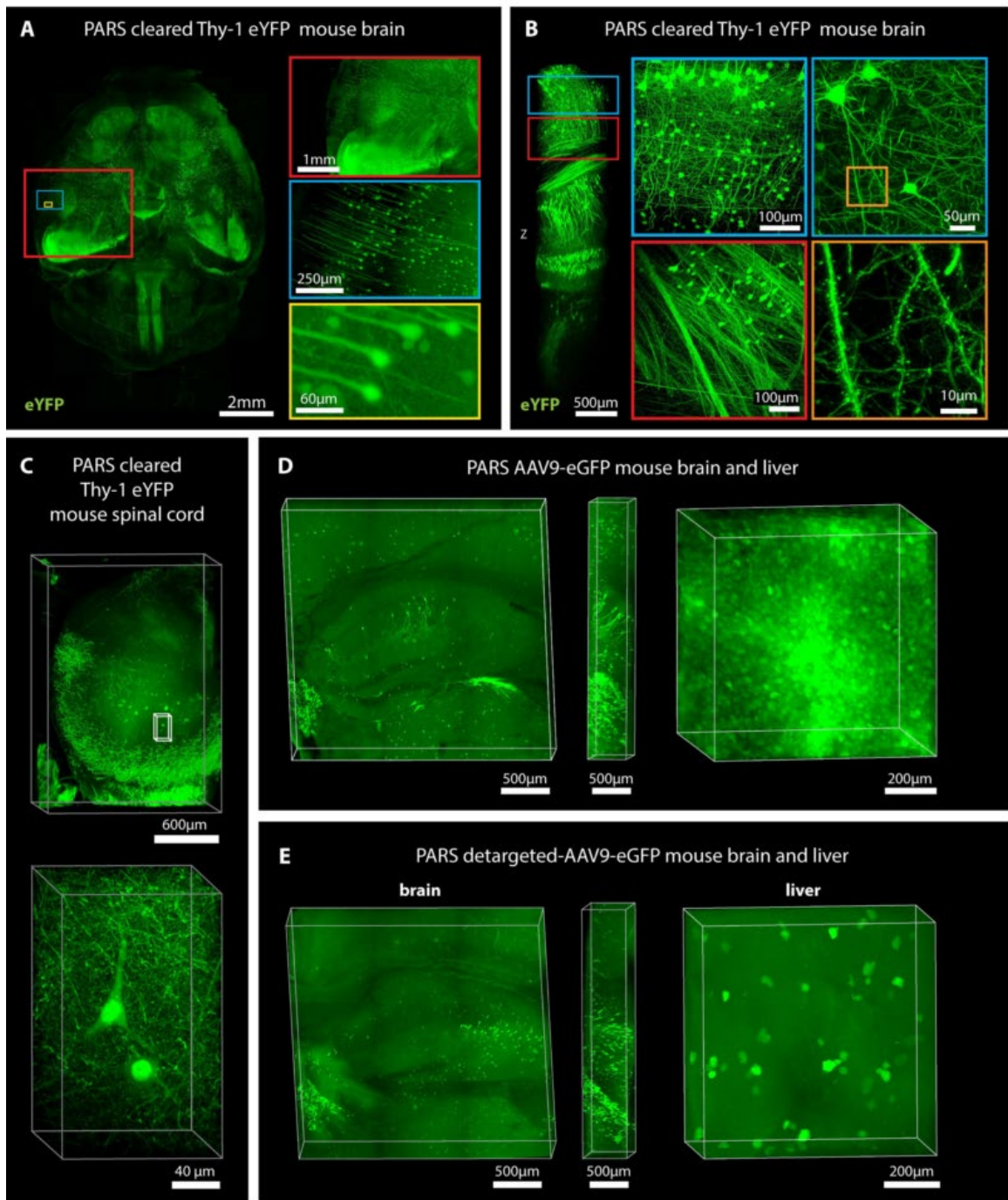
(A) CNS tissue may be rendered transparent optically transparent by the direct perfusion of all PARS reagents into the CSF via an intracranial brain shunt inserted either (left) below the dura in the region directly above the olfactory bulb, or into the cisterna magna (or placed directly above the dorsal inferior colliculus, right). The cannula, which is connected to the perfusion lines may be cemented into position with dental acrylic. (B) Whole-brain and the corresponding 2 mm thick slices (left) and whole-spinal cord (right) from PARS-CSF rats that were cleared at 37 °C for 4-days (brain) or for 2-weeks (spinal cord) are shown. The extent of whole-brain clearing is dependent on brain tissue proximity to the cannula: the frontal lobe was rendered optically transparent, whereas the mid-hind brain were only weakly cleared (see 2 mm slices on right side of panel). After 24-hour incubation in RIMS, PARS-CSF brain slices were sufficiently cleared for imaging without further sectioning. (C) Images show native eGFP fluorescence in 500  $\mu$ m PARS-CSF cleared coronal brain slices prepared from mice that, 6-months prior to clearing, received IV injections with AAV9:CAG-eGFP. Representative sections of cortex and hippocampus are presented at higher magnification in image boxes (right). In the layer V coronal view, an AAV9 transduced eGFP-expressing glial cell and eGFP-neuron adjacent to a blood vessel are clearly visible. In the hippocampus (bottom), the finer neuronal processes of eGFP-expressing CA1 neurons may be visualized with high resolution, which suggests that PARS-CSF may be completed without severe damage to cellular morphology. For microscopy see Supplemental Methods. Also see Figure S4.

**Figure 4**



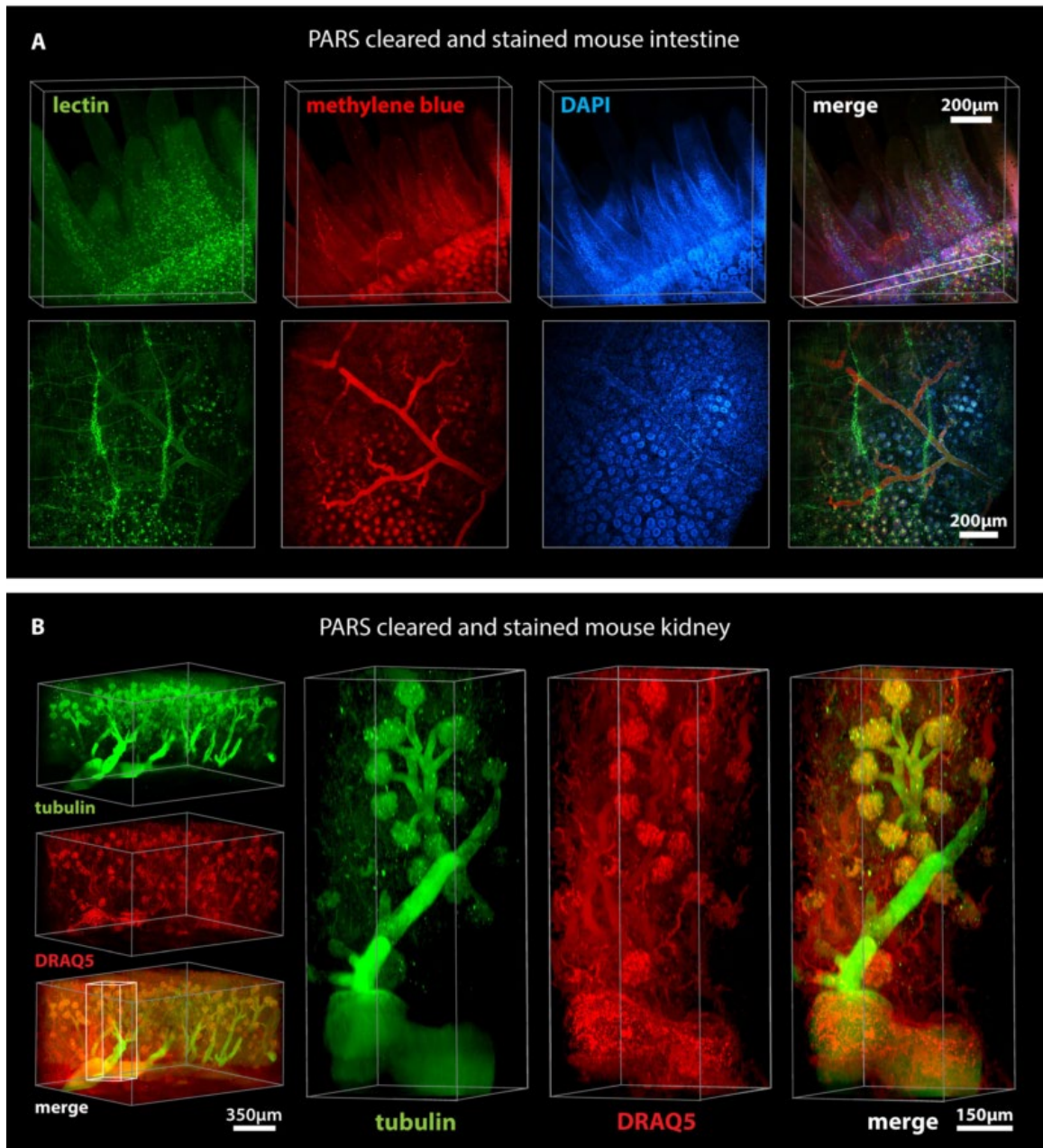
**Figure 4: PARS achieves whole-body clearing.** (A) Schematic of PARS clearing and immunostaining. (B) A comparison of optical transparency of mouse brains and peripheral organs before and after PARS clearing. (C) Representative images of relative mouse brain size before (first box, from left) and after (second box) 2 weeks of PARS clearing shows that PARS circumvents hydrogel swelling and brain tissue expansion during the clearing process. Brain tissue expands gradually after immersion in RIMS (third box); this volume change may be mitigated via post-fixing PARS samples in 4% PFA overnight prior to RIMS mounting (fourth box). (D) Representative images of relative rat brain size before (right) and after (left) 4-days of PARS clearing, showing how PARS is a scalable method. Coronal slices of rat whole-brain samples show gross tissue morphology, highlighting that unmyelinated areas may be cleared within 4-days of PARS-based clearing. (E) Protein loss of PARS clearing compared to other clearing methods (n = 4 mice for each); graph shows mean  $\pm$  s.e.m.; one way ANOVA followed by Bonferroni posthoc test was used to determine statistical significance in comparison to A4P0 8% SDS PARS clearing. \* indicates  $p < 0.05$  and \*\* indicates  $p < 0.01$ . Images for (B-D) were taken using bright field camera. Also see Figure S4, S7, S3E, and Supplemental Movie 1.

Figure 5



**Figure 5: PARS enables whole-brain mapping of widespread and sparse genetically encoded fluorescent signals with subcellular resolution.** (A) Whole brain image ( $z = 6$  mm), and (B) deep-brain imaging ( $z = 4$  mm) of adult Thy1-eYFP mouse after PARS clearing for 10 days. The boxes on the right show high magnification images of indicated areas. (C) Spinal cord image of adult Thy1-eYFP mouse after PARS clearing for 2 weeks ( $z = 2$  mm). Lower panel shows high magnification images of indicated region ( $z = 1.2$  mm). (D) Images show native eGFP fluorescence in 1 mm coronal brain slices (left) and liver (right) prepared from the PARS cleared mice that received IV injections of AAV9:CAG-eGFP. Image columns to the right of each coronal brain image show the orthogonal views ( $z = 0.5$  mm). (E) Native eGFP fluorescence in 1 mm coronal brain slices (left) and liver (right) prepared from PARS cleared mice injected with a liver detargeted variant, AAV9BD1:CAG-eGFP. Image columns to the right of each coronal brain image show the orthogonal views ( $z = 0.5$  mm). For microscopy see Supplemental Methods. Also see Figure S5 and Supplemental Movie 2 (for 5B).

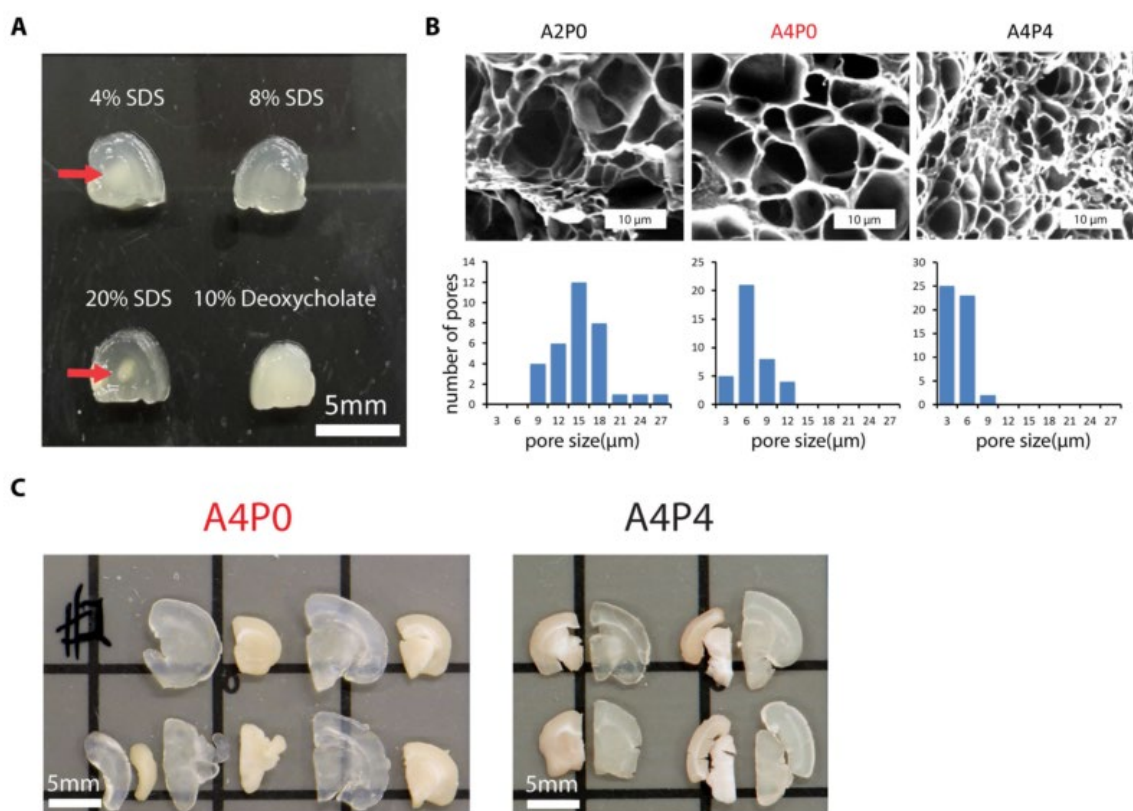
Figure 6



**Figure 6: PARS allows rapid and uniform clearing and immunolabeling of peripheral organs.**

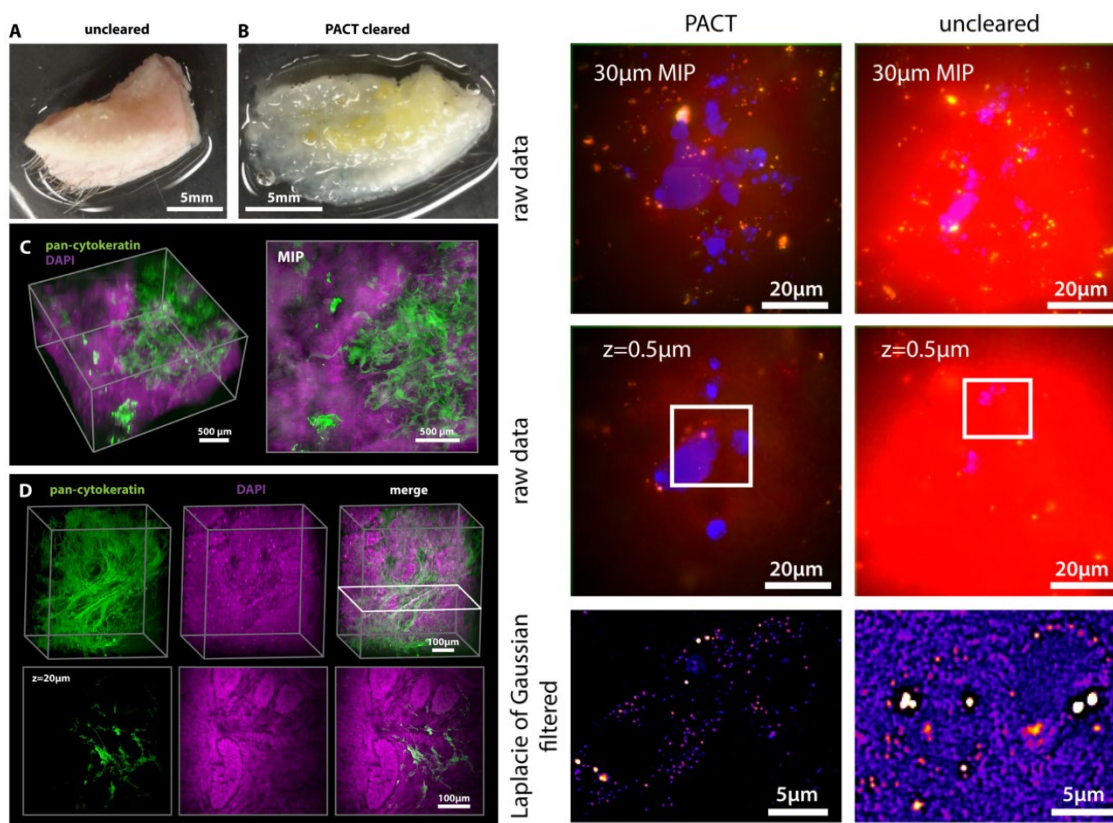
Clearing and immunohistochemical labeling was achieved in whole mice through PARS alone. **(A)** PARS-cleared mouse intestine was stained with lectin, methylene blue, and DAPI, and imaged through a depth of 500  $\mu\text{m}$ . Lower panels shows maximum intensity projection of above rendering,  $z = 50 \mu\text{m}$ . ( $z = 500 \mu\text{m}$ ). **(B)** A 1 mm thick kidney section was imaged (left) for anti-tubulin antibody and DRAQ5 labeling. Right panels show high magnification images of the indicated region and the structure of glomeruli, demonstrating that PARS enables antibody-based labeling throughout the kidney ( $z = 1.2 \text{ mm}$ ). For microscopy see Supplemental Methods. Also see Figure S6, S7, and Supplemental Movie 3 (for 6B).

## Supplementary Figure 1



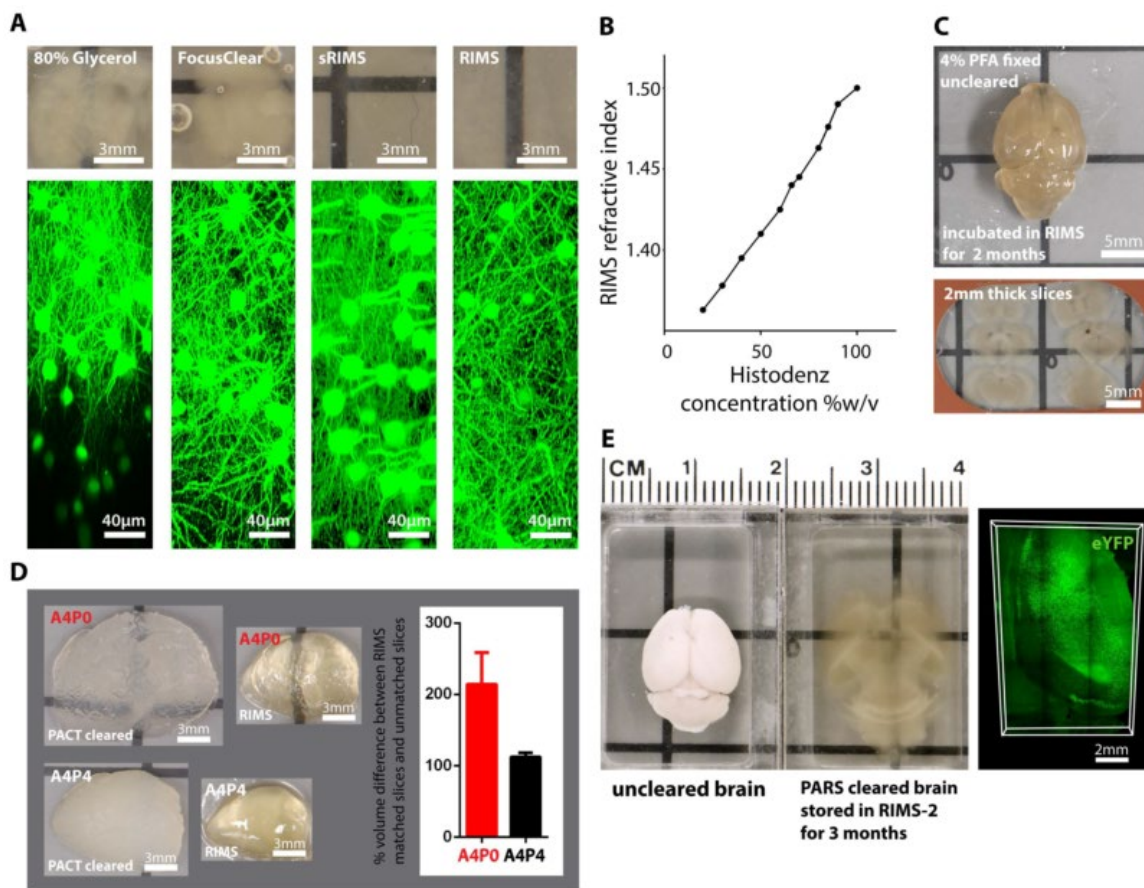
**Supplementary Figure 1, related to Figure 1, 3 and 4; and Table S2: PACT cleared A4P0 tissue-hydrogel hybrid using 8% SDS shows optimal optical transparency.** All samples were PACT cleared for 3 days. (A) Comparison of optical transparency of 3 mm mouse brain coronal blocks PACT cleared using different percentage of SDS and 10% sodium deoxycholate (arrows indicate incomplete clearing). (B) Scanning Electron Microscopy (SEM) images showing the pores of tissue hybridized with different hydrogel percentages; the histograms below indicate the distribution of the pore size for each condition. (C) Compared to A4P4, A4P0 tissue-hydrogel hybrids show greater tissue expansion and optical transparency (1 mm mouse brain slices). Samples for (B) and (C) were PACT cleared in 8% SDS. Images for (A) and (C) were taken using bright field camera.

## Supplementary Figure 2



**Supplementary Figure 2, related to Figures 1 and 2: PACT samples are compatible with gross tissue pathology and fine transcriptional analysis.** (A-C) A 3mm-thick section of a human basal cell carcinoma (BCC) tissue biopsy was cleared with PACT, immunolabeled with anti-pan-cytokeratin (AE1/AE3) antibody, and counter-stained with DAPI. (A) Photographs of uncleared (top) and cleared 3mm-thick section (bottom) of human basal cell carcinoma (BCC) tissue biopsy (scale bars = 5mm). (B) Low magnification (5x) and (C) high magnification (25x) 3D rendering and maximum intensity projections showing tumor tissue (magenta) and keratin filament remnants (green) of apoptotic tissue (scale bars= 500µm and 100µm). (D) (smFISH) For microscopy see Supplemental Methods.

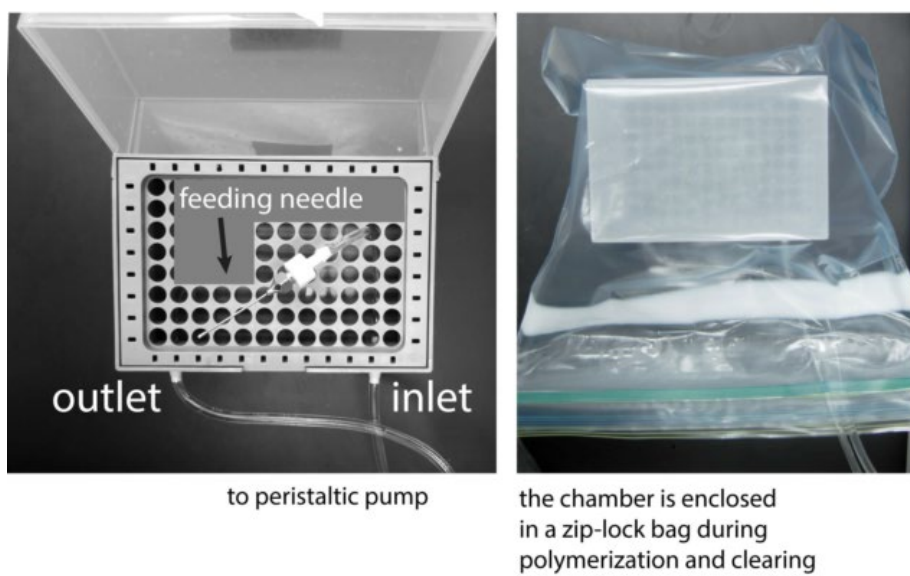
## Supplementary Figure 3



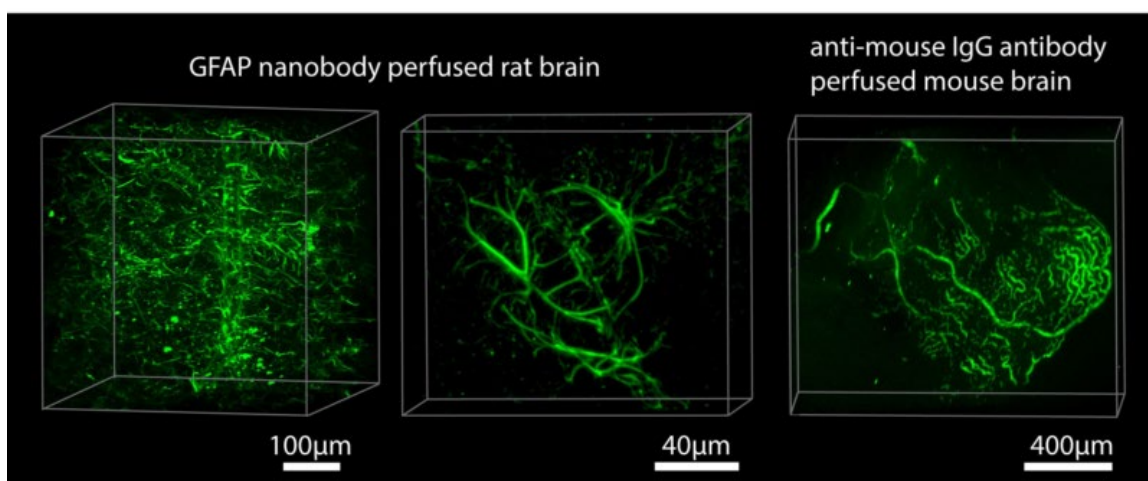
**Supplementary Figure 3, related to Figures 1 and 4; and Table S2: sRIMS and RIMS give better optical transparency by matching the refractive index of cleared tissue-hydrogel hybrid and allow for long-term storage and imaging.** (A) Optical transparency (top, bright field camera) and confocal images (bottom) of PACT cleared 1 mm Thy1-eYFP mouse brain coronal slices mounted and stored for 2 weeks in different media. Whereas the optical transparency of samples mounted in 80% glycerol was very poor, RIMS and sRIMS, a sorbitol solution-based mounting media (see Extended Methods), enhanced the optical transparency and imaging resolution depth of mounted samples. We detected precipitation, perhaps of dissolved salts, in tissue that had been mounted in FocusClear for more than 2 weeks. (B) The refractive index of RIMS prepared with various concentrations of Histodenz (diluted in phosphate buffer). (C) After a 2-month incubation in RIMS, uncleared whole-brain tissues become optically transparent in superficial, poorly myelinated regions. Thus, RIMS immersion offers a milder, albeit slower, alternative to more involved clearing protocols when superior resolution is desired for thick-sectioned (~50-300  $\mu\text{m}$ ) tissue slices. (D) Representative images (bright field camera) and the quantification of the percentage of tissue shrinkage of PACT cleared (3 days) 3 mm Thy1-eYFP mouse brain sagittal blocks after incubated in RIMS for 1 day ( $n = 4$  blocks) for A4P0 and A4P4 hydrogel-tissue hybrids. (E) A size comparison between uncleared Thy1-eYFP whole-brain and a PARS cleared Thy1-eYFP whole-brain mounted in RIMS for 3 months (bright field camera), and the eYFP fluorescence signal ( $z = 1$  mm) after long-term storage in RI 1.43 (60% Histodenz w/v) RIMS-2. For microscopy see Supplemental Methods.

## Supplementary Figure 4

## A PARS perfusion chamber setup



## B

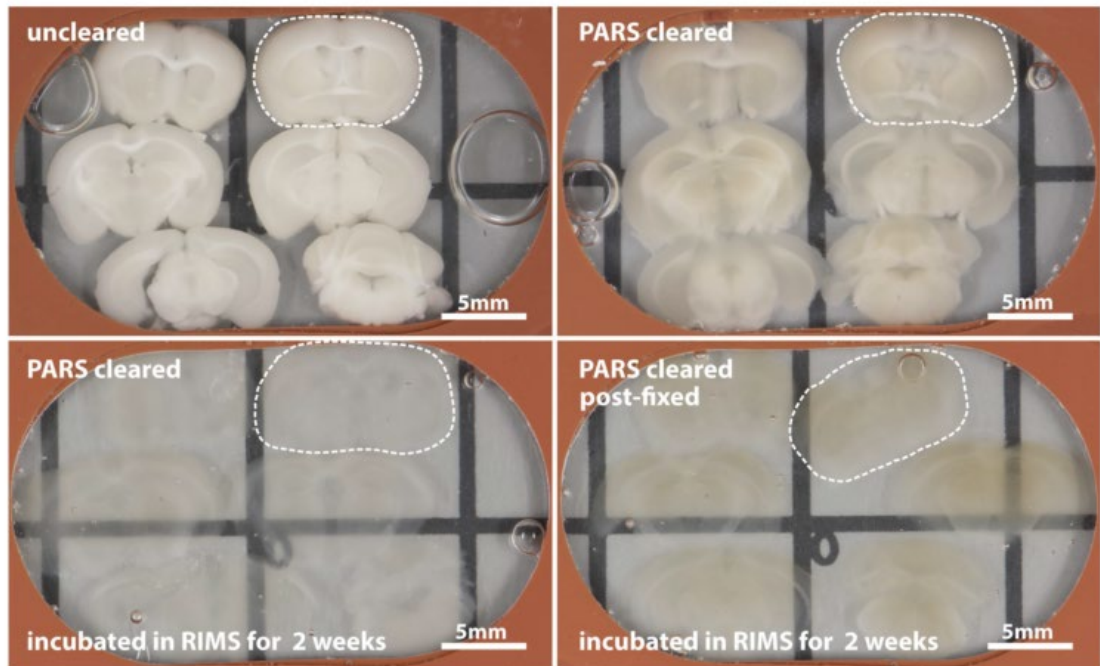


**Supplementary Figure 4, related to Figures 3 and 4: Development of PARS System**

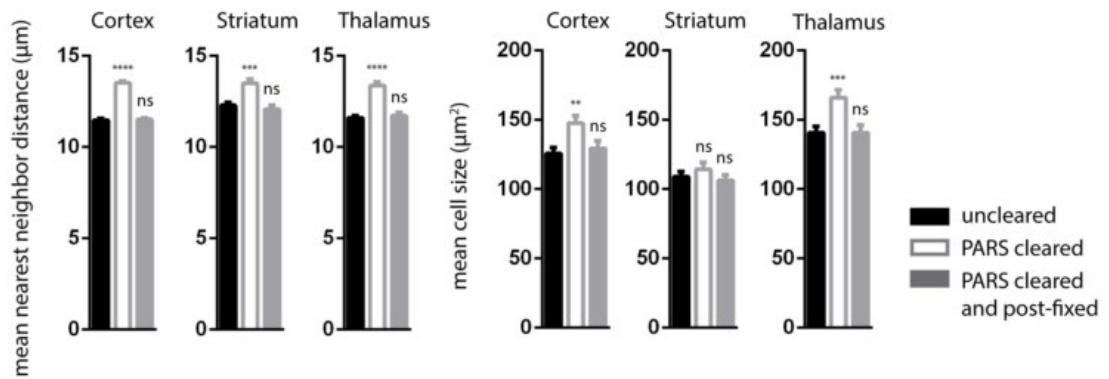
**for whole-body clearing.** (A) Left: PARS was conducted in custom-built perfusion chambers prepared from pipette boxes. Following perfusion-fixation with 4% PFA through a feeding needle that is affixed to the left ventricle or ascending aorta, the rodent is secured atop the pipette tip grating. To drain the pipette box as it fills with perfusate that exits the rodent body through a lesion in the right atrium, one end of a catheter tube is secured to the bottom of the pipette tip box. The tubing is then threaded through a peristaltic pump, and the opposite end is connected to the feeding needle. This allows perfusate to be siphoned out of the pipette box and recirculated back through the cardiac catheter, achieving continuous perfusion of hydrogel monomers, wash buffer, clearing detergents, and histological stains through the rodent vasculature. Of note, this PARS set-up may be applied to PARS-CSF (see **Figure 3A**) by attaching catheter tubing to the intracranial cannula rather than feeding needle. Right: Immediately prior to hydrogel polymerization, the entire perfusion chamber (with catheter-connected subject) is sealed within a ziplock bag for tissue degassing, and the entire set-up is left within this bag throughout the rest of the PARS protocol. The bag allows the perfusion chamber to be placed in a shallow water bath – forming a barrier to prevent water from flooding the perfusion chamber, or from toxic PARS reagents from contaminating the water bath. (B) Rodents were perfused with anti-GFAP (left) and anti-mouse IgG (right) antibodies to investigate whole-body vasculature accessibility via the perfusion of PARS reagents. Specifically, PARS reagents must be able to circulate through both major blood vessels as well as tissue microvasculature in order to achieve uniform, rapid clearing and labeling of both central and peripheral organs, poorly- and well-vascularized tissues alike. Right: Following PARS-based fixation through the cardiac feeding needle, the mouse was perfused with recirculating 100 mL alexa fluor 647 conjugated anti-IgG antibody for 24 hours at room temperature. The brain was then excised, sectioned and PACT-cleared. The images depict the well-preserved vasculature of a 1 mm mouse brain section (cortex) achieved via perfusion-based delivery of whole immunoglobins rather than nanobodies into uncleared tissue. The extensive labeling of mouse vasculature suggests that the PARS pressure gradient can drive antibody solutions through major blood vessels. For microscopy see Supplemental Methods.

## Supplementary Figure 5

A

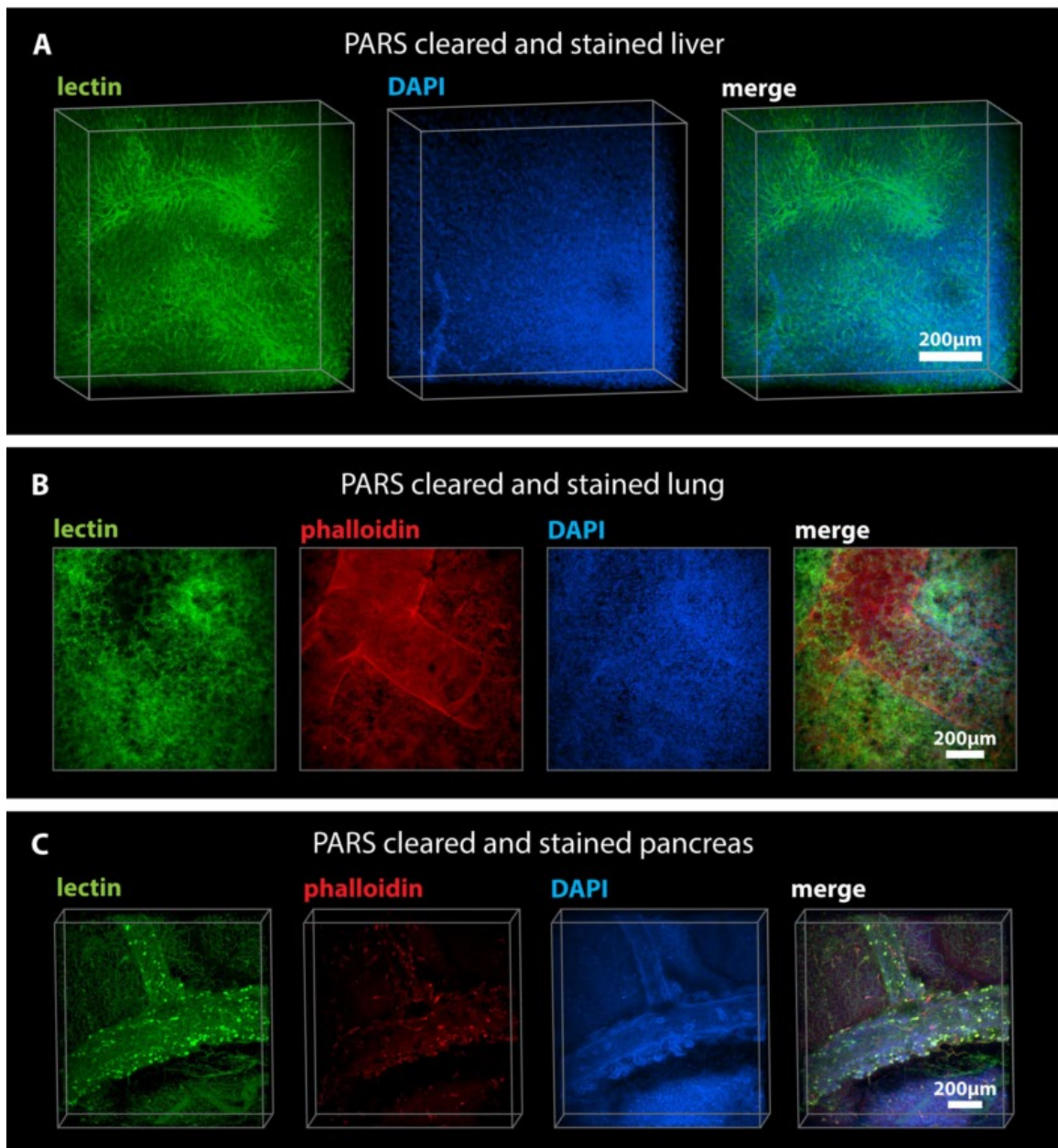


B

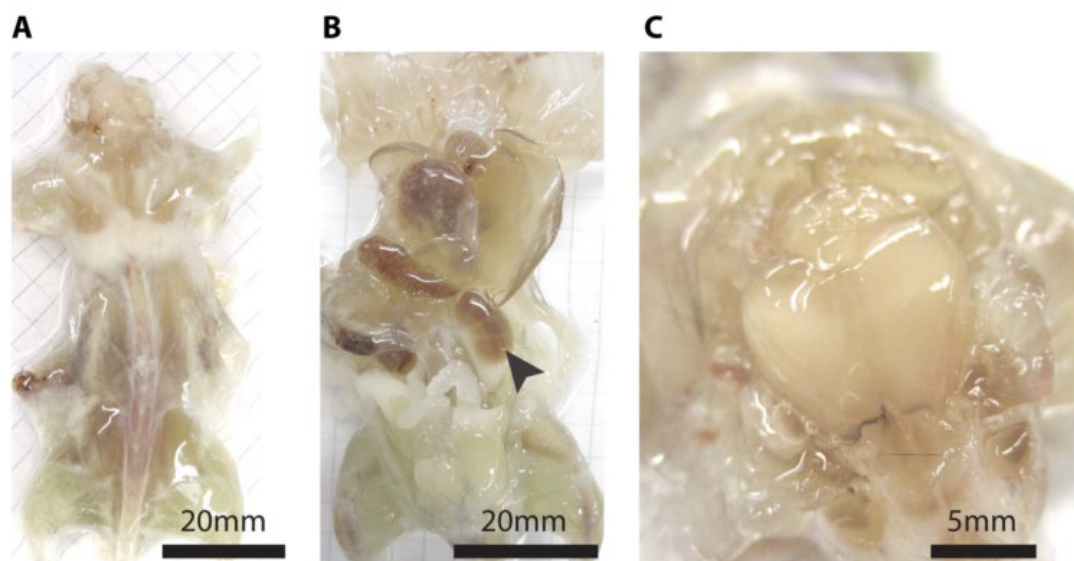


**Supplementary Figure 5, related to Figures 4 and 5: Tissue Preservation and Quantification.** (A) Bright field images of 1mm thick mouse brain slices from uncleared (top left), PARS cleared (top right), PARS cleared and 2-week RIMS immersion (bottom left), and PARS cleared, 4% PFA post-fixed and RIMS mounted mouse brain sections. Note the slices are from the whole brains in Figure 4C. (B) The mean nearest neighbor distance between cells in the cortex, striatum and thalamus were quantified in uncleared, PARS cleared, and PARS cleared then post-fixed brains slices. Compared to the uncleared control, PARS cleared brain slices showed a small but significant increase in cell spacing and cell size in all three regions of the brain while PARS cleared then post-fixed brain slices did not. \*\* indicates  $p < 0.01$ , \*\*\* indicates  $p < 0.005$ , \*\*\*\* indicates  $p < 0.0005$ , and *ns* indicates not significant.

Supplementary Figure 6



**Supplementary Figure 6, related to Figure 6: PARS renders major peripheral organs optically transparent.** Following 1-week of PARS clearing and perfusion-labeling, peripheral organs were excised, cut into 1-2 mm sections, and immersed in RIMS for 24 hours before imaging. **(A)** 500  $\mu\text{m}$  imaging stack of PARS cleared and stained mouse liver sample, with diffuse lectin and DAPI staining suggesting that PARS reagents were able to access the entire organ, despite the density of liver tissue. **(B)** 100  $\mu\text{m}$  imaging stack of PARS cleared and stained mouse lung sample and **(C)** 600  $\mu\text{m}$  thick imaging stack of PARS cleared mouse pancreas sample, both exhibiting high-level lectin, phalloidin and DAPI fluorescent signals throughout. The pancreatic duct is clearly visible in all images of **(C)**. We observed fine resolution of cellular structures in all three tissue samples. Lectin staining, which marks blood vessels, in combination with the fluorescent signals of other small-molecule dyes demonstrate that stained tissue is in the immediate vicinity of tissue vasculature. In peripheral organs, immunolabeling occurs via both vasculature circulation and passive diffusion of perfusate leaks into tissue surrounding vasculature. ( $z = 100 \mu\text{m}$ , scale bars = 100  $\mu\text{m}$ ). For microscopy see Supplemental Methods.

**Supplementary Figure 7**

**Supplementary Figure 7, related to Figure 4, Figures 5 and 6 to a lesser extent: PARS is capable of whole-body clearing.** The (A) dorsal and (B) ventral view of whole Thy1-eYFP mouse after PARS clearing with 8% SDS for 1 week showed good optical transparency of whole body. Arrowhead in (B) points to cleared kidney. (C) The image of the brain for the same mouse. Images were taken using bright field camera.

**Supplementary Table 1, related to Figure 1 (and 4, S1, S5): Methodological Considerations of Major Clearing Protocols of the Last Decade.**

<b>Technique</b>	<b>Clearing time for whole-brain</b>	<b>Complete transparency</b>	<b>Fluorescent quenching</b>	<b>Tissues validated</b>	<b>Significant contribution to field</b>	<b>Drawback</b>
<b><i>BABB</i>, <i>THF</i>, <i>DBE</i>(Becker et al., 2012; Dodt et al., 2007)</b>	hours-days	Yes, but tissue shrinkage	Yes(Ertürk et al., 2012; Ke et al., 2013)	Rodent brain, spinal cord, peripheral tissues	Among first clearing reagents	Harsh reagents(Ke et al., 2013), IHC
<b><i>ClearT2</i>(Kuwajima et al., 2013)</b>	days	No	No-partial(Ke et al., 2013)	Rodent brain and embryo	Less quenching than BABB; novel reagents	IHC: Immunolabeling only through 120 um
<b><i>Scale (A2, U2)</i>(Hama et al., 2011)</b>	weeks - months (slowest)	Yes, but tissue swelling(Chung et al., 2013; Ke et al., 2013; Kuwajima et al., 2013)	No-minimal (Ke et al., 2013; Kuwajima et al., 2013)	Mouse brain, embryo(Hama et al., 2011)	Transparency without quenching; IHC/F	Slow; tissue deformation; potential protein loss with clearing(Ke et al., 2013)

<b>3DISCO</b> ( <b>Ertürk et al., 2012;</b> <b>Ertürk and Bradke, 2013)</b>	< week	Yes	No, but signal decay w/in days(Ertürk et al., 2012; Ertürk and Bradke, 2013)	Peripheral/central organs, embryos, tumors(Ertürk and Bradke, 2013); Central(Ertürk et al., 2012) and peripheral(Jung et al., 2014) nerves	Balance between rapidity and quality of cleared tissue; imaging protocol	Requires immediate sample imaging; IHC-very limited
<b>CLARITY</b> ( <b>Chung and Deisseroth, 2013;</b> <b>Chung et al., 2013;</b> <b>Kim et al., 2013)</b>	10 days	Yes	No	Rodent, human and non-human primate brains, spinal cord, zebrafish(Zhang et al., 2014)	Hydrogel-embedding; best tissue quality when performed correctly; IHC/F	ETC difficult, customized equipment, expensive (Chung et al., 2013)
<b>Advanced CLARITY</b> ( <b>Poguzhelskaya et al., 2014;</b> <b>Tomer et al., 2014;</b>	3 weeks	Yes	No	Whole mouse brain	No ETC – passive thermal CLARITY, COLM, CLARITY objectives,	Requires COLM set-up

<i>Zhang et al., 2014)</i>					rapid imaging protocol	
<i>SeeDB(Kee et al., 2013; Ke and Imai, 2014)</i>	days (fast)	No	No	Young rodent brains(Ke et al., 2013)	No tissue deformation, fast	Tissue browning, incomplete clearing, IHC
<i>CUBIC(Susaki et al., 2014)</i>	2 weeks	Mostly-Yes	No	Rodent and non-human primate brain	CUBIC informatics, optimized Scale(Susaki et al., 2014)	Brain only; potential protein loss during clearing
<i>PACT, PARS</i>	days-weeks	Yes	No	All major rodent organs; whole-body clearing	optimized/simplified CLARITY; permits long-term tissue storage; IHC/F	Slower than 3DISCO

**IHC: Compatible with immunohistochemistry**

**IHC/F: Compatible with immunohistochemistry, immunofluorescent labeling; validated for (> 0.5 mm) depth of antibody penetration**

**IHC: IHC-incompatible, IHC-unverified, or strong restrictions, such as only compatible with lipophilic tissue dyes, or poor antibody penetration (<< 0.5 mm)**

**COLM: CLARITY-optimized light sheet microscopy; CLARITY objectives possess a several-millimeter working distance, which permits whole-brain or thick slice imaging. The COLM set-up grants rapid sample imaging and thus improves the throughput of whole-brain analysis. However, regardless of the imaging**

**methodology followed: e.g. such as those provided in COLM, 3DISCO and CUBIC protocols, whole-brain and large sample imaging requires a specialized, expensive microscopy set-up.**

**Supplementary Table 2, related to Figures 1, S1, and S3: Reagents for PACT, PARS and RIMS.**

<i>Reagent</i>	<i>Formulation or Supplier</i>
0.1 M phosphate-buffered saline (PBS)	For all wash steps and dilutions prepared in PBS, unless noted Combine 8g NaCl, 0.2g KCl, 1.42g Na <sub>2</sub> HPO <sub>4</sub> , 0.245g KH <sub>2</sub> PO <sub>4</sub> in deionized H <sub>2</sub> O to a total volume of 1L; pH to 7.4 and sterile filter.
0.1 M phosphate buffer	(Recipe)
<b>For Cardiac Perfusion-Fixation</b>	
4% Paraformaldehyde (PFA)	Dilute 32% (wt/vol) PFA stock to 4% PFA in final concentration 0.1 M PBS
PBS flush	Prepare 0.1 M PBS with 0.5% sodium nitrate and 10 units/ml heparin
<b>Hydrogel Monomer Solutions</b>	
A2PO	2% Acrylamide, 0% PFA in 0.1 M PBS For 200 ml, add 10 ml of 40% (wt/vol) acrylamide to 100 ml of 0.2 M PBS and 90 ml of distilled water (dH <sub>2</sub> O)
A4PO	4% Acrylamide, 0% PFA in 0.1 M PBS For 200 ml, add 20 ml of 40% (wt/vol) acrylamide to 100 ml of 0.2 M PBS and 80 ml of distilled water (dH <sub>2</sub> O)
A4P4	4% Acrylamide, 4% PFA in 0.1 M PBS For 200 ml, add 20 ml of 40% (wt/vol) acrylamide and 25 ml of 32% (wt/vol) PFA to 100 ml of 0.2 M PBS and 55 ml of distilled water (dH <sub>2</sub> O)
A0P4	4% PFA in 0.1 M PBS For 200 ml, add 25 ml of 32% (wt/vol) PFA to 100 ml of 0.2 M PBS and 75 ml of distilled water (dH <sub>2</sub> O)
0.25% VA-044 Initiator	2,2'-Azobis[2-(2-imidazolin-2-yl)propane]dihydrochloride (VA-044, Wako Chemicals USA, Inc.)

	<ul style="list-style-type: none"> <li>• Add 100 mg to 40 ml hydrogel monomer solution in a 50 ml conical immediately prior to use (PACT)</li> <li>• Add 0.5 g to 200 ml 0.1 M PBS immediately prior to use (PARS)</li> </ul>
N <sub>2</sub>	<ul style="list-style-type: none"> <li>• PACT: attach a long needle to the gas source (N<sub>2</sub> tank with regulator and hose), lower needle to the bottom of the vacutainer or conical containing hydrogel monomer and tissue, and bubble gas through hydrogel solution for 1+ minutes; immediately proceed to hydrogel polymerization step</li> <li>• PARS: attach tubing to the N<sub>2</sub> tank regulator/hose, and insert the opposite end into the ziplock bag; loosely seal ziplock bag around tubing so that excess gas may escape; turn on N<sub>2</sub> gas flow to fill the perfusion chamber and ziplock; allow atmosphere exchange for 2 minutes; immediately proceed to hydrogel polymerization step or bubble N<sub>2</sub> through PBS in perfusion chamber box</li> </ul>
<b>PACT and PARS Detergents</b>	
0.1% tritonX-100 (vol/vol) in PBS	Add 1 ml tritonX-100 to 0.1M PBS for a total volume of 1 L, pH 7.5
4% SDS	Sodium dodecyl sulfate (SDS) Add 40 g SDS to 0.1M PBS for a total volume of 1 L, pH 7.5
8% SDS	Add 80 g SDS to 0.1M PBS for a total volume of 1 L, pH 7.5
20% SDS	Add 200 g SDS to 0.1M PBS for a total volume of 1 L, pH 7.5
10% Deoxycholate	Add 100 g sodium deoxycholate to 0.1M PBS for a total volume of 1 L, pH 7.5
<b>Histology and Imaging</b>	
Antibody incubation buffer	Dilute all antibodies (~1:200-400) and/or staining reagents in 0.1M PBS containing 2% normal donkey serum, 0.1% TritonX-100 and 0.01% (wt/vol) sodium azide; net cost of \$3/ml
RIMS	40 g of Histodenz (Sigma D2158) Histodenz in 30mL of 0.02M phosphate buffer with 0.01% sodium azide, pH to 7.5 with NaOH

sRIMS	70% sorbitol (w/v) (Sigma S1876) in 0.02M phosphate buffer with 0.01% sodium azide, pH to 7.5 with NaOH; net cost of \$0.2/ml
80-90% glycerol	Prepare 80-90% (vol/vol) glycerol in dH <sub>2</sub> O
FocusClear™	(Proprietary, CelExplorer Labs), net cost of \$36/ml
<b>Antibodies and Small-molecule Dyes for Histology</b>	
DAPI	1:200-400 dilution
anti-pan-cytokeratin (AE1/AE3) Alexa Fluor 488 primary antibodies	eBiosciences 1:100 dilution
AlexaFluor 647 conjugated anti-GFAP nanobody	Jackson ImmunoResearch, West Grove, PA 1:100 dilution
chicken anti-tyrosine hydroxylase (TH) IgY	Aves Labs, Tigard, OR 1:200-400 dilution
chicken anti-glial fibrillary acidic protein (GFAP) IgY	Aves Labs, Tigard, OR 1:200-400 dilution
rabbit anti-ionized calcium-binding adapter molecule 1 (Iba1) IgG	Biocare medical, Concord, CA 1:200-400 dilution

rabbit anti-integrin b4, b5 IgG	Santa Cruz Biotechnology, Dallas, Texas 1:200-400 dilution
rabbit anti-beta tubulin IgG	Santa Cruz Biotechnology, Dallas, Texas
AlexaFluor 647 conjugated donkey anti-mouse IgG	Jackson ImmunoResearch, West Grove, PA 1:200-400 dilution
NeuroTrace 530 / 615 Red Fluorescent Nissl Stain	Life Technologies, Grand Island, NY 1:50 dilution
SYSTO 24	1:200-400 dilution
Acridine Orange	
Lectin	1:200-400 dilution
Methylene blue	1:200-400 dilution
Tubulin	1:200-400 dilution
DRAQ5	1:200-400 dilution
Phalloidin	1:200-400 dilution
7.0 mm or 3.0 mm spacers or	iSpacer, SunJin Lab Co.
0.5 mm or 2.5 mm spacers	Silicone Isolator, Electron Microscopy Sciences, PA
<b>smFISH</b>	
Ethanol	Graded dilutions of ethanol: 100%, 95%, 70% ethanol prepared with RNase-free sterile H <sub>2</sub> O

permeabilization buffer	0.5% sodium borohydride (w/v) in 70% ethanol solution
hybridization buffer	10% dextran sulfate (wt/vol, Sigma D8906), 10% formamide (vol/vol), 2X SSC
20mer oligo probes towards B-actin	1nM per each of 24 Alexa 594 labeled 20mer oligo probes towards B-actin prepared in hybridization buffer
2X SSC	Saline sodium citrate buffer
30% Formamide 2X SSC	30% Formamide (w/v) 2X Saline sodium citrate buffer
Slowfade Gold + DAPI	Life S36938
aminosilane-treated coverslips	Thermoscientific

### Table References

- Alexander, A.L., Lee, J.E., Lazar, M., and Field, A.S. (2007). Diffusion tensor imaging of the brain. *Neurotherapeutics : the journal of the American Society for Experimental NeuroTherapeutics* 4, 316-329.
- Bartzokis, G., Lu, P.H., Heydari, P., Couvrette, A., Lee, G.J., Kalashyan, G., Freeman, F., Grinstead, J.W., Villablanca, P., Finn, J.P., *et al.* (2012). Multimodal Magnetic Resonance Imaging Assessment of White Matter Aging Trajectories Over the Lifespan of Healthy Individuals. *Biological psychiatry* 72, 1026-1034.
- Becker, K., Jährling, N., Saghafi, S., Weiler, R., and Dodt, H.-U. (2012). Chemical clearing and dehydration of GFP expressing mouse brains. *PloS one* 7, e33916.
- Berthoud, H.-R., and Neuhuber, W.L. (2000). Functional and chemical anatomy of the afferent vagal system. *Autonomic Neuroscience* 85, 1-17.
- Birmingham, K., Gradinaru, V., Anikeeva, P., Grill, W.M., Pikov, V., McLaughlin, B., Pasricha, P., Weber, D., Ludwig, K., and Famm, K. (2014). Bioelectronic medicines: a research roadmap. *Nat Rev Drug Discov* 13, 399-400.
- Chung, K., and Deisseroth, K. (2013). CLARITY for mapping the nervous system. *Nature methods* 10, 508-513.
- Chung, K., Wallace, J., Kim, S.Y., Kalyanasundaram, S., Andalman, A.S., Davidson, T.J., Mirzabekov, J.J., Zalocusky, K.A., Mattis, J., Denisin, A.K., *et al.* (2013). Structural and molecular interrogation of intact biological systems. *Nature* 497, 332-337.
- Colomba, A., and Ridley, A.J. (2014). Analyzing the roles of Rho GTPases in cancer cell migration with a live cell imaging 3D-morphology-based assay. *Methods in molecular biology* 1120, 327-337.
- Dodt, H.-U., Leischner, U., Schierloh, A., Jährling, N., Mauch, C.P., Deininger, K., Deussing, J.M., Eder, M., Zieglgänsberger, W., and Becker, K. (2007). Ultramicroscopy: three-dimensional visualization of neuronal networks in the whole mouse brain. *Nature methods* 4, 331-336.
- Ernst, R.K., Yi, E.C., Guo, L., Lim, K.B., Burns, J.L., Hackett, M., and Miller, S.I. (1999). Specific Lipopolysaccharide Found in Cystic Fibrosis Airway *Pseudomonas aeruginosa*. *Science* 286, 1561-1565.

Ertürk, A., Becker, K., Jährling, N., Mauch, C.P., Hojer, C.D., Egen, J.G., Hellal, F., Bradke, F., Sheng, M., and Dodt, H.-U. (2012). Three-dimensional imaging of solvent-cleared organs using 3DISCO. *Nature protocols* 7, 1983-1995.

Ertürk, A., and Bradke, F. (2013). High-resolution imaging of entire organs by 3-dimensional imaging of solvent cleared organs (3DISCO). *Experimental neurology* 242, 57-64.

Erturk, A., Mauch, C.P., Hellal, F., Forstner, F., Keck, T., Becker, K., Jahrling, N., Steffens, H., Richter, M., Hubener, M., *et al.* (2012). Three-dimensional imaging of the unsectioned adult spinal cord to assess axon regeneration and glial responses after injury. *Nature medicine* 18, 166-171.

Fukamachi, K., Ishida, T., Usami, S., Takeda, M., Watanabe, M., Sasano, H., and Ohuchi, N. (2010). Total-circumference intraoperative frozen section analysis reduces margin-positive rate in breast-conservation surgery. *Japanese journal of clinical oncology* 40, 513-520.

George, M.S., Sackeim, H.A., Rush, A.J., Marangell, L.B., Nahas, Z., Husain, M.M., Lisanby, S., Burt, T., Goldman, J., and Ballenger, J.C. (2000). Vagus nerve stimulation: a new tool for brain research and therapy. *Biological psychiatry* 47, 287-295.

Gibson, E.M., Purger, D., Mount, C.W., Goldstein, A.K., Lin, G.L., Wood, L.S., Inema, I., Miller, S.E., Bieri, G., Zuchero, J.B., *et al.* (2014). Neuronal Activity Promotes Oligodendrogenesis and Adaptive Myelination in the Mammalian Brain. *Science*.

Hama, H., Kurokawa, H., Kawano, H., Ando, R., Shimogori, T., Noda, H., Fukami, K., Sakaue-Sawano, A., and Miyawaki, A. (2011). Scale: a chemical approach for fluorescence imaging and reconstruction of transparent mouse brain. *Nature neuroscience* 14, 1481-1488.

Hsiao, E.Y., McBride, S.W., Chow, J., Mazmanian, S.K., and Patterson, P.H. (2012). Modeling an autism risk factor in mice leads to permanent immune dysregulation. *Proceedings of the National Academy of Sciences of the United States of America* 109, 12776-12781.

Hsiao, E.Y., McBride, S.W., Hsien, S., Sharon, G., Hyde, E.R., McCue, T., Codelli, J.A., Chow, J., Reisman, S.E., Petrosino, J.F., *et al.* (2013). Microbiota modulate behavioral and

physiological abnormalities associated with neurodevelopmental disorders. *Cell* 155, 1451-1463.

Hsiao, E.Y., and Patterson, P.H. (2011). Activation of the maternal immune system induces endocrine changes in the placenta via IL-6. *Brain, behavior, and immunity* 25, 604-615.

Huppi, P.S., Maier, S.E., Peled, S., Zientara, G.P., Barnes, P.D., Jolesz, F.A., and Volpe, J.J. (1998). Microstructural Development of Human Newborn Cerebral White Matter Assessed in Vivo by Diffusion Tensor Magnetic Resonance Imaging. *Pediatric research* 44, 584-590.

Jung, Y., Ng, J.H., Keating, C.P., Senthil-Kumar, P., Zhao, J., Randolph, M.A., Winograd, J.M., and Evans, C.L. (2014). Comprehensive Evaluation of Peripheral Nerve Regeneration in the Acute Healing Phase Using Tissue Clearing and Optical Microscopy in a Rodent Model. *PLoS ONE* 9, e94054.

Kaya, F., Mannioui, A., Chesneau, A., Sekizar, S., Maillard, E., Ballagny, C., Houel-Renault, L., DuPasquier, D., Bronchain, O., Holtzmann, I., *et al.* (2012). Live Imaging of Targeted Cell Ablation in *Xenopus*: A New Model to Study Demyelination and Repair. *The Journal of Neuroscience* 32, 12885-12895.

Ke, M.-T., Fujimoto, S., and Imai, T. (2013). SeeDB: a simple and morphology-preserving optical clearing agent for neuronal circuit reconstruction. *Nature neuroscience* 16, 1154-1161.

Ke, M.T., and Imai, T. (2014). Optical clearing of fixed brain samples using SeeDB. *Current protocols in neuroscience / editorial board, Jacqueline N Crawley [et al]* 66, Unit 2.22.

Kim, S.Y., Chung, K., and Deisseroth, K. (2013). Light microscopy mapping of connections in the intact brain. *Trends in Cognitive Sciences* 17, 596-599.

Kuwajima, T., Sitko, A.A., Bhansali, P., Jurgens, C., Guido, W., and Mason, C. (2013). ClearT: a detergent-and solvent-free clearing method for neuronal and non-neuronal tissue. *Development* 140, 1364-1368.

Lucas, S.M., Rothwell, N.J., and Gibson, R.M. (2006). The role of inflammation in CNS injury and disease. *British journal of pharmacology* 147 Suppl 1, S232-240.

- Magnon, C., Hall, S.J., Lin, J., Xue, X., Gerber, L., Freedland, S.J., and Frenette, P.S. (2013). Autonomic nerve development contributes to prostate cancer progression. *Science* *341*.
- Poguzhelskaya, E., Artamonov, D., Bolshakova, A., Vlasova, O., and Bezprozvanny, I. (2014). Simplified method to perform CLARITY imaging. *Molecular neurodegeneration* *9*, 19.
- Schain, A.J., Hill, R.A., and Grutzendler, J. (2014). Label-free in vivo imaging of myelinated axons in health and disease with spectral confocal reflectance microscopy. *Nature medicine* *20*, 443-449.
- Singh, P.K., Schaefer, A.L., Parsek, M.R., Moninger, T.O., Welsh, M.J., and Greenberg, E.P. (2000). Quorum-sensing signals indicate that cystic fibrosis lungs are infected with bacterial biofilms. *Nature* *407*, 762-764.
- Susaki, E.A., Tainaka, K., Perrin, D., Kishino, F., Tawara, T., Watanabe, T.M., Yokoyama, C., Onoe, H., Eguchi, M., and Yamaguchi, S. (2014). Whole-Brain Imaging with Single-Cell Resolution Using Chemical Cocktails and Computational Analysis. *Cell*.
- Tomer, R., Ye, L., Hsueh, B., and Deisseroth, K. (2014). Advanced CLARITY for rapid and high-resolution imaging of intact tissues. *Nature protocols* *9*, 1682-1697.
- Vakoc, B.J., Lanning, R.M., Tyrrell, J.A., Padera, T.P., Bartlett, L.A., Stylianopoulos, T., Munn, L.L., Tearney, G.J., Fukumura, D., Jain, R.K., *et al.* (2009). Three-dimensional microscopy of the tumor microenvironment in vivo using optical frequency domain imaging. *Nature medicine* *15*, 1219-1223.
- Zhang, M.D., Tortoriello, G., Hsueh, B., Tomer, R., Ye, L., Mitsios, N., Borgius, L., Grant, G., Kiehn, O., Watanabe, M., *et al.* (2014). Neuronal calcium-binding proteins 1/2 localize to dorsal root ganglia and excitatory spinal neurons and are regulated by nerve injury. *Proceedings of the National Academy of Sciences of the United States of America* *111*, E1149-1158.
- Zoukos, Y., Leonard, J.P., Thomaidis, T., Thompson, A.J., and Cuzner, M.L. (1992). beta-Adrenergic receptor density and function of peripheral blood mononuclear cells are increased in multiple sclerosis: a regulatory role for cortisol and interleukin-1. *Annals of neurology* *31*, 657-662.

## Extended Methods

### Animals

Wild-type mice (C57BL/6N and FVB/N, both males and females), *Thy1-YFP* mice (line H), and *Th-cre* (1Tmd/J) mice were used in the development and testing of novel clearing protocols and clearing reagents. *Thy1-YFP* mice were used to evaluate the maintenance of endogenous fluorescent signals throughout multi-week clearing steps and under long-term sample storage in RIMS. Periadolescent through adult wild-type rats (Long-Evans and Wistar, males and females) were used to optimize clearing protocols for larger tissue samples, and to depict the preservation of vasculature during lengthy perfusion-based clearing and antibody staining steps. For transcardial perfusion, subjects were deeply anesthetized with an overdose of Euthasol (100 mg/kg IP injection) prior to intracardiac perfusion first with heparinized PBS (10U/mL heparin in 0.1 M PBS) containing 0.5% NaNO<sub>2</sub> and then with 4% PFA. For PACT, the brain and/or desired organs were excised and post-fixed in 4% PFA for several hours prior to hydrogel monomer infusion and clearing steps. For PARS-based whole-body clearing, the intracardiac catheter was inserted to the level of the aortic arch, stabilized inside the aorta with a loop of suture thread and a microclamp. For PARS-based whole-brain clearing, the descending aorta was ligated with a microclamp.

For experiments involving the visualization of AAV9-CAG-eGFP transduced cells, young adult female C57Bl/6 mice were injected with virus via the retro-orbital sinus, and following a 6-month delay for viral transduction and eGFP expression, mice were euthanized for PACT and PARS studies.

**Ethics statement:** Animal husbandry and all experimental procedures involving mice and rats were approved by the Institutional Animal Care and Use Committee (IACUC) and by the Office of Laboratory Animal Resources at the California Institute of Technology.

### AAV production and systemic delivery

By injecting mice with adeno-associated viral vectors carrying fluorescently-labeled transgenes, we were able to observe the compatibility of PARS processing and RIMS

mounting with more sparse, localized fluorescent labeling than that which is driven by the Thy1 promoter (**Figure 5A-C** versus **Figure 5D-E**). Sparse labeling of specific neuron types and glia as well as localized eGFP expression in distinct organs (e.g. liver and hippocampus **Figure 5D-E**) was clearly visible. Single stranded ssAAV-CAG-eGFP vectors packaged into AAV9 or the AAV9 variant capsid, AAV9BD1, was generated and purified as described (Lock et al., 2010). The AAV2/9BD1 capsid was modified from AAV2/9 (U. Penn) with the following mutations (VP1 numbering): An N498Y mutation was made to reduce liver transduction (Pulicherla, 2011) and the amino acid sequence AAADSPAHP (Chen et al., 2009) between AA588-589 and a Y731F mutation (Pulicherla et al., 2011) were made in an unsuccessful attempt to increase CNS transduction.  $1 \times 10^{12}$  vector genomes (vg) of either virus was delivered intravenously into young adult female C57Bl/6 mice via the retro-orbital sinus and the mice were euthanized 6 months later for assessment of native eGFP fluorescence by PARS. All imaging of PARS brain and liver tissue from AAV9-injected mice was performed after 2 weeks tissue storage in RIMS.

## **PACT and PARS clearing reagents**

### *Selection of PACT and PARS reagents*

To screen different hydrogel monomer formulations and clearing conditions, several adult C57 and Thy-1 eYFP mice (Jackson) were anesthetized with an overdose of Euthazol (100 mg/kg, IP injection) and transcardially perfused first with PBS containing 0.5% NaNO<sub>2</sub> and 10U/mL heparin, and then 4% paraformaldehyde (PFA) in PBS. The excised whole brains were post-fixed in 4% PFA for 6 hours, sliced into 1 mm and 3 mm sagittal sections and coronal sections, and then sections were incubated at 4°C overnight in A2P0 (2% acrylamide and 0% paraformaldehyde in PBS), A4P0 (4% acrylamide and 0% paraformaldehyde in PBS), or, A4P4 (4% acrylamide and 4% paraformaldehyde in PBS) hydrogel monomer solution, each containing 0.25% photoinitiator 2,2'-Azobis[2-(2-imidazolin-2-yl)propane]dihydrochloride (VA-044, Wako Chemicals USA, Inc.). While still submerged in hydrogel monomer, the hydrogel-infused samples were degassed by bubbling nitrogen through the sample-hydrogel solution in the vacutainer or 5 mL

Eppendorf tubes for 1 minute. It should be noted that we experimented with several, more rigorous methods of replacing oxygen atmosphere with an inert gas, as was deemed necessary in the original and advanced CLARITY protocols (Chung et al., 2013; Tomer et al., 2014) (e.g., 1. Placing the vacutainer containing the sample on ice, 2. Degassing the vacutainer with the house vacuum line while gently vortexing for several minutes, 3. Removing the sample from ice and bubbling nitrogen through the hydrogel monomer solution for several minutes, 4. Repeating steps 1-3 several times). However, we found that the brief 1-minute exchange of oxygen for nitrogen supported adequate polymerization: residual oxygen may have hampered the complete hybridization between tissue and acrylamide monomers, however our tissue-hydrogel matrix was sufficient for preserving tissue architecture and protein content. To polymerize the hydrogel-tissue matrix, the samples were transferred to a 37 °C waterbath or heating block and incubated for 2-3 hours at this elevated temperature. The polymerized samples were washed briefly with PBS to remove excess hydrogel, transferred to 50 mL conical tubes, and incubated for 2-5 days at 37 °C with shaking in either PBS, 0.1% tritonX-100 in PBS, or a clearing solution: 4% SDS, 8% SDS, 20% SDS, or 10% Deoxycholate, all prepared in 0.1M PBS, pH 7.5. Images of 3 mm brain sections were taken at 24 hours and 48 hours (**Figure 1A**) to show the trade-off between greater tissue swelling for tissue-hydrogel matrixes prepared with low PFA concentrations, and slower tissue clearing for tissue-hydrogel matrixes prepared with high PFA (and acrylamide) concentrations; the A4P0 hydrogel formulation was selected for general use in subsequent PACT and PARS experiments. 72-hr incubation of brain sections in the 8% SDS clearing solution resulted in superior tissue clearing (**Figure S1A**), and so the 8% clearing solution was selected for subsequent PACT and PARS experiments. Regarding clearing time, this parameter must be optimized in a case-specific manner. 24-hour clearing may be sufficient for small tissue samples or highly porous tissue, while larger, highly myelinated, or dense tissue sections and whole organs may require >96 hours. Care must be taken to not overclear the samples and also to check periodically for excessive swelling if samples are to be stored long term since swelling does contribute to hydrogel softening and disintegration in the long run, risking sample loss. This is accelerated by elevated temperature and mechanical stress during sample preparation and handling. Gentle treatment of the tissue-hydrogel samples and the addition of anti-

microbial agents to incubation solutions allows the hydrogel to remain stable for up to two weeks. Also, we found that an additional round of tissue crosslinking with 1-2% PFA or of tissue-hydrogel re-polymerization after clearing was beneficial to counteracting both tissue expansion in mounting media and tissue disintegration.

### **PACT Immunohistochemistry**

To immunostain PACT-processed tissue, cleared samples were washed with 4-5 changes of PBS over 1 day to remove residual SDS. Then, the samples were incubated with primary antibodies (1:200-400) in PBS containing 2% normal donkey serum, 0.1% TritonX-100 and 0.01% sodium azide at room temperature with shaking for 3-7 days. Six A4P0-polymerized and six A4P4-polymerized 3-mm sagittal sections were removed from these antibody incubations at 24hrs, 48 hrs and 72 hrs in order to measure IgG penetration depth in cleared tissue (see **Figure 1B**). For remaining sections, unbound primary antibody was removed via washing sections in 4-5 PBS buffer exchanges over the course of one day. Then, samples were incubated with secondary antibodies (Fab fragment secondary antibodies are preferred, 1:200-400) in PBS containing 2% normal donkey serum, 0.1% TritonX-100 and 0.01% sodium azide at room temperature with shaking for 2-5 days.

After washing with 4-5 changes of PBS over 1 day, the samples were incubated in RIMS solution (40 g of Sigma D2158 (Histodenz) in 30mL of 0.02M phosphate buffer with 0.01% sodium azide, pH to 7.5 with NaOH – which results in a final concentration of 88% Histodenz w/v) at room temperature until they become transparent. During long incubations (> 4 days) of tissue in antibody, small-molecule stains, or RIMS, the solution was exchanged for fresh halfway through the incubation. As an extra precaution and to prevent bacterial growth, tissues may be transferred to fresh 50 ml conical tubes or staining jars with every buffer exchange. It is suggested that RIMS incubations and mounting be performed in a clean environment – either in a hood, or by decanting RIMS into a fresh conical over flame to minimize bacterial contamination.

The primary antibodies used for passive staining were chicken anti-tyrosine hydroxylase (TH) IgY, chicken anti-glial fibrillary acidic protein (GFAP) IgY (Aves Labs, Tigard, OR), rabbit anti-ionized calcium-binding adapter molecule 1 (Iba1) IgG (Biocare medical, Concord, CA), rabbit anti-integrin b4, b5 IgG, and rabbit anti-beta tubulin IgG (Santa Cruz Biotechnology, Dallas, Texas). An AlexaFluor 647 conjugated donkey anti-mouse IgG (Jackson ImmunoResearch, West Grove, PA) was used for the antibody penetration experiment (Figure 1B). Nissl staining was performed with NeuroTrace 530 / 615 Red Fluorescent Nissl Stain (1:50 in PBS, Life Technologies, Grand Island, NY; samples were incubated at RT overnight and then washed in PBS prior to mounting. For small molecule staining with acridine orange, samples were placed in a 100 $\mu$ g/mL solution of acridine orange for 10 minutes, followed by washout in PBS for one hour. The tissues were then placed in RIMS solution for 4 hours prior to imaging. All steps were performed at room temperature.

### **PARS chamber design**

To perfuse PARS reagents through vasculature for clearing and immunolabeling steps necessitated the fabrication of a simple apparatus to recirculate reagents with a continuous pressure gradient on tissue for several days-to-weeks during the lipid extraction and antibody diffusion. So, using the traditional cardiac perfusion fixation technique (Gage et al., 2012; Jonkers et al., 1984) as a delivery method, we devised a PARS chamber that consisted of the following components: 1) a feeding needle catheter clamped in-place within the left ventricle of the subject, 2) a perfusate collection well (pipette box) to catch recirculating reagents that exit the vasculature through a lesioned right atrium, and 3) catheter tube (PTFE tubing) that transfers recirculating reagents from the collection well back into subject vasculature via its passage through a peristaltic pump (**Figure S4A**). To confirm that this set-up was functional for whole-organism clearing, several different detergents including SDS at several different percentages, sodium lauryl sarcosine, and sodium deoxycholate, at various concentrations, were continuously perfused through whole mice and rats via the carotid artery for up to 2 weeks. As in PACT (**Figure S1A**), only SDS could effectively render tissue transparent for optical imaging. Likewise, when

delivered using the PARS chamber set-up, 8% SDS could efficiently solvate lipids deep in tissue and accomplish uniform clearing of large tissue samples. Thus, the PARS chamber set-up was adopted for subsequent PARS experiments.

### **PARS clearing and staining**

For transcardial perfusion fixation of adult mice or rats, a feeding needle was inserted through the left ventricle and into the aorta, and loosely sutured in place to the vessel at the level of the aortic arch. Following perfusion with PBS and 4% PFA, as summarized for PACT, the fixed whole rodents were transferred into a custom-built perfusion chamber where the solutions inside the chamber is perfused into the rodent and recirculated via a peristaltic pump. The rodent is were post-fixed with 4% PFA through the same feeding needle into the aorta at a flow rate of 1mL/min for 1-2 h at room temperature. For clearing of rat brain and spinal cord, we systematically ligated the arterial circulation leaving the carotid arteries intact and removed tissue not directly perfused by these vessels. To prevent PFA from cross linking the acrylamide monomers, we first perfused PBS for 2 hours at RT to wash out the residual PFA and we infused 4% acrylamide (A4P0) in PBS at RT overnight. The next day, we again perfused PBS to remove any remaining PFA/acrylamide polymers/monomers in the vasculature. Before polymerization and without disconnecting perfusion lines, we placed the perfusion chamber into a ziplock bag and infused nitrogen gas into the perfusion chamber through a separate connection to degas the sample. The polymerization process was initiated by adding 200mL of 0.25% VA-044 initiator with PBS and submerging the degassed perfusion chamber in a 37-42 degree water bath for 2-3 hours. A lead weight was placed on top of the perfusion chamber to prevent it from tipping over. After polymerization, the solution was replaced with 8% SDS in 0.1M PBS, pH 7.5 clearing buffer, and the mouse/rat was perfused for up to 2 weeks. For PARS IHC, the cleared mouse/rat was first perfused with 8 buffer changes of 200mL PBS over a two day period to remove the residual SDS. Then, using the same antibody formulations described in the PACT protocol, a 3-day perfusion with a primary antibody cocktail, 1-day perfusion with PBS wash, a 3-day perfusion with the secondary antibody cocktail, and a 1-day PBS wash was conducted in order to stain the peripheral organs of the cleared mouse/rat.

### **PARS-CSF methodology for brain and spinal cord clearing**

For applications restricted to brain and spinal cord mapping, we developed a within-skull PARS strategy that grants thorough clearing of the whole-brain and whole-spinal cord by direct infusion of hydrogel monomers and clearing reagents into the CSF via an intracranial brain shunt. Under specific circumstances (e.g., the pre-existing availability of a guide cannula in the subject from an *in vivo* pharmacological, neurobiological, or optogenetic study), PARS-CSF would permit whole-brain clearing and histology that is automatically optimized for the region near the existing cannula, and that requires less time and reagents as the equivalent whole-organ PACT procedure.

Herein, we validated two routes for intracranial delivery of PARS reagents. To clear the spinal cord, a cannula may be inserted either into the cisterna magna or lowered through the skull (by drilling a hole in the region of interest and using tweezers to create an opening in the dura), to the level of the subarachnoid space, directly above the dorsal inferior colliculus, (see **Figure 3A**). The rat spinal cord sample (right) could be cleared when PARS-CSF was conducted at elevated temperatures and for a longer period of clearing. To clear the whole-brain, the cannula may be lowered through the skull, penetrating the dura, and placed in the region directly above the olfactory bulb (see **Figure 3B**). The cannula (21G PlasticsOne) is cemented in-place on the skull surface using dental acrylic (Metabond). The PARS procedure was then applied to this intracranial preparation: the catheter tubing was connected to the subdural cannula as opposed to the cardiac feeding tube, and all PARS reagents were infused at 1 ml/min using the same order and timeframe as in PARS. For whole-brain clearing, the subject may be decapitated, with only the head transferred to the PARS chamber and connected to the infusion lines. The subject was then transcardially perfused with 4% PFA followed by PBS wash, and the head placed atop the pipette tip rack of the PARS chamber (**Figure S4A**). The pipette box and catheter lines were prefilled with 4% acrylamide monomer solution (A4P0), the tubing was connected to the cannula, and A4P0 was intracranially infused at a 1 ml/min flow rate overnight at room temperature (**Figure S4A**, left). After flushing the brain of unbound PFA and acrylamide

monomers (2-hour infusion of PBS), which was critical to ensure that the vasculature remained unpolymerized, the whole-brain was degassed via transferring the PARS chamber into a ziplock bag and placing the chamber under an inert atmosphere ( $N_2$ ) for two minutes (**Figure S4A**, right). The bagged-PARS chamber was then transferred to a 37-42 °C water bath, and degassed PBS supplemented with the thermal initiator was infused through the brain for the entire 2-3 h incubation. After formation of this whole brain-hydrogel matrix, in-skull tissue clearing was accomplished via constant perfusion-recirculation of 8% SDS through the cannula for 4 days, with the PARS chamber remaining in the 37-42 °C water bath for the entire process. Finally, after extensive PBS washing (2-3 days), the catheter lines were disconnected, and the brain was removed, sectioned, and mounted in RIMS for imaging (**Figure 3B**).

Using mice that were IV-injected with AAV9-eGFP, the PARS-CSF procedure for whole-organ clearing was validated with respect to the following conditions: 1) only limited bias in how well regions clear relative to the cannula placement, 2) no structural damage in regions near the cannula due excessive fluid pressure, either from too high flow rate or inadequate drainage of perfused liquids, causing high intracranial pressure, 3) preservation of subcellular structural morphology, and 4) good visualization of sparsely labeled cell populations and fluorescence, especially in comparison of bright, widespread eYFP labeling of Thy1-eYFP mice versus virus-mediated eGFP in wild-type mice. It may have particular relevance to scientists performing research that already involves the use of intracerebral (IC) or intracerebroventricular (ICV) cannulated mouse or rat subjects and that requires post-mortem brain histology for each subject.

### **Antibody penetration**

Four transcardially perfused and 4% PFA post-fixed adult mouse (4-12 weeks old) brains were cut into 2 mm sagittal slices, and these slices were PACT processed. Specifically, one half of each PFA-fixed brain was hybridized with A4P4 hydrogel, while the other half was hybridized in 4A0P hydrogel. All the samples were passively cleared with 8% SDS in PBS, as described in the PACT protocol, and the residual SDS was removed by PBS washing for 1 day. The samples were then incubated in primary antibody cocktails (donkey anti-

mouse-IgG antibody, 1:200, in PBS containing 2% normal donkey serum, 0.1% Triton-X100 and 0.01% sodium azide) for a range of time-periods, spanning 24-72 hours. Samples were then washed with 4-5 buffer exchanges of 0.1 M PBS over 1 day and mounted in RIMS solution. Images were taken with a Zeiss LSM 780 confocal microscope using the W Plan-Apochromat 20x/1.0 DIC M27 (working distance 1.8mm). The depth of antibody penetration (**Figure 1B**) was outlined on y-z projected images using Fiji with Reslice and Z project plugins.

### **RIMS (Refractive Index Matching Solutions) for PACT and PARS samples**

We experimented with several different mounting medias, including: 80-90% glycerol, FocusClear™, RIMS, a mounting media optimized for our imaging set-up with standard confocal microscopy. RIMS solution was prepared via dissolving 40 g of Histodenz™ (Sigma D2158) in 0.02M phosphate buffer with 0.01% sodium azide for a total volume of 30 mL, pH to 7.5 with NaOH, which results in a final concentration of 88% Histodenz (w/v) with RI = 1.46 (used throughout this work unless otherwise noted). Estimated cost to produce is \$3/mL while FocusClear is \$36/mL. We note that the refractive index (RI) of RIMS may be adjusted to match the specific tissue/imaging system: it is expected that the RIMS RI may range from 1.42 (60% Histodenz w/v) to 1.48 (95% Histodenz w/v) in order to obtain optimal sample resolution. Light transmittance in RIMS (**Figure S3B**) was measured.

For RIMS mounting, samples were first submerged in RIMS at room temperature until they become transparent. During this period, the cleared tissue initially shrinks for the first few hours (see **Figures 3B, S3D**). Continued incubation in RIMS will lead to gradual tissue expansion over time until RIMS has fully penetrated the tissue (see **Figures 4C, S5A**); we observed that our largest samples (e.g. rat whole-brain) became transparent within one week of RIMS-immersion, after which their expansion ceased. We were able to limit tissue expansion, however, by post-fixing the cleared and stained samples in 4% PFA for 1-2 hours at room temperature (small samples) or up to overnight (large samples) before proceeding to RIMS incubation (see **Figure 4C**, right box; **Figure S5A**, lower right box).

Although post-fixing PARS tissue curtailed gradual tissue volume expansion (**Figure S3**), the additional crosslinking also precipitated a slight decrease in tissue transparency (**Figure S5A**). Fluorescence intensity, cell phenotyping, or resolvable depth of imaging were not adversely affected, however.

sRIMS: a cost-effective sorbitol-based alternative to RIMS: 70% sorbitol (w/v) (Sigma S1876) in 0.02M phosphate buffer with 0.01% sodium azide, pH to 7.5 with NaOH; net cost of \$0.2/ml.

While RIMS outperformed sRIMS in our hands in terms of resolvable imaging depth, sorbitol is a commonly available chemical across scientific laboratories, and thus offers a convenient, cost-effective and superior alternative to glycerol-based mounting solutions.

### **Vasculature preservation**

Rats were transcardially perfused with heparinized PBS, 4% PFA, and lastly hydrogel monomer solution according to the PARS protocol. Then, following hydrogel infusion but before clearing, the rat was perfused via its intra-aortic catheter with 100 mL AlexaFluor 647 conjugated anti-GFAP nanobody (1:100 in PBS) at room temperature overnight. The brain was removed from the skull and incubated in 4% PFA at 4°C overnight to crosslink the nanobody. The brain was then cut into 1 mm coronal slices and PACT cleared in 8% SDS in 0.1M PBS, pH7.5 at 37°C for 3 days. Cleared samples were incubated in RIMS solution for one day and mounted in RIMS solution for imaging. Images were taken using Zeiss LSM 780 confocal microscope with LD LCI Plan-Apochromat 25x/0.8 Imm Corr DIC M27 multi-immersion objective.

### **Sliced tissue expansion and weight gain measurement**

PFA-fixed adult mouse (4-12 weeks old) brain was cut into six 1 mm thick coronal slices. Slices from one half of the brain were stored in PBS, while slices from the other half of the brain were PACT-cleared for 4 days. Slices were weighed and imaged with a conventional camera before and after clearing. The size of the slices was outlined and calculated using Image J. The tissue expansion and weight gain were determined by calculating the change

in size and weight of slices before and after clearing (**Figure 1E**), and normalizing them to the pre-PACT measurements.

### **Protein loss measurement**

The percentage of protein loss for each sample (**Figure 1C, 2E**) was obtained by measuring the amount of total protein in the clearing solutions collected from PACT or PARS clearing with NanoDrop blanked with respective solutions, and normalized to the weight of the mouse (for PARS) or the slices (for PACT) before clearing.

### **Whole-Brain Tissue Morphology Preservation and Quantification**

To observe the effect of PARS processing and RIMS mounting on brain volume, PFA-fixed adult mouse brains were either immediately extracted (uncleared control) or PARS-processed; and then brains from these two groups were treated according to one of the following conditions: incubated in PBS for 1 day, incubated in PBS for 1 week, mounted in RIMS for 1 day, mounted in RIMS for 2 weeks, or post-fixed and mounted in RIMS for 2 weeks. Cleared and uncleared brains from all conditions were then photographed to estimate their relative size change (**Figure 4C**), cut into sections to visualize clearing depth (**Figure S5A**), slide-mounted, and imaged via confocal microscopy in order to evaluate gross changes in tissue architecture (e.g. morphological deformations of major brain regions, structure integrity of ventricles and vasculature) (**Figure S5B**). The percentage of protein loss for each sample (**Figure 1C, 2E**) was obtained by measuring via NanoDrop the protein concentration of clearing solution aliquots that were collected after PACT or PARS-processing of tissue. The net protein loss could then be estimated based on this concentration and the known total volume of clearing solution used during processing. The amount of protein lost by each sample was normalized to the weight of the mouse (for PARS) or the tissue slice (for PACT) before clearing so that protein losses across samples and across tissue processing conditions could be compared.

## Single-molecule RNA FISH

Tissue samples were adhered to aminosilane-treated coverslips by dehydrating for 1 hour under light vacuum. Samples were permeabilized prior to hybridization according to the following protocol: First, samples were washed twice in 100% ethanol for 10 minutes at room temperature. Next samples were washed in 95% ethanol for 10 minutes at room temperature. Samples were then incubated in 70% ethanol for 2 hours at 4°C. After incubation, tissue was placed in a 0.5% sodium borohydride (w/v) 70% ethanol solution for 10 minutes at room temperature. Finally, the tissue was rehydrated with 3 washes of PBS.

Hybridizations were performed overnight at 37°C in a hybridization buffer composed of 10% dextran sulfate (w/v, Sigma D8906), 10% formamide (v/v), 2X SSC containing 1nM per each of 24 Alexa 594 labeled 20mer oligo probes towards B-actin. The next day samples were washed in 30% Formamide 2X SSC at room temperature for 30 minutes followed by 4 washes with 2X SSC. After washing sample was mounted between two coverslips with Slowfade Gold + DAPI (Life S36938). Samples were imaged on a Nikon Ti Eclipse microscope with an Andor Ikon-M camera and a 60X/1.4NA Plan Apo  $\lambda$  objective with an additional 1.5x magnification. Images were acquired as Z-stacks with a 0.5 $\mu$ m step size over 30 $\mu$ m. Samples were excited by a 589nm (SDL-589-XXXT), 532nm (SDL-532-200TG) and 405nm(SDL-405-LM-030) lasers manufactured by Shanghai Dream Laser.

The smFISH images (**Figure 2**) were analyzed using image analysis scripts written in MATLAB. To determine the average background of the sample, the images were median filtered using a 50x50 pixel kernel and the average pixel intensity of the center 200x200 pixel sub-image was used as the average background value of the image. The smFISH dots were found by applying a Lapacian of Gaussian filter, thresholding the image based on the average background value and comparing the resulting image with a dilated image to find local maxima. The error bars were calculated using the standard deviation of the resulting measurements.

## Human tissue biopsy preparation

Human basal cell carcinoma skin tissue samples were obtained from patients undergoing excision of their cancers after appropriate informed consent and under approval of UCLA IRB #12-01195. Tissue samples were obtained from sections of tumors not necessary for diagnostic or margin control purposes and varied in size depending on the size of the original skin cancer.

Biopsied tumor samples were processed utilizing the PACT methodology as described for rodent tissue, using 4% acrylamide solution (A4P0) to generate hydrogel support matrix for fixed tissue. Polymerized tissue-hydrogel matrices were then passively cleared for 2-7 days (i.e., depending on tissue thickness) in 8% SDS at 37 °C. In general, a 3 mm thick human skin section could be rendered transparent within 3-4 days.

PACT-processed samples were immunolabeled with anti-pan-cytokeratin (AE1/AE3) Alexa Fluor 488 primary antibodies (eBiosciences) at 1:100 dilution for two days followed by a 1-day wash in PBS. All labeling and wash steps were performed at room temperature, and final PACT-processed biopsy samples were mounted in RIMS. Imaging was performed on a Zeiss 780 confocal microscope with a 20x long working distance objective as described above.

Despite testing a range of clearing times (2-7 days in 8% SDS) for tissue-hydrogel samples, the subcutaneous layer (consisting primarily of adipocytes) resisted consistent clearing (yellow tissue, **Figure S2A**) due to incomplete micelle solvation of all the packed lipids in adipocytes.

### **Scanning Electron Microscopy**

Samples were imaged on an FEI Quanta 200F environmental scanning electron microscope (ESEM) in ESEM mode. Thin slices of PACT-processed brain tissues were placed on the sample holder in the chamber and imaged at a voltage of 5 kV and working distance between 7.7-8.3 mm with a spot size of 3 or 4 using the gaseous secondary electron detector (GSED). Please note that stretching during cutting/SEM process will make the pores of tissue-hydrogel hybrid larger. The actual effective pore size of the SEM images should be smaller than we present here.

## Quantification methods

Mean Nearest neighbor distance: 1mm thick coronal slices were stained with DAPI and imaged w/ the 10x 0.45N.A. plan-apo objective. 24 3 $\mu$ m-thick images were taken from different regions of the cortex thalamus and striatum. A 30 pixel rolling ball radius subtraction filter was used to remove the background. All images are individually thresholded and converted into a binary image. A binary watershed segmentation was applied to divide cells that are clustered together. The resulting images were quantified with the analyzing particles option on Image J. The centroid of each cell was identified in the measurement the nearest neighbor distances were calculated by applying the “nnd” plugin on imageJ.

GFP size quantification: 1mm thick coronal slices of AAV9-eGFP IV injected mouse brain were imaged with the 5x 0.25N.A. Fluar objective. A maximum projection of the Z-stack was used for quantification. The area of each GFP positive neuron was isolated and quantified with the analyzing particles option on ImageJ.